The Transient Motion of a Solid Sphere Between Parallel Walls

A Thesis

Submitted to the College of Graduate Studies and Research
In Partial Fulfillment of the Requirements for
the degree of
Master of Science
in the
Department of Mechanical Engineering
University of Saskatchewan
Saskatoon

By

Warren T. Brooke

Permission to Use

In presenting this thesis in partial fulfillment of the requirements for a Postgraduate degree from the University of Saskatchewan, I agree that the Libraries of this University may make it freely available for inspection. I further agree that permission for copying of this thesis in any manner, in whole or in part, for scholarly purposes may be granted by the professor who supervised this thesis work or, in his absence, by the Head of the Department or the Dean of the College in which the thesis work was done. It is understood that any copying or publication or use of this thesis or parts thereof for financial gain shall not be allowed without my written permission. It is also understood that due recognition shall be given to me and to the University of Saskatchewan in any scholarly use which may be made of any material in my thesis.

Requests for permission to copy or to make other use of material in this thesis in whole or in part should be addressed to:

Head of the Department of Mechanical Engineering
57 Campus Drive
University of Saskatchewan
Saskatoon, Saskatchewan
S7N 5A9

Abstract

This thesis describes an investigation of the velocity field in a fluid around a solid sphere undergoing transient motion parallel to, and midway between, two plane walls. Particle Image Velocimetry (PIV) was used to measure the velocity at many discrete locations in a plane that was perpendicular to the walls and included the centre of the sphere. The transient motion was achieved by releasing the sphere from rest and allowing it to accelerate to terminal velocity.

To avoid complex wake structures, the terminal Reynolds number was kept below 200. Using solutions of glycerol and water, two different fluids were tested. The first fluid was 100%wt glycerol, giving a terminal Reynolds number of 0.6 which represents creeping flow. The second solution was 80%wt glycerol yielding a terminal Reynolds number of 72. For each of these fluids, three wall spacings were examined giving wall spacing to sphere diameter ratios of h/d = 1.2, 1.5 and 6.0. Velocity field measurements were obtained at five locations along the transient in each case. Using Y to denote the distance the sphere has fallen from rest, velocity fields were obtained at Y/d = 0.105, 0.262, 0.524, 1.05, and 3.15.

It was observed that the proximity of the walls tends to retard the motion of the sphere. A simple empirical correlation was fit to the observed sphere velocities in each case. A wall correction factor was used on the quasi-steady drag term in order to make the predicted unbounded terminal velocity match the observed terminal velocity when the walls had an effect.

While it has been previously established that the velocity of a sphere is retarded by the proximity of walls, the current research examined the link between the motion of the sphere and the dynamics of the fluid that surrounds it. By examining the velocity profile between the surface of the sphere at the equator and the wall, it was noticed that the shear stresses acting on the sphere increase throughout the transient, and also increase as the wall spacing decreases. This is due to the walls blocking the diffusion of vorticity away from the sphere as it accelerates leading to higher shear stresses.

In an unbounded fluid, the falling sphere will drag fluid along with it, and further from the sphere, fluid will move upward to compensate. It was found that there is a critical wall spacing that will completely prevent this recirculation in the gap between the

sphere and the wall. In the 80%wt glycerol case, this critical wall spacing is between h/d = 1.2 and 1.5, and in the 100%wt glycerol case the critical wall spacing is between h/d = 1.5 and 6.0.

Acknowledgements

The author would like to extend sincere thanks to the many people without whose support this work would not have been completed.

My supervisor, Dr. J. Bugg is both a highly valued mentor and a friend. His patience knows no bounds, although at times I seem to have tested that on a daily basis. His intellect is staggering and there was never a problem that I had that he did not help me with. I wish to thank him for his many hours of guidance. He is a credit to the teaching profession and I am lucky to have taken the chance to work with Dr. Bugg.

As well, I would like to thank the other members of my committee, Dr. Gabriel, Dr. Bergstrom and Dr. Sumner who always offered their help and expertise during my studies.

I would like to extend my gratitude to the Canadian Space Agency for funding this research.

Lastly, I would like to extend my sincere thanks to all of my family and friends who supported me during this degree. Kurt and Jenn who always had a place for me, Michael who always had wisdom to share, and Laura who was always there for me.

Table of Contents

List of Figures

List of Tables

Nomenclature

A	Projected frontal area of the sphere, [m^2]
a	Sphere radius, [m]
a, b	Curve fitting parameters for velocity history
C_D	Drag coefficient
d	Sphere diameter, [m]
$\vec{F}_T$	Total force acting on the sphere, [N]
$\vec{F}_D$	Quasi-steady drag force, [N]
$\vec{F}_m$	Force due to gravitational acceleration, [N]
$\vec{F}_B$	Buoyancy force, [N]
$\vec{F}_G$	Submerged gravity force, [N]
$\vec{F}_{AM}$	Added Mass force, [N]
$\vec{F}_H$	History force, [N]
f_H	Empirical data fit function within the history integral
f_{cyl}	Focal length for the cylindrical lens, [m]
f_{sph}	Focal length for the spherical lens, [m]
$f(h/d)$	Wall factor
g	Acceleration due to gravity, [m/s^2]
h	Spacing between the plane walls, [m]
IA	Interrogation area
$I(i, j)$	Image intensity function at location (i, j)
KE_{fluid}	Kinetic energy of the fluid, [N.m]
$K(t\text{-}s)$	History kernel
m_{AM}	Added mass coefficient
m_f	Mass of fluid displaced by sphere, [g]
m_p	Mass of the sphere (particle), [g]
p	Pressure acting on the sphere, [Pa]
p_∞	Freestream pressure, [Pa]
P	Pressure acting on the sphere normalised with the freestream pressure
r, θ	Polar coordinate system
r^*	ratio of sphere diameter to wall spacing
Re	Reynolds number
Re_T	Terminal Reynolds number
R_{12}	Cross correlation function between image 1 and 2
s	Dummy variable of integration.
$\vec{s}$	Displacement vector
s_x, s_y	Components of displacement vector
t	time, [s]
U_∞	Freestream velocity, [m/s]
U_p	Velocity of the sphere (particle), [m/s]
U_T	Terminal speed, [m/s]
u, v, w	Components of velocity vector (Cartesian)

u_r, u_θ	Components of velocity vector (Polar)
u', v', w'	Components of perturbation velocity
$\vec{V}$	Velocity field
$\vec{V}^*$	Velocity field normalised with the freestream velocity
$\vec{v}$	Perturbation velocity vector
w	Gaussian weighting function
x, y, z	Cartesian coordinate system centred on the sphere
X, Y, Z	Cartesian coordinates normalised with the sphere diameter
x_c, y_c	Coordinates of the centre of fluid rotation
Y	Coordinate attached to the release point, [m]
δz_s	Laser light sheet thickness, [m]

Greek

Ψ	Stokes stream function
ρ_f	Density of fluid, [kg/m^3]
ρ_p	Density of sphere (particle), [kg/m^3]
μ	Dynamic viscosity of the fluid, [Pa.s]
ν	Kinematic viscosity of the fluid, [m^2/s]
λ	Viscosity ratio between the droplet and exterior fluid

Chapter 1:
Introduction

1.1 Background

Fluid mechanics is a very old branch of science. Archimedes was discovering the nature of fluids long before calculus was established, and indeed while geometry itself was being born. A similar theme in the difficulty of directly observing the motion of a fluid is noted though history. Often, the motion of foreign objects carried along with the flow shows the fluid flow indirectly.

Two examples may be taken from last century: the flow past a knife edge and the flow around a spinning cylinder imaged in 1934 by Prandtl and Tietjens. These images are shown in Figures 1.1 and 1.2 respectively.

Figure 1.1: Flow passing over a knife edge from left to right. A thin sheet of light illuminates tiny shavings of aluminum in the flow. From Prandtl and Tietjens [1934], p. 295 (reprinted by Dover Publications [1957]).

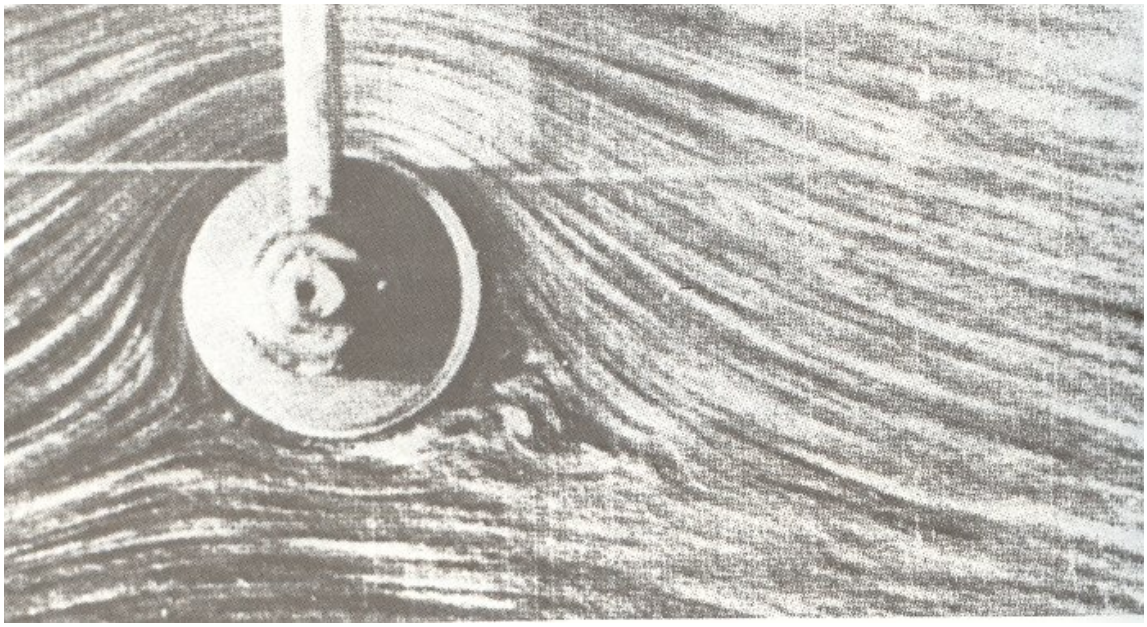

Figure 1.2: A uniform freestream flows around a rotating cylinder. Aluminum filings on the surface of the fluid show flow direction. From Prandtl and Tietjens [1934], p. 284 (reprinted by Dover Publications [1957]).

Figures 1.1 and 1.2 demonstrate that the technique of flow investigation through the imaging of tiny metal shavings is simple and effective. Such flow visualisations provide a means of observing patterns within the flow.

Further in history, in the 1730's, the same idea occurs in Reynolds' laboratory with the famous needle and dye from Reynolds' investigations into the onset of turbulence. A few more centuries into the past, one of the first sketches of fluid motion was done by Leonardo daVinci over five hundred years ago, and is shown in figure 1.3.

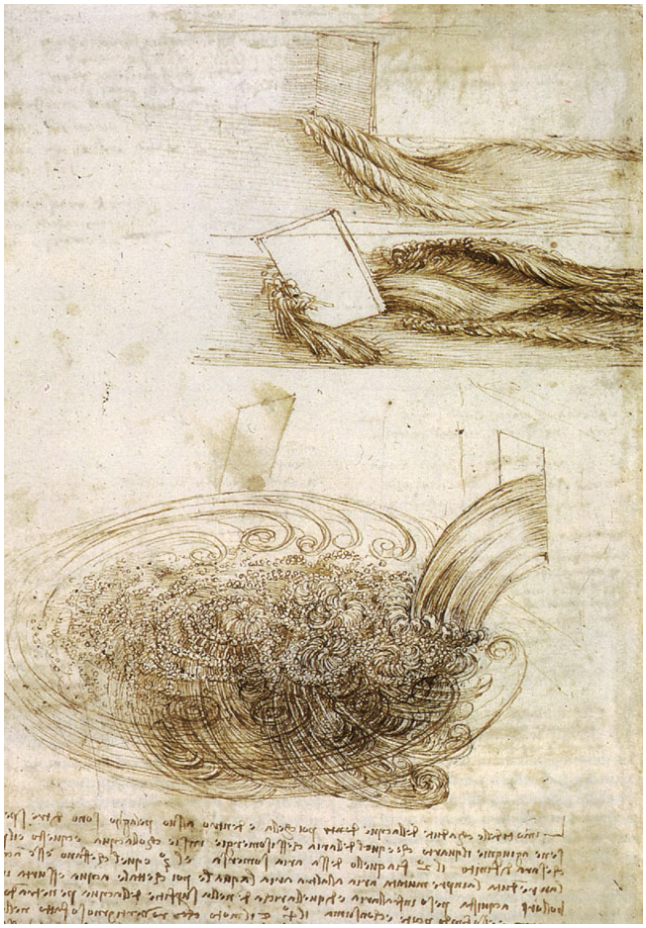

Figure 1.3: Leonardo da Vinci "Study of Water Formations" c. 1507-09. Sketches of vortices around an object in a river, and a whirlpool structure. Popham [1945], p. 281.

Again we see that the sketch of the flow is composed of a great number of individual path lines that represent how massless particles would travel through the fluid. Without the path lines, we are unable to see the motion of the fluid.

These flow visualization techniques are optically satisfying and serve to qualitatively describe the structures of the flow, however they provide only limited quantitative information required for scientific investigation. The photographic technique employed by Prandlt and Teitjens in 1934 was unavailable in da Vinci's time. Undoubtedly, each of these scientists were aware that by knowing the length of time the film was exposed and measuring the length of each streak the particle velocity could be measured. However, the obstacle in tackling such an analysis manually is the sheer number of particle streaks. Optical techniques are clearly powerful tools since the

instantaneous velocity of the whole flow field is caught in one frame. However, there exists a crisis of labour that prohibits the analysis of the complete velocity vector field from such an image by hand. Until the late 1980's, computers and image analysis software were simply not powerful enough to do the job.

Within the past decade, computers and software have become much more powerful, and with the advent of digital photography, image analysis can now be accomplished very quickly. Now, 530 years after da Vinci contemplated the river, fluid dynamics research return to this centuries-old idea with a technique called Particle Image Velocimetry (PIV). This technique allows thousands of velocity measurements to quickly be made at regular intervals in a plane within a flow field. In a PIV system, a laser light sheet is pulsed twice to illuminate a plane within the flow. The flow is seeded with microscopic particles which scatter the laser light so that their images can be recorded on a recording medium. Between the two laser pulses, the particles will move slightly as they follow the flow. By knowing the displacement of the particles and the separation time between the laser pulses, an instantaneous velocity field of the fluid carrying the particles can be determined.

In the current investigation we will use PIV to examine the flow of a viscous fluid around a solid sphere. The investigation will begin by describing well-known theories starting with steady, creeping flow and then proceeding to a mathematical treatment of flows at higher Reynolds numbers. The three specific cases for steady flow around a sphere examined in this thesis are inviscid flow theory, Stokes' creeping flow model, and Oseen's approximation which is an improvement on Stokes' model.

With an understanding of the steady solutions, we will then examine the case of transient flow around a sphere. Transient flow around a body is considerably more complex than the steady case, and there has been much work done in various research groups concerning this topic. Transient flow can exist due to the acceleration of a body within the fluid or an acceleration of the fluid itself. The present study is concerned only with the sudden acceleration of a solid, spherical particle from rest until it reaches terminal velocity. From an engineering point of view, this case is important as it models the sedimentation of particles (e.g. sand) in an essentially infinite fluid (e.g. drinking water reservoir). The infinite-fluid case has been studied and mathematical models exist

that acceptably model the motion of the sedimenting particle. However, the constrained case, where the sphere is moving parallel to solid walls, is less well understood. The present study aims not only to observe the motion of a sphere as it accelerates between plane walls due to gravity, but also to observe the motion of the fluid itself as it is set in motion by the sphere.

Observing the motion of the sphere itself has been the traditional method of analyzing the transient motion of a sphere through a fluid. However, the motion of the sphere is intimately tied to the stresses and pressure distributions acting on the sphere due to the motion of the fluid. By employing the PIV technique we may record both the motion of the sphere and the motion of the surrounding fluid, and perhaps give details of the coupling between the two.

1.2 Objectives

The general goal of this research is to examine the effect of wall proximity on the transient motion of a solid sphere through an initially quiescent fluid at low Reynolds number. The specific objectives are to:

1. Make successful PIV measurements around an accelerating sphere,
2. Quantify changes in the sphere motion due to wall proximity,
3. Identify changes in the flow structure due to wall proximity, and
4. Investigate the effects of Reynolds number on this flow.

1.3 Organisation of Thesis

The theories of steady and transient flow around a sphere will be presented in Chapter 2 and the details of the particle image velocimetry technique and the apparatus used for this experiment will be given in Chapter 3. The results and discussion will be presented in Chapter 4, and the conclusion and recommendations for future work will be given in Chapter 5.

Chapter 2:
Theory and Background

2.1 Potential Flow Theory

Potential flow theory is perhaps a peculiar place to begin an investigation of creeping flow as the former deals with the extreme case where viscous forces become zero and the latter represents the opposite extreme where viscous forces dominate. It is, however, instructive to present the inviscid theory to show where its weaknesses lie in describing real flows and how the creeping flow models are an improvement for very low Reynolds numbers. Also, boundary layer theory teaches us that inside the boundary layer, shear stresses resulting from viscosity tend to dominate, however outside of this region real fluids behave as if they were inviscid.

Begin by considering a velocity field, $\vec{V}$, given by the Cartesian vector field,

$$\vec{V} = u\hat{i} + v\hat{j} + w\hat{k}, \tag{2.1}$$

where u, v, and w are the components of velocity.

To give a complete description of the fluid motion, we must turn to the Navier-Stokes equations which govern the transport of momentum for an incompressible flow of a Newtonian fluid. In Cartesian coordinates these equations, in the x, y, and z directions respectively, are:

$$\left.\begin{aligned}
\rho_f\left(\frac{\partial u}{\partial t}+u\frac{\partial u}{\partial x}+v\frac{\partial u}{\partial y}+w\frac{\partial u}{\partial z}\right) &= \rho_f g_x - \frac{\partial p}{\partial x}+\mu\left(\frac{\partial^2 u}{\partial x^2}+\frac{\partial^2 u}{\partial y^2}+\frac{\partial^2 u}{\partial z^2}\right)\\
\rho_f\left(\frac{\partial v}{\partial t}+u\frac{\partial v}{\partial x}+v\frac{\partial v}{\partial y}+w\frac{\partial v}{\partial z}\right) &= \rho_f g_y - \frac{\partial p}{\partial y}+\mu\left(\frac{\partial^2 v}{\partial x^2}+\frac{\partial^2 v}{\partial y^2}+\frac{\partial^2 v}{\partial z^2}\right)\\
\rho_f\left(\frac{\partial w}{\partial t}+u\frac{\partial w}{\partial x}+v\frac{\partial w}{\partial y}+w\frac{\partial w}{\partial z}\right) &= \rho_f g_z - \frac{\partial p}{\partial z}+\mu\left(\frac{\partial^2 w}{\partial x^2}+\frac{\partial^2 w}{\partial y^2}+\frac{\partial^2 w}{\partial z^2}\right)
\end{aligned}\right\}. \tag{2.2}$$

where ρ_f is the fluid density, t is time, g_x, g_y, and g_z are the components of gravity, p is the pressure and μ is the viscosity of the fluid. This set of equations is closed with the continuity equation.

These equations represent a balance between convection of momentum on the left, and gravity, pressure and viscous forces on the right. It is interesting to see that the entire field of fluid dynamics can be stated so succinctly, but their neat form veils a frustrating

truth and the Navier-Stokes equations exist as one of the so-called "Millennium Problems" for which the Clay Institute of Mathematics has sponsored a one-million dollar prize for a solution. As Delvin [2003] puts it, "No one has been able to find a formula that solves the Navier-Stokes equations. In fact, no one has been able to show in principle whether a solution even exists! The most significant lesson we have learned to date is that the mathematics of fluid flow seems to be extremely hard."

However, despite their complexity, these equations are "solved" in nature every time a river flows into the ocean, or air passes over the wing of a bird. Though a full mathematical solution still eludes us, special simplifications allow closed-form solutions to exist for a number of simple geometries in simple (although not trivial) flows.

The Navier-Stokes equations may be written in vector form for the steady flow of an incompressible, Newtonian fluid as,

$$\rho_f \left(\vec{V} \cdot \vec{\nabla}\right)\vec{V} = \rho_f \vec{g} - \vec{\nabla} p + \mu \nabla^2 \vec{V} \,. \tag{2.3}$$

As the focus of this thesis is the flow around a sphere, it is convenient to work in spherical coordinates. The coordinate system is presented in Figure 2.1.

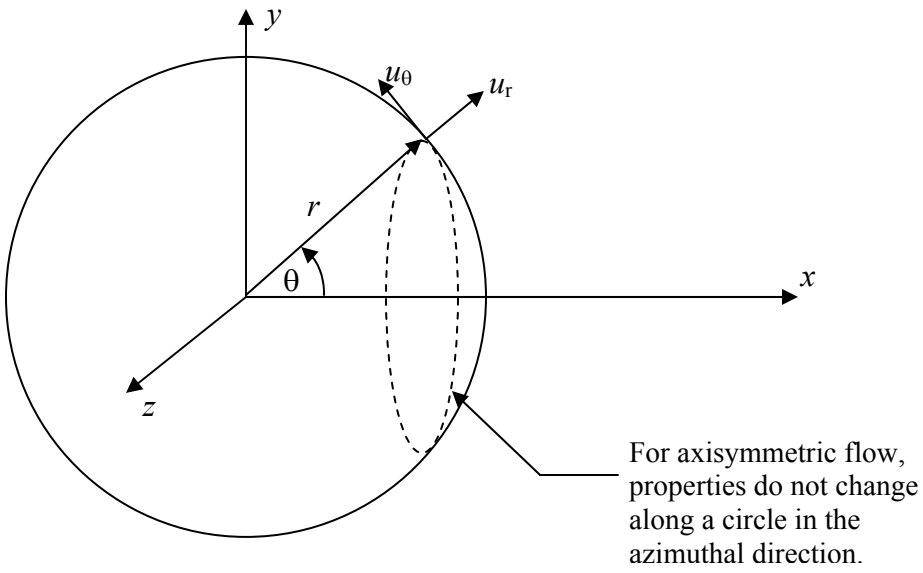

Figure 2.1: Definition of spherical coordinate system.

If the flow is axisymmetric, the two-dimensional flow field is defined by the velocity components u_r and u_θ. Equation (2.3) may be used by noting that in spherical coordinates,

$$\vec{\nabla} \cdot \vec{V} = \frac{1}{r^2}\frac{\partial\left(r^2 u_r\right)}{\partial r} + \frac{1}{r\sin\theta}\frac{\partial u_\theta(\sin\theta)}{\partial\theta} \tag{2.4}$$

and, $$\nabla^2(\ ) = \frac{1}{r^2}\frac{\partial}{\partial r}\left(r^2\frac{\partial(\ )}{\partial r}\right) + \frac{1}{r^2\sin\theta}\frac{\partial}{\partial\theta}\left(\sin\theta\frac{\partial(\ )}{\partial\theta}\right). \tag{2.5}$$

In this coordinate system, there exists a scalar function, Ψ, the Stokes stream function, such that,

$$u_r = -\frac{1}{r^2\sin\theta}\frac{\partial\Psi}{\partial\theta} \tag{2.6}$$

and, $$u_\theta = \frac{1}{r\sin\theta}\frac{\partial\Psi}{\partial r}. \tag{2.7}$$

For the case of a solid sphere of radius a submerged in a uniform freestream of inviscid fluid flowing at a velocity of U_∞ in the positive x-direction, the boundary conditions are:

(a) no penetration at the wall,

$$u_r = 0 \quad \text{at} \quad r = a, \quad \text{and} \tag{2.8}$$

(b) freestream conditions far from the sphere,

$$u_\theta = -U_\infty\sin\theta, \quad \text{and} \ u_r = U_\infty\cos\theta \quad \text{for} \quad r\to\infty. \tag{2.9}$$

Note that since this is the inviscid case, the no-slip condition at the sphere wall is not enforced. These boundary conditions are satisfied for the stream function given by,

$$\Psi = -U_\infty\left(1-\frac{a^3}{r^3}\right)\frac{r^2}{2}\sin^2\theta \quad . \tag{2.10}$$

Using equation (10) to solve for the velocity components u_θ and u_r gives,

$$u_\theta = -U_\infty\left(1+\frac{a^3}{2r^3}\right)\sin\theta, \tag{2.11}$$

and,

$$u_r = U_\infty\left(1-\frac{a^3}{r^3}\right)\cos\theta. \tag{2.12}$$

2.2 Creeping Flow Theory

Potential flow is a balance between inertia and pressure forces, whereas a balance between pressure and viscous forces governs creeping flow. The Reynolds number, *Re*, gives the dimensionless ratio of inertial forces to viscous forces as,

$$Re = \frac{\rho_f U_\infty d}{\mu}, \tag{2.13}$$

where ρ_f is the fluid density, μ is the fluid viscosity and *d* is the diameter of the sphere.

The Navier-Stokes equations may be non-dimensionalised by choosing appropriate scaling factors such as the freestream velocity, U_∞, freestream pressure, p_∞, and the diameter, *d*, of the sphere. In this way the dimensionless variables become,

Velocity: $\vec{V}^* = \frac{\vec{V}}{U_\infty}$

Length: $X = \frac{x}{d}$, $Y = \frac{y}{d}$, and $Z = \frac{z}{d}$

Pressure: $P = \frac{p}{p_\infty}$.

With these non-dimensional variables, equation (2.3) may be written as,

$$\vec{V}^*\left(\vec{V}^* \cdot \vec{\nabla}\right) = -\frac{p_\infty}{\rho_f U_\infty^2}\vec{\nabla}P + \frac{1}{Re}\vec{\nabla}^2\vec{V}^*. \tag{2.14}$$

Viscous forces vary linearly with velocity while inertia forces vary with its square. Thus, for viscous forces to be on the order of the inertia term, the Reynolds number must be near unity. For flows in which viscosity dominates inertia, the Reynolds number must be much less than one. Since the Reynolds number appears in the denominator of the viscous stress terms in equation (2.14), the lower the Reynolds number becomes, the greater is the importance of the viscous terms. In the limiting case where the Reynolds number goes to zero, the inertia terms vanish completely in comparison to the viscous terms. This is not a realistic situation, as it demands that either the velocity goes to zero, in which case the term fluid dynamics loses meaning, or that the viscosity goes to infinity in which case we have shifted into the study of solid mechanics. It is therefore generally understood that slow viscous flow, or creeping flow, is simply

restricted to *Re*<<1, although the Reynolds number will retain a finite value. In this range of Reynolds number, the fluid inertia, although not zero, is negligible compared to the viscous stresses.

For this case, the Navier-Stokes equations, in dimensional vector form, for incompressible flow of a Newtonian fluid become,

$$\vec{\nabla} p = \mu \nabla^2 \vec{V} \,. \tag{2.15}$$

By eliminating the convective derivative, the non-linearity associated with the full Navier-Stokes equations has been removed. With the non-linearity gone, the equations are now reversible meaning the direction of the velocity vector may be reversed and the equation remains the same. This means that the stream function, Ψ, must have fore and aft symmetry around a body in the flow. With the simplifications offered by Stokes flow, the stream function satisfies the biharmonic function

$$\nabla^4 \Psi = 0 \,. \tag{2.16}$$

The boundary conditions required to solve this equation for the case of axisymmetric flow around a sphere are presented in Clift *et al*. [1978]. For the case of solid spheres the boundary conditions are reported as,

(a) flow returns to freestream conditions far from the sphere,

$$\frac{\Psi}{r^2} = -\left(\frac{U_\infty}{2}\right)\sin^2\theta \,, \tag{2.17}$$

(b) fluid may not penetrate the surface of the sphere, (p subscript denotes particle)

$$\Psi = \Psi_{\mathrm{p}} = 0 \quad \text{at } r=a \tag{2.18}$$

(c) no slip at the surface of the sphere,

$$\frac{\partial \Psi}{\partial r} = \frac{\partial \Psi_{\mathrm{p}}}{\partial r} = 0 \text{ at } r=a \tag{2.19}$$

Solving equation (2.16) subject to the boundary conditions (2.17) – (2.19) gives the stream function around a solid sphere as,

$$\Psi = -\frac{U_\infty r^2 \sin^2\theta}{2}\left[1 - \frac{3a}{2r} + \frac{a^3}{2r^3}\right]. \tag{2.20}$$

From this, the velocity components of the vector field surrounding the sphere may be found using equations (2.6) and (2.7). For Stokes flow, the components of velocity are:

$$u_r = U_\infty \cos\theta\left[1 - \frac{3a}{2r} + \frac{a^3}{2r^3}\right], \quad \text{and} \tag{2.21}$$

$$u_\theta = -U_\infty \sin\theta\left[1 - \frac{3a}{4r} - \frac{a^3}{4r^3}\right]. \tag{2.22}$$

The primary difference between the inviscid solution and Stokes' solution is that the no-slip condition at the sphere is enforced in the latter case.

2.3 Oseen's Approximation

One of the difficulties of using the Stokes flow model for creeping flow is that it predicts the viscous stresses to have an effect on the velocity even at large distances away from the surface. For finite Reynolds numbers, the inertia terms that have been dropped in obtaining the Stokes flow solution tend to dominate in the region far from the sphere. The viscous forces dominate only near the surface and the creeping flow approximations are only valid over a distance on the order of *a/Re* from the surface of the sphere [Clift *et al.* 1978].

Schlichting [1979] reports that Oseen suggested that instead of neglecting the inertia terms entirely, the convective derivative could be included in a simplified form. The fluid velocity is represented as the sum of the freestream velocity, U_∞, and a perturbation velocity, $\vec{v}$, given by,

$$\vec{v} = u'\hat{i} + v'\hat{j} + w'\hat{k}\,, \tag{2.23}$$

where *u'*, *v'*, and *w'* are the components of the perturbation velocity. This perturbation velocity is small with respect to the freestream. In this way the velocity vector of the fluid surrounding the sphere can be written as,

$$\vec{V} = \left(u' + U_\infty\right)\hat{i} + v'\,\hat{j} + w'\,\hat{k}\,, \tag{2.24}$$

and the neglected convective derivative for steady flow becomes,

$$\frac{\mathrm{D}\vec{V}}{\mathrm{D}t} = \left(\vec{v}\cdot\vec{\nabla}\right)\vec{v} + \left(U_\infty \hat{i}\cdot\vec{\nabla}\right)\vec{v}\,. \tag{2.25}$$

The first term on the right hand side of equation (2.25) is small compared to the second term at large distances from the sphere, thus the non-linear first term is neglected. With the inclusion of the new, linearised inertia terms, equation (2.15) becomes,

$$\vec{\nabla}p = \mu\nabla^2\vec{V} - \rho\left(U_\infty \hat{i}\cdot\vec{\nabla}\right)\vec{v}\,. \tag{2.26}$$

As reported by Clift *et al.* [1978], equation (2.26) is generally called Oseen's equation. Although the equation is linear, the presence of the final term makes the equation irreversible, thus the fore and aft symmetry of the solution is lost. Some constraints must be put on the perturbation vector in equation (2.23) such that the original characteristics of the flow are not lost. The boundary conditions are:

(a) the flow returns to freestream conditions far from the sphere,

$$\vec{v} \to 0 \quad \text{as} \quad r\to\infty, \quad \text{and}$$

(b) the no-slip condition is satisfied at the sphere's surface,

$$\vec{v} = -U_\infty \hat{i} \quad \text{at } r=a.$$

Although equation (2.26) may not be described as the gradient of a scalar stream function in an exact solution, an approximate solution has been developed by Lamb and is given in Clift *et al.* [1978] as,

$$\Psi = -\frac{U_\infty r^2 \sin^2\theta}{2}\left[1+\frac{a^3}{2r^3}\right] + \frac{3U_\infty a^2}{Re}\left(1-\cos\theta\right)\left[1-\exp\left(-\frac{rRe}{4a}(1+\cos\theta)\right)\right]. \tag{2.27}$$

As we can see from the second term in equation (2.27), the Reynolds number appears in this stream function, which is a great advantage over Stokes' creeping flow stream function. In this way, Oseen's approximation is much better able to represent the streamlines when they deviate from the symmetrical creeping flow solution as the sphere's velocity increases, or more correctly, as the Reynolds number increases.

As before, we differentiate the stream function with respect to r and θ to obtain the radial and tangential components of the velocity within a moving fluid surrounding a stationary sphere.

Oseen predicts the velocity components to be,

$$u_r = -\frac{3U_\infty a^3}{r^2 Re} + \left(1 + \frac{a^3}{2r^3}\right)U_\infty \cos\theta + \frac{3U_\infty a}{r}\left[\frac{1}{4} - \frac{\cos\theta}{4} + \frac{a}{rRe}\right]\left[\exp\left(-\frac{rRe}{4a}(1+\cos\theta)\right)\right] \tag{2.28}$$

$$u_\theta = \left(\frac{a^3}{4r^3} - 1\right)U_\infty \sin\theta + \frac{3U_\infty a}{4r\sin\theta}\left(1-\cos^2\theta\right)\left[\exp\left(-\frac{rRe}{4a}(1+\cos\theta)\right)\right]. \tag{2.29}$$

This section discussed the steady, creeping flow around a sphere, which occurs in real fluids when the Reynolds number is much less than one. The details of the velocity field around a slowly moving sphere are now known for each of the three theories: potential flow, Stokes flow, and Oseen's approximation.

In such cases, a stream function describing the steady flow of fluid around the sphere is readily obtained. As the Reynolds number decreases, the viscous stresses become more important and the stream function becomes much more complex. Although clever manipulations have yielded stream functions for steady flows around spheres, approximations and simplifications to deal with the non-linear convective terms and also the description of the boundary conditions leads to limits of applicability in each case. The Oseen equation, for example, predicts infinite "drift" where the motion of the sphere will induce fluid motion even very far from the sphere. Using a different approach, Proudman and Pearson [1957] used different forms of the stream function appropriate in the region near the sphere and in the outer region to satisfy the conditions far from the sphere. Using a series expansion it was found that, although the technique worked reasonably well for the first two terms, the addition of subsequent terms in the expansion tends to worsen the fit to experimental data. These results led Proudman and Pearson to suggest that Reynolds number may be an unsuitable expansion parameter. A conclusion drawn by Clift *et al*. [1978] is that "analytic solutions for flow around a spherical particle have little value for $Re>1$."[p. 46] They suggest that for *Re* greater than unity, the full Navier-Stokes equations be solved numerically for the best description of the flow field, while empirical formulas be used for determining the drag coefficient.

Unsteady motion has not yet been treated within this thesis. This is important, as the interaction between the sphere and the fluid is modeled differently when the sphere is accelerating than when the sphere reaches terminal velocity. The current models in the literature will be presented in the next chapter.

2.4 Additional Effects due to Transient Motion

As we move away from the steady-flow case and examine the transient motion of a body through a fluid, we find the literature switches its focus away from the fluid itself. In the case of transient flow around an accelerating body, the focus is traditionally on the motion of the body rather than the motion of the surrounding fluid. Instead of trying to describe the motion of the fluid, the problem shifts to developing a correct form for the governing equation of motion that describes how the sphere responds to the forces acting on it from changing flow conditions.

The forces acting on the sphere are the result of the distribution of stresses and pressure in the fluid. These forces change throughout the transient as the flow patterns are being established in the fluid. In reality, there is only ever one surface "force" acting on the particle as it moves through the fluid and this is the integrated result of the state of stress and pressure acting at the surface. However, without prior knowledge of the state of stress in the fluid, it is traditional to separate the force acting on the particle into several different contributions arising from different physical phenomenon. In this way, we may add each contribution and use the sum to predict the motion of the sphere using Newton's second law,

$$\sum F = m_{\mathrm{p}} \frac{\mathrm{d}U_{\mathrm{p}}}{\mathrm{d}t}. \tag{2.30}$$

where F represents the forces acting on the particle, and m_{p} and U_{p} are the mass of the particle and its velocity.

2.5 The Forces Acting on a Submerged Sphere

In the transient case, much is borrowed from hydrostatics and steady flow theory as we begin the separation of forces acting on a body. However, in transient flow there

has been some debate over the physical significance of these divisions owing to the increased drag experienced by the accelerating sphere. The division of forces describing where to attribute this increased drag has remained somewhat arbitrary. Even so, we may begin our treatment with hydrostatics.

2.5.1 Gravity Forces

The forces due to gravity may be divided into the weight of the body owing to its mass and the buoyancy. The buoyancy force on a submerged body is the integrated effect of the hydrostatic pressure distribution acting on the surface of the body. This is equivalent to the weight of the fluid displaced by the sphere.

2.5.2 Steady Drag

As the sphere moves through the fluid, the no-slip condition at the solid interface leads to shear stresses in the fluid acting on the sphere. The integrated effect of the shear stresses acting on the surface leads to a viscous drag force. This acts in conjunction with the pressure drag, or form drag, which acts over the sphere's surface arising from the deviation of the pressure distribution from the hydrostatic pressure distribution. The overall effect of these forces in steady flow is called the steady drag force and is typically characterised by a drag coefficient, C_D, that is suited to the range of Reynolds numbers in question. The drag coefficient is typically correlated to the terminal Reynolds number (Re_T) and the graph of C_D versus Re_T is called the standard drag curve. A good summary of drag coefficients and their ranges of application is given in Clift *et al*. [1978]. For this study, the Reynolds number ranges between zero and a maximum of 72. A good drag coefficient correlation for a solid sphere that covers this range is given by the Schiller-Neumann Formula,

$$C_D = \frac{24}{Re}\left(1 + 0.15Re^{0.687}\right), \; Re < 800. \tag{2.31}$$

The overall drag force is then,

$$F_D = \frac{1}{2}\rho_f U_p^2 C_D A, \tag{2.32}$$

where U_p is the particle velocity, and A is the projected frontal area of the body.

In the steady state case, the sphere translates through the fluid at a constant speed and the weight, buoyancy and drag forces are in equilibrium. In this case, the sphere has reached terminal velocity. Using F_B, F_D, and F_m to denote the buoyancy force, the drag force and the force due to gravity, the free-body diagram appears as in Figure 2.2.

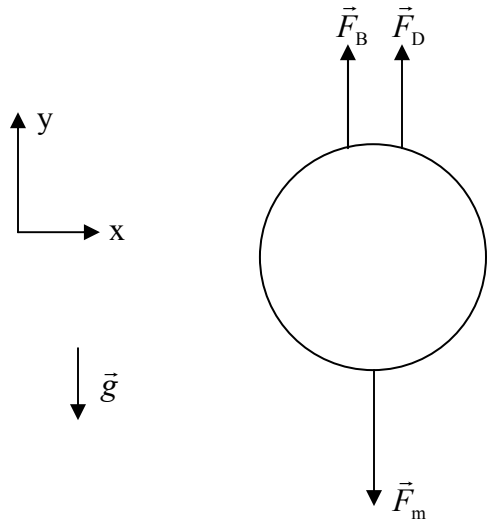

$$F_m = m_p g$$

$$F_D = \frac{1}{2}\rho U_p^2 C_D A$$

$$F_B = m_f g$$

Where,
m_p = mass of particle
m_f = mass of displaced fluid
g = acceleration due to gravity

Figure 2.2: Free body diagram of sphere at terminal velocity.

While this is valid for the steady case, there is an imbalance of forces acting on the sphere during transient motion. The effect of acceleration is to increase the force retarding the motion of the sphere. The effects of the modifications to the drag term must decay and the steady drag must be restored as the sphere approaches terminal velocity. It is here that the separation of the contributions to the unsteady drag becomes somewhat arbitrary.

The first classical result was derived from the unsteady Stokes equation by Basset in 1888 and, as reported by Clift *et al*. [1978], is typically called the BBO equation for work done by Basset in 1888, Boussinesq in 1903, and Oseen in 1927. Leaving the details for subsequent sections, the forces acting on the accelerating sphere were separated into four contributions as follows:

$$m_p \frac{dU_p}{dt} = F_G + F_D + F_{AM} + F_H . \qquad (2.33)$$

The terms on the right hand side of equation (2.33) are, respectively: the submerged gravity force F_G, the quasi-steady drag force F_D at the instantaneous sphere velocity, the added mass force F_{AM} due to the added inertia from acceleration of the surrounding fluid, and the history force F_H that results from the diffusion of vorticity generated at the surface of the sphere into the surrounding fluid as the sphere accelerates. In this way the gravitational and steady drag forces are retained respectively from hydrostatics and steady flow, and the effects of unsteadiness are merged into the remaining two terms.

2.5.3 The Added Mass

The first of these additional forces is called the added mass force, or alternatively the virtual mass or hydrodynamic mass. This force arises from the fact that, as the body accelerates through the fluid, the fluid itself must also be accelerated. This causes the body to behave as though it were more massive than if it were accelerating in a vacuum. The amount that the body appears to exceed its "in vacuum" mass is referred to as the "added mass". A balance between the forces acting on the body and the resulting acceleration must include the effect of the added mass as follows,

$$\sum F = \left(m_p + m_{AM}\right)\frac{dU_p}{dt}, \tag{2.34}$$

where F are the forces acting on the body, m_p and U_p are the mass of the particle and its instantaneous velocity, respectively, and m_{AM} is the added mass due to the acceleration of the surrounding fluid.

The added mass can be found by evaluating the total kinetic energy of the fluid moving relative to the body and then equating this with an equivalent kinetic energy of the body at the instantaneous velocity, U_p. Knowing the kinetic energy and the particle velocity allows the added mass to be determined. As reported by Magnaudet [1997], the added mass is the same for both creeping flow and for inviscid flow.

The kinetic energy of the fluid may be determined by using potential flow theory. In the case of a sphere moving through an otherwise stationary fluid, the velocity field is obtained from superimposing a freestream and a spherical doublet. The case of a sphere moving through a quiescent fluid is shown in Figure 2.3, along with an element of fluid mass.

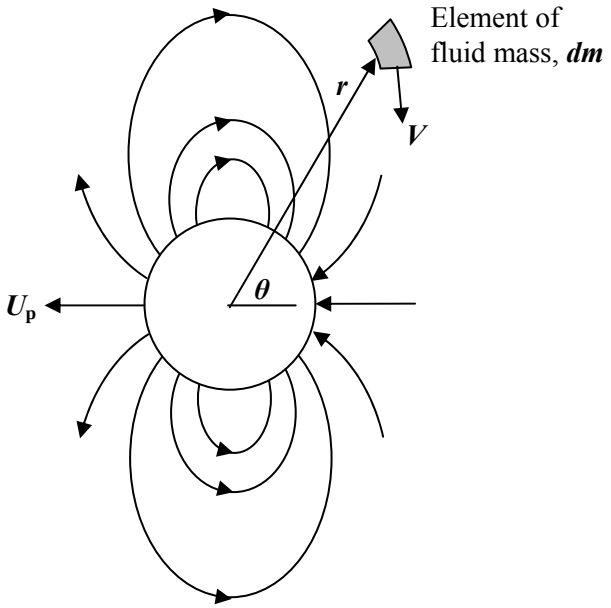

Figure 2.3: Potential flow streamlines around a moving sphere showing an element of fluid mass.

The total kinetic energy of the fluid surrounding the sphere may be found by integration. The velocity of the fluid element relative to a stationary observer can be represented by a sum of the velocity components in the radial, r, direction and angular, θ, direction in spherical coordinates. In these coordinates, the velocity components are,

$$u_r = -\frac{U_\mathrm{p} a^3 \cos\theta}{r^3}, \quad \text{and } u_\theta = -\frac{U_\mathrm{p} a^3 \sin\theta}{2r^3}, \tag{2.35}$$

where a is the radius of the sphere, and r and θ are the radial and angular location of the fluid element. Using this coordinate system, the fluid element has a mass of,

$$\mathrm{d}m = \rho_\mathrm{f} (2\pi r \sin\theta) r \,\mathrm{d}r \,\mathrm{d}\theta \ , \tag{2.36}$$

where ρ_f is the density of the fluid. The kinetic energy of the fluid is then,

$$KE_\mathrm{fluid} = \int \frac{1}{2} V^2 dm, \tag{2.37}$$

where,

$$V^2 = u_r^2 + u_\theta^2 .$$

The result is,

$$KE_{\text{fluid}} = \frac{1}{3}\rho\pi a^3 U_{\text{P}}^2 . \tag{2.38}$$

The "added mass" is the mass, which when traveling at a velocity U_{p}, would have the same kinetic energy as the fluid. This can be stated as,

$$KE_{\text{fluid}} = \frac{1}{2} m_{\text{AM}} U_{\text{p}}^2 . \tag{2.39}$$

Thus for a spherical particle, the added mass is,

$$m_{\text{AM}} = \frac{2}{3}\rho\pi a^3 , \tag{2.40}$$

which is one-half of the mass of fluid displaced by the sphere. The value of one-half of the displaced mass is referred to as the added mass coefficient.

While this analysis is valid for potential flow, in which the viscosity of the fluid is zero, one must question whether the unsteady flow of a fluid with finite viscosity around a sphere will have the same added mass coefficient. Due to the viscosity of the fluid, the no-slip condition is enforced at the surface of the sphere and the fluid experiences a shearing action as a result of the motion of the sphere. In this case, the streamlines do not appear exactly as in Figure 2.3, but rather, the fluid tends to rotate about a point of zero fluid velocity that is off the surface of the sphere.

It has been found by using the Stokes solution for creeping flow and a similar analysis of equating the kinetic energy of the fluid to an equivalent mass, that the added mass coefficient of one-half remains valid. In fact, Magnaudet [1997] reports that in a DNS investigation by Rivero [1991], the added mass coefficient is equal to 0.5 for Reynolds numbers between 0.1 and 1000. Further, Magnaudet [1997] and Legendre [1996] independently show that the added mass coefficient "remains constant and equal to 0.5 whatever the flow parameters…and is a general result for a spherical body, whatever its physical nature."

Since the added mass coefficient is the same for both zero and infinite Reynolds number, it must account for changes in the pressure distribution and not the distribution of shear stresses acting on the sphere.

2.5.4 The History Force

The history force is the result of the finite amount of time required for additional vorticity to be transported away from the surface of the accelerating body. As the solid body accelerates, the no-slip condition at the surface means that the velocity gradient near the surface also increases. Due to the viscosity of real fluids, this disturbance will take time to be communicated through the rest of the medium. This effect is present for the entire transient phase while a body is changing its velocity, thus the effect is cumulative and depends on the entire velocity history of the accelerating body over the time taken to reach the final velocity from the initial velocity. The total force is the integrated effect over the duration of acceleration, and is called the history force.

The integrand of the history force depends upon the flow conditions, the shape of the body and the mode of acceleration of the body. Within this integrand the history kernel is a weighting function that attempts to account for the instantaneous force acting on the accelerating particle as vorticity is transported into the surrounding fluid through both diffusion, which is a slow process, and convection, which can occur much more quickly. It is for this reason that the history kernel is often very sensitive to Reynolds number for flows extending beyond the creeping flow limit.

The general form of the history force for a sphere of diameter d is,

$$\vec{F}_{\mathrm{H}}(t) = \mu d \int_0^t K(t-s)\left(\frac{\partial \vec{U}_{\mathrm{p}}}{\partial s} - \frac{\partial \vec{V}}{\partial s}\right) \mathrm{d}s \tag{2.41}$$

where μ is the fluid viscosity, V is the "undisturbed" fluid velocity evaluated at the centre of the sphere, and the term $K(t\text{-}s)$ is the history kernel. In this experiment, the fluid is at rest and derivative of V is zero. The integration occurs over s, which is a dummy variable of integration, and begins at time t=0 when the acceleration starts and continues to any time, t.

Boussinesq and Basset were the first to evaluate the history kernel in 1888, but this was based on the study of creeping flow and is only valid in the creeping flow range. Mei and Adrian [1992] presented a history kernel dependent upon Reynolds number for spherical particles that is valid for Reynolds numbers up to 100. This history kernel is given as,

$$K(t-s)=3\pi\left\{\left[\frac{4\pi(t-s)\nu}{d^2}\right]^{\frac{1}{4}}+\left[\frac{\pi\left|U_{\mathrm{p}}-V\right|^3}{d\nu f_H^3(Re_s)}(t-s)^2\right]^{\frac{1}{2}}\right\}^{-2}, \tag{2.42}$$

where ν is the kinematic viscosity of the fluid. The function f_H is an empirical data fit which, for a suddenly accelerated solid sphere, is given by Mei and Adrian [1992] as,

$$f_H(Re)=0.75+0.105Re, \tag{2.43}$$

based on the instantaneous Reynolds number.

It can be noted that the upper bound of the history integral, *t*, is itself a variable which means that as time continues, so too does the interval of integration. The negative exponent in the history kernel leads to singularities when the time variable, *t*, is equal to the dummy variable of integration, *s*.

2.5.5 Summary of Transient Motion

If the subscript "p" denotes the particle properties and subscript "f" denotes those of the fluid, the overall equation of motion that describes the motion of a sphere as it accelerates due to gravity is the sum of all of the forces described and is given by,

$$\begin{aligned}\frac{\pi}{6}\rho_{\mathrm{p}}d_{\mathrm{p}}^3\frac{\mathrm{d}U_{\mathrm{p}}}{\mathrm{d}t}&=\frac{\pi}{6}d_{\mathrm{p}}^3(\rho_{\mathrm{p}}-\rho_{\mathrm{f}})g-\frac{1}{2}\rho_{\mathrm{f}}AU_{\mathrm{p}}^2\frac{24}{Re}\left(1+0.15Re^{0.687}\right)-\frac{1}{2}\frac{\pi}{6}\rho_{\mathrm{f}}d_{\mathrm{p}}^3\frac{\mathrm{d}U_{\mathrm{p}}}{\mathrm{d}t}\\&-3\pi\mu d_{\mathrm{p}}\int_0^t\left\{\left[\frac{4\pi\nu(t-s)}{d_{\mathrm{p}}^2}\right]^{\frac{1}{4}}+\left[\frac{\pi\left|U_{\mathrm{p}}(s)\right|^3(t-s)^2}{\nu d_{\mathrm{p}}\left[0.75+0.105Re_i(s)\right]^3}\right]^{\frac{1}{2}}\right\}^{-2}\frac{\mathrm{d}U_{\mathrm{p}}}{\mathrm{d}s}\mathrm{d}s\end{aligned} \tag{2.44}$$

The presence of the history integral is problematic since it means that a closed form solution of the equation of motion is not possible. The equation of motion is non-linear not only due to the implicit form of the quasi-steady drag coefficient, where the instantaneous Reynolds number appears, but also because during the transient portion of the motion, the instantaneous velocity is dependent upon the integrated effects of the entire velocity history of the transient. A numerical method is necessary to solve the equation of motion.

2.6 Flow Regimes for a Sphere at Higher Reynolds Numbers

The objective of this research is to study the flow of fluid around a sphere in the creeping flow regime, where Reynolds number, *Re*, is less than unity, and also for Reynolds numbers up to 100. This range of Reynolds numbers was chosen to ensure that the flow remains axisymmetric in the unbounded case, and avoids the periodic shedding of vorticity associated with higher Reynolds numbers. It is, however, instructive to list the range of flow regimes associated with a sphere at higher Reynolds numbers.

a. Unseparated flow. The boundary layer remains fully attached to the sphere in the range of $1 < Re < 20$. By $Re = 10$ the fore-and-aft asymmetry in the streamlines becomes apparent.
b. Onset of separation. The boundary layer first begins to separate from the rear stagnation point at approximately $Re = 20$. The separation is indicated by a change in the sign of vorticity.
c. Steady wake region. The point of boundary layer separation moves forward on the sphere as Reynolds number increases in the range of $20 < Re < 130$. Both the width and the length of the recirculating wake increase as *Re* increases. At approximately $Re = 35$ the wake changes from a convex to a concave shape.
d. Onset of wake instability. In the range of $130 \leq Re \leq 400$, the generation of vorticity at the surface of the sphere surpasses the diffusion and convection of vorticity away from the sphere. As a result, discrete pockets of vorticity begin to be shed from the wake. At approximately $Re = 270$, large vortices form periodically and move downstream.
e. High subcritical Reynolds number range. In the range extending from $400 < Re < 3.5 \times 10^5$, a regular succession of vortices are shed as loops from alternate sides of a plane which precesses slowly around the axis of motion. From $Re = 400$ to about $Re = 3 \times 10^5$, the wake appears as a pair of helical vortex filaments, since the separation point rotates around the sphere at the vortex shedding frequency.
f. Critical transition and supercritical flow. Critical transition occurs as Reynolds number increases beyond $Re = 2 \times 10^5$ and the separated shear

layer becomes turbulent. Due to enhanced momentum transfer, the turbulent boundary layer is able to withstand the adverse pressure gradient past the equator of the sphere and separation is delayed. As a result, there is a large drop in the form drag in this range and the drag coefficient falls from 0.5 at $Re = 2 \times 10^5$ to 0.07 at $Re = 4 \times 10^5$. As Re increases further, the separation angle on the sphere widens again and the drag coefficient rises towards a constant value of approximately 0.19.

2.6 The Influence of Walls on the Motion of a Sphere

Up until this point we have focused on the translation of solid spherical particles through an unbounded, or infinite, viscous fluid. However, it is also of engineering interest to study the case where the particles are interacting with other particles or also the walls of containing vessels. We will consider the case of a single solid sphere centred between, and moving parallel to, two plane walls as shown in Figure 2.4. The variable, h, is the distance between the parallel walls.

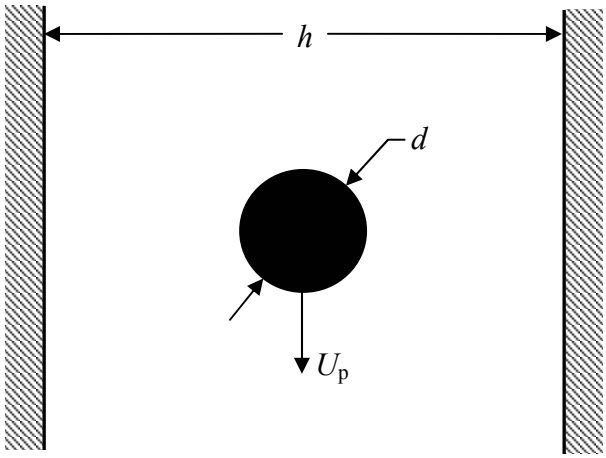

Figure 2.4: Sphere translating parallel to two plane walls at the midpoint.

Classically, this problem has been addressed by first considering Stokes' creeping flow solution, and then modifying the steady drag force term with a wall correction factor. This modification is typically expressed in terms of the ratio of wall spacing to sphere diameter (h/d, or its reciprocal) and accounts for the increased drag experienced by the sphere due to the proximity of the walls.

The general creeping flow problem of a sphere moving parallel to a plate, or between plates, was treated in 1923 by Faxen. Happel and Brenner [1973] present a mathematically rigorous review of Faxen's method of reflections. In this method, a general form of Stokes' solution for a sphere translating in an unbounded medium is solved simultaneously with functions reflected such that the sum of the solutions will cancel the original Stokes field at the walls. The result, from two reflections at each wall,

is six simultaneous equations in terms of nine unknowns, which are solved by applying continuity. Faxen used this method to determine the increased drag due to the presence of the walls for steady, creeping flow in the general case where the sphere is arbitrarily spaced between the plates. For the special case where the sphere lies at the midpoint, Faxen obtained,

$$F_D = -\frac{3\pi\mu d U_p}{1 - 1.004(d/h) + 0.418(d/h)^3 + 0.21(d/h)^4 - 0.169(d/h)^5}. \qquad (2.45)$$

In this expression the numerator is the drag force obtained by Stokes and the denominator is the wall correction factor.

There have been few experimental investigations into wall effects for containing vessels other than circular cylinders. However, using prismatic tanks of triangular, square, and semi-infinite parallel plate cross sections, Miyamura *et al.* [1980] conducted creeping flow experiments to examine the wall effects of these geometries on the steady motion of sedimenting spheres. Employing ball bearings of various diameters between 1 mm and 9 mm, dropped in a very viscous aqueous millet jelly, Miyamura *et al*. achieved results in a range of Reynolds number between 0.000241 and a maximum of 0.699. They characterised the effect of the wall by the relationship between the free settling velocity, U_F, to the settling velocity, U_w, observed when the sphere velocity was effected by the walls. His results, along with those of Faxen are given in figure 2.5. In the case of parallel plates, the wall effects are given as a function of the ratio $r^* = d/h$. In this figure, the triangular data points represent settling runs where the ball bearing was noticed to be rotating, but as Miyamura states, these cases were quite rare.

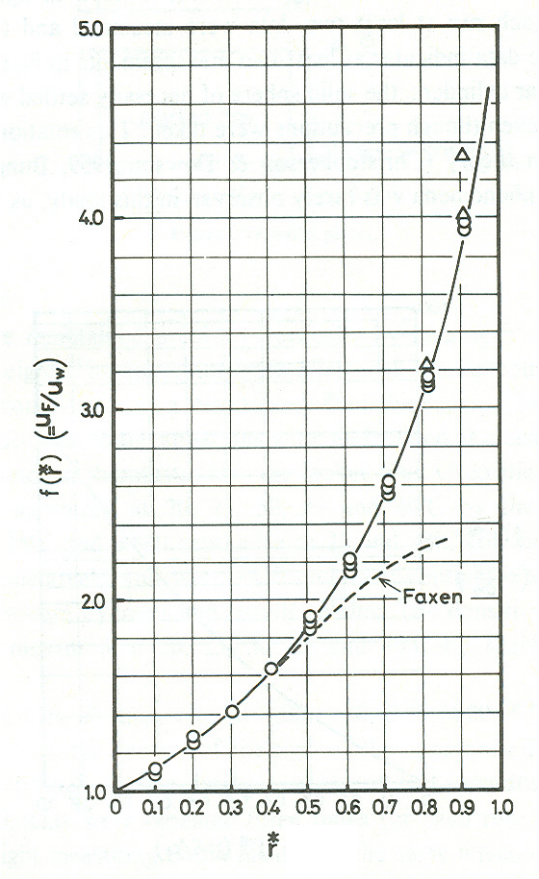

Figure 2.5: Experimental results of Miyamura *et al.* [1980] for a sphere descending midway between parallel plates showing the wall correction factor as a function of dimensionless wall spacing. Reprinted from the *International Journal of Multiphase Flow*, volume 7, Miyamura, A., Iwasaki, S., and Ishii, T., "Experimental Wall Correction Factors of Single Solid Spheres in Triangular and Square Cylinders, and Parallel Plates", pp. 46-47, Copyright (1980), with permission from Elsevier.

The relation that Faxen gives is observed to fit the data quite well up to $r^* = 0.4$, but deviates significantly thereafter. Miyamura *et al*. used a least-squares method to fit a polynomial to the experimental data to come up with a 19th order data fit given by,

$$f\left(r^*\right) = \frac{1}{R_o + R_1 \cdot \left(r^*\right) + R_2 \cdot \left(r^*\right)^2 + \ldots + R_{19} \cdot \left(r^*\right)^{19}} . \tag{2.46}$$

The coefficients of this equation, R_0 to R_{19}, are available in Miyamura *et al.* [1980]. This formula, although purely empirical, appears to do a very good job of correcting the motion of a sphere undergoing steady, creeping translation between walls.

Shapira and Haber [1988] generalized the creeping motion of any viscous sphere moving steadily between two parallel plates by using the method of reflections given by Faxen. By defining the viscosity ratio, $\lambda=\mu_{interior}/\mu_{exterior}$, any droplet may be examined. In this case, a viscosity ratio of infinity would represent a solid sphere, while near-zero would represent a gaseous bubble. The resulting drag force is given in terms of *d/h*, and the drag coefficient. For the case of a solid sphere where $\lambda = \infty$, the drag force is presented as:

$$F_{\mathrm{D}} = -12\pi\mu d U_{\mathrm{p}}\left(1+\frac{3}{4}\frac{d}{h}C_{\mathrm{D}}\right), \tag{2.47}$$

where the drag coefficient is given by a very complex function of hyperbolic transcendentals in an appendix to the Shapira and Haber [1988] paper. They also present a table of results offering a comparison of this function to Faxen's which tends to agree very well for the case of solid spheres. As expected, the drag coefficient reaches a minimum when the sphere is traveling at the midpoint between the plates.

In a 1961 paper on creeping flow near a single wall, Wakiya [1961] presents the results for the unsteady case by solving the unsteady form of the Stokes equation. The method of reflections is used with a Laplace transform with respect to time. Happel and Brenner [1973] explain the details of Wakiya and present a first approximation result of the force at time *t* acting on an impulsively started sphere as,

$$\frac{F}{3\pi\mu d U_{\mathrm{p}}} = 1+\frac{9}{16}\frac{d}{h}+\frac{1}{16}\frac{dh^2}{\sqrt{\pi}\left(\sqrt{\nu t}\right)^3}. \tag{2.48}$$

For large times, this reduces to the steady state case. For the case in which only a short time has elapsed, or the sphere is a long distance from the wall, a slightly different form is used. The expression in this case is,

$$\frac{F}{3\pi\,\mu d U_{\mathrm{p}}} = 1+\frac{d}{2\sqrt{\pi\nu t}}+\frac{9}{32}\frac{2d}{h}\left(\frac{4\nu t}{3h^2}\right). \tag{2.49}$$

The difference between these two equations rests on a series expansion based on a dimensionless group given by,

$$\kappa = \frac{h}{2\sqrt{\nu t}}. \tag{2.50}$$

For the case where $\kappa < 1$, the first equation is used, and for $\kappa > 1$ the second is used. As an overall result, the effect of the wall is to cause a more rapid decay of the unsteady terms and the sphere velocity approaches steady state more quickly.

Chapter 3:
Apparatus and Instrumentation

3.1 Introduction

The experiments were designed to investigate the transient velocity field around a solid sphere accelerating from rest to terminal velocity between parallel plane walls. The observations were carried out using the dual-frame PIV technique. The effect of the plane walls was investigated by using a tank with a movable wall. With this variability in tank geometry, the tank could be set up to represent a semi-infinite fluid or have any prescribed wall proximity. In addition, the fluid properties were varied by using different solutions of glycerol and water. The following sections describe the various components of the apparatus and instrumentation, which include the tank, the digital camera, the test fluids, the seeding particles, the solid sphere, and the particle image velocimetry system.

3.2 Test Tank

The experiments were conducted in a glass rectangular tank with base dimensions of 207 mm x 163 mm and a depth of 242 mm. The tank was filled with various solutions of glycerol and water which allowed the viscosity of the mixture to be controlled. The viscosity of the fluid and the spacing of the walls are independent variables. Altering the viscosity changes the terminal velocity of the falling sphere and also the terminal Reynolds number achieved.

3.3 Sphere

The solid sphere is made of nylon and is 19.07 mm in diameter. A small hole was drilled through the centre of the sphere and filled with lead to increase the sphere's density. The sphere was initially suspended submerged near the top of the tank from a pneumatic release mechanism as shown in Figure 3.1. The sphere was positioned such that the light sheet coincided with the centre of the sphere and such that only one half of the sphere appears in the field of view. By positioning the sphere in this fashion, a larger portion of the flow field could be captured. The properties of the sphere are given in table 3.1.

Table 3.1: Properties of test sphere

Mass, m_p	5.056 g
Diameter, d	19.07 mm
Density, ρ_p	1392.38 kg/m^3

3.4 Sphere Release Mechanism

The sphere was initially submerged and held in place near the top of the tank by means of a pneumatic holder. A small rubber cup was manufactured using the sphere itself as a partial mould. This ensured a reliable seal for the suction device. The rubber cup was fixed to the end of a 2.11-mm-diameter stainless steel tube which was mounted vertically between a pair of traversing rails at the top of the tank. The traversing rails allowed the sphere release mechanism to be positioned midway between the parallel plane walls. The steel tube could be raised or lowered into the tank, which allowed the sphere release point to be varied with respect to the camera. This ensured that PIV measurements could be made around the sphere at many points along the transient.

3.5 Trigger Laser

A laser pointer was attached to one wall of the tank, casting a horizontal beam through the field of view and shining on a photo-resistor on the other side of the tank. The purpose of this laser was to trigger the PIV system when the sphere broke the laser beam. By doing this, the sphere was in a predictable location in each PIV frame and the data from several frames could be analyzed and averaged. This reduced the effect of spurious vectors and smoothed the data set.

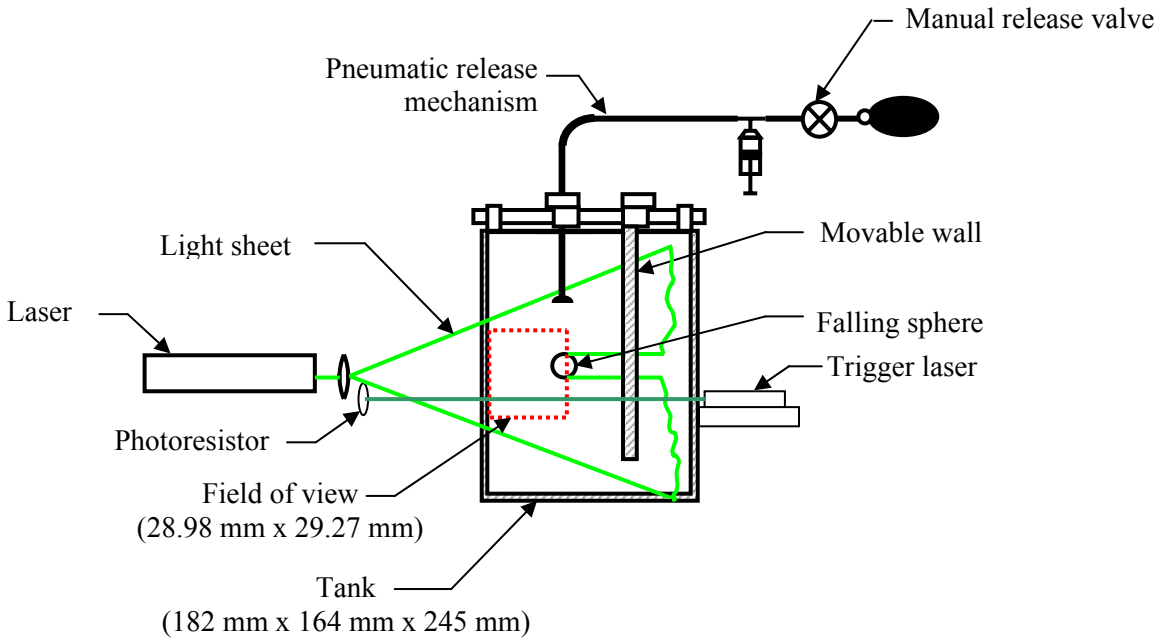

Figure 3.1: Schematic representation of apparatus showing the arrangement of the test tank, the PIV illumination laser, the trigger laser, the movable wall, and the release mechanism.

3.6 Test fluids

The fluid used in this experiment was a mixture of glycerol and water. This is a good choice for the study of low Reynolds number flow ($Re < 200$) as its viscosity is very high and it forms a homogeneous mixture with water. Any viscosity between that of pure water and 100% glycerol may be achieved. This mixture is also favourable for PIV work for its optical clarity.

Two different test fluids were used. The first was pure glycerol which had a very high viscosity and resulted in a terminal Reynolds number of 0.6 that approximated creeping flow. The second fluid was a mixture of 80%wt glycerol and 20%wt water. The properties of this fluid put the terminal Reynolds number near Re=100. It was desirable to keep Reynolds number below 200 to avoid complex wake structures involving vortex shedding.

The experiments were carried out at a temperature of 25 ^{o}C, however, due to the equipment running during the tests, the temperature was found to vary by a few degrees. This is a problem since the properties of glycerol are very sensitive to changes in

temperature and concentration. It was found that it was impossible to accurately gauge the viscosity of a mixture of test fluid based solely on the tabulated information from the Glycerin Producers Association [1963]. Thus, a Brookfield viscometer was employed to directly measure the viscosity of each fluid for each test. The density did not show such high variability with temperature and was measured by weighing the mass of fluid in a 100 mL calibrated volume flask with an Ohaus Adventurer, 210 g maximum capacity electronic scale. With the measured viscosity and density values, the terminal velocity, U_T and terminal Reynolds number, Re_T, could be predicted by using three equations recursively. The drag coefficient for a sphere in the range $Re \leq 800$ is given by the Schiller-Neumann formula,

$$C_D = \frac{24}{Re}\left(1 + 0.15Re^{0.687}\right). \tag{3.1}$$

A starting value is chosen as an initial guess for Reynolds number which is then used to calculate the drag coefficient. This is then used to calculate the terminal velocity using,

$$U_T = \sqrt{\frac{4gd\left(\rho_p - \rho_f\right)}{3\rho_f C_D}}. \tag{3.2}$$

Finally, this value is used to calculate a new Reynolds number using,

$$Re_T = \frac{\rho_f U_T d}{\mu}, \tag{3.3}$$

which is used to calculate a new drag coefficient. This process is repeated until the solution converges. Typically ten iterations were used to find U_T and Re_T. Two different concentrations of fluid mixture were tested giving terminal Reynolds numbers of Re_T = 0.6 for 100%wt glycerol and Re_T = 72 for 80%wt glycerol. Information about the fluid properties and the predicted terminal velocity and Reynolds number are summarised in Table 3.2.

Table 3.2: Properties of the test fluids (25^{o}C)

Concentration wt% Glycerol	**Density, ρ [kg/m^3]**	**Viscosity,μ [Pa.s]**	***Re*$_T$**	**U_T [m/s]**
100	1255.4	1.000	0.6	0.0245
80	1206.3	0.0572	72	0.1714

3.7 Introduction to Particle Image Velocimetry (PIV)

As we saw in the introduction, flow visualization is perhaps the oldest research tool for the investigation of moving fluids. By observing points as they move along with the fluid we may observe the flow patterns over an extended field. This is very satisfying to the eye and is useful for revealing characteristics of the flow, although these observations are often of limited use in science and engineering as they are of a qualitative nature. However, with the aid of PIV, the missing quantitative aspect has at last been married to the visually pleasing, whole-field flow visualisation. A comprehensive review of PIV is given in Raffel *et al*. [1998].

Using this technique, velocity measurements can quickly be made at thousands of discrete locations over the entire field of view. With the use of digital cameras and computers, processing the information into a vector map takes only minutes. This technique will be used to investigate the flow around an accelerating sphere.

There are several different arrangements of PIV systems available. These are mainly differentiated by the concentration of tracer particles and by the recording medium employed. Regardless of which arrangement is used, every PIV system is composed of at least six parts: a source of illumination, light sheet optics, seeding particles, recording optics, recording medium, and image analysis software. A general arrangement of these components is given in Figure 3.2.

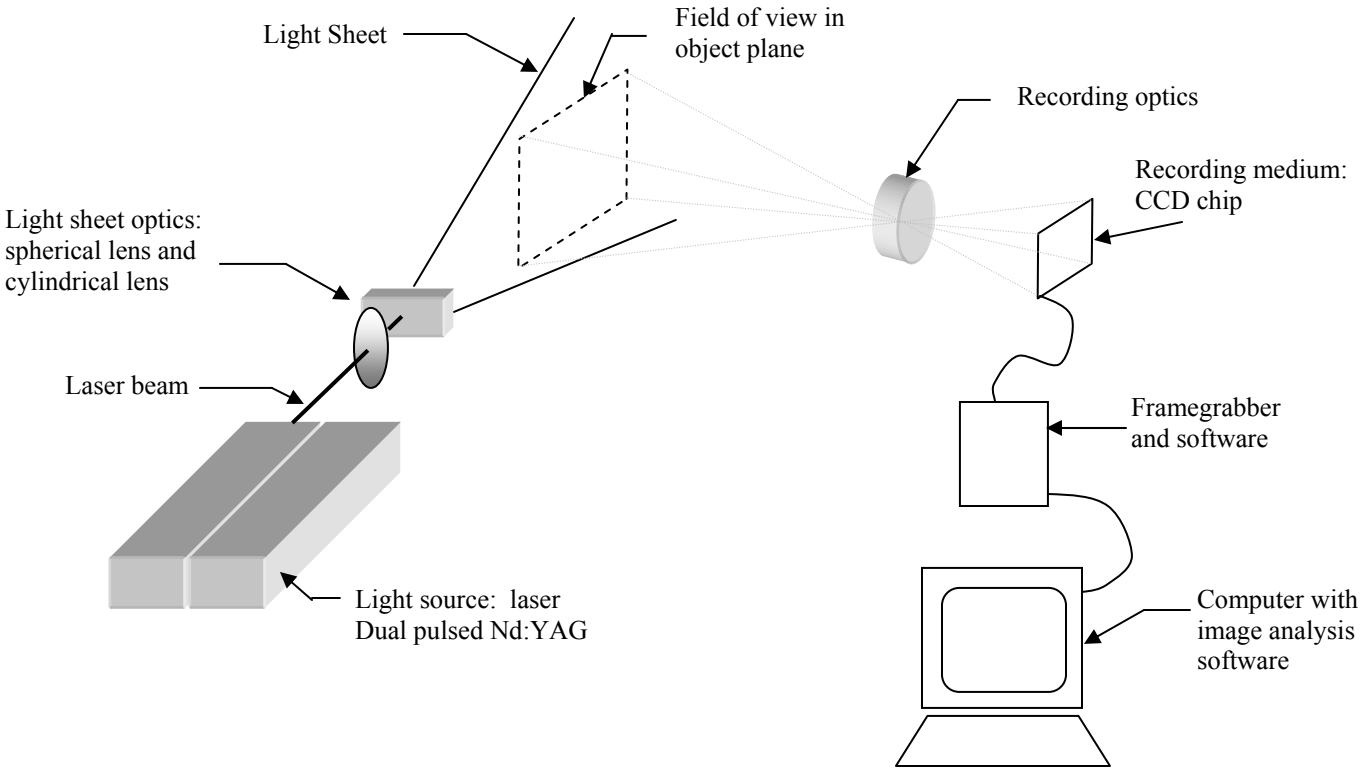

Figure 3.2: Typical layout of PIV components

The theory behind PIV is very simple. In essence, we put something that we can see into the fluid that is small enough to accurately track the fluid motion. The motion of the fluid, which we cannot see, is inferred by the motion of the tracking particles which we can see. A picture is taken at time t, and a second at time $t+\Delta t$, where Δt is a small time interval. By knowing the time interval Δt between the two exposures and measuring the displacement of the particles between the first and second image, a velocity magnitude and direction can be determined.

If the concentration of seeding particles is low, then particle pairs may be located and the analysis is very much like that just described. This is called particle tracking velocimetry (PTV). If the seeding concentration is increased, the spatial resolution of the measurements is also increased, but it becomes difficult to match particle pairs between

the two images. This case is called particle image velocimetry (PIV) and the displacement of groups of particles must be determined through statistical methods.

By using a CCD (charged couple device) camera we are able to advance frames in the very short time interval (on the order of microseconds) between image exposures. This allows the two images to be located on separate frames which removes the directional ambiguity associated with single-frame PIV techniques. Among other desirable traits, dual-frame PIV allows the measurement of velocities with zero magnitude.

3.8 Seeding of the Fluid

One of the most important concerns when doing PIV experiments is the choice of seeding particles. It is the particles themselves that will be observed rather than the fluid. If the fluid motion is to be measured, the seed particles must be small enough to faithfully follow the flow. However, the smaller the seed particles become, the less light they will scatter thus making it difficult to capture images of the particles with a camera. So there is a trade off in that the particles must be large enough to scatter enough light energy to produce clear images, yet small enough to follow the motion of the fluid.

The particles chosen for this experiment were polystyrene spheres with a mean diameter of 30 μm. The settling velocity of these particles in the 80%wt glycerol is on the order of 10^{-6} m/s. The spheres were impregnated with Rhodamine dye which gave these particles the unique property of fluorescence. When the fluorescent particles are illuminated with a certain wavelength of light, in this case the 532 nm laser light, the material emits a different wavelength of light, around 590 nm.

Laser light which reflects off the sphere and other surfaces tends to overwhelm the camera and obscure the images of the seed particles making image analysis impossible. With the fluorescent particles, a filter could be placed in front of the camera lens to filter out the laser light while letting only the light from the fluorescent particles pass through to the camera. This eliminates overexposure and allows successful image analysis to be conducted. As well, the sphere was painted black to minimise laser light reflected from the sphere surface.

3.9 Illumination

The source of illumination employed for this experiment was a New Wave Research Inc. MiniLase III, dual Nd:YAG laser. This laser emits long wavelength radiation that is frequency doubled to 532 nm, which is green in the visible spectrum. At this wavelength each pulse has a duration of 6 ns and energy of 50 mJ/pulse. A laser of this type must recharge between pulses and the pulse repetition rate is 15 Hz. This is too slow for PIV. Therefore, two identical lasers are used so that the pulse separation can be made arbitrarily short. The time between the pulse pairs is still limited by the recharge rate of 15 Hz. A Berkley Nucleonics Inc. 500B pulse generator programmed from a microcomputer controls the pulse timing.

The light emerges from the laser as a cylindrical beam with a diameter of about 3 mm. To create the light sheet necessary the beam was reduced in diameter with a spherical lens, and then diverged in one direction with a cylindrical lens. The focal length of the spherical lens was $f_{sph} = 0.25$ m at which point the beam thickness was reduced to $\delta z_s = 0.056$ mm. The focal length of the cylindrical lens was $f_{cyl} = -6.4$ mm giving a divergence angle of $\theta = 13^o$. A schematic of the light sheet optics is given in Figure 3.3.

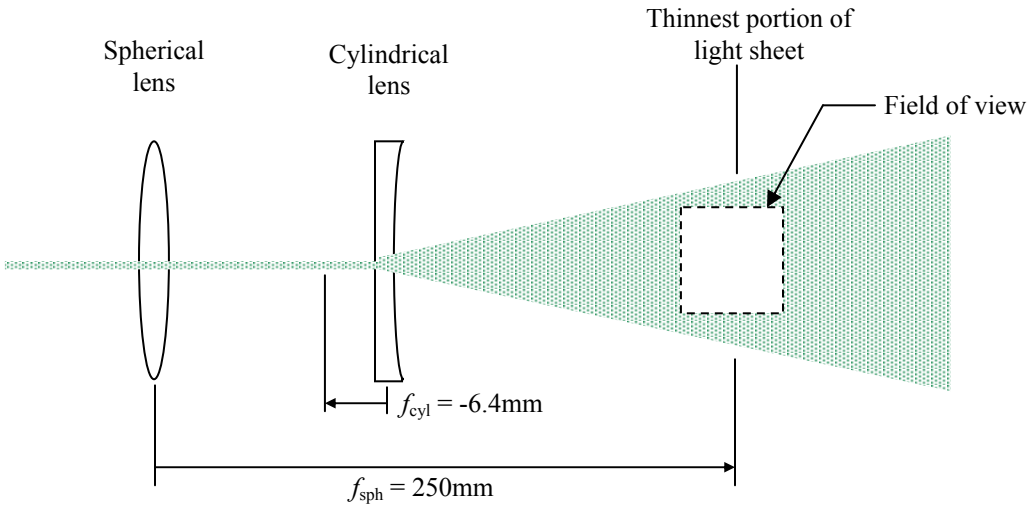

Figure 3.3: Side view of light sheet and optics (not to scale).

3.10 Camera and recording optics

The recording medium used in this experiment was a full-frame interline transfer CCD in a Kodak Megaplus model ES1.0 digital camera with a Nikon AFMicro Nikkor 60 mm lens. As noted earlier, a filter was placed before the lens to eliminate reflected laser light which would otherwise overexpose the frame. Unfortunately, this filter tends to attenuate the intensity of the light passing through it, thus the aperture was opened to the maximum setting of $f^{\#}$ 2.8 to allow the maximum possible light energy to reach the CCD array.

The digital camera used has a poorer resolution than its film counterpart, but gains at least two distinct advantages. First, with the interline image transfer, this CCD is able to take two images on separate frames thus eliminating the directional ambiguity and the rotating mirrors associated with film cameras and image shifting techniques. This feature also allows a whole series of images to be taken of a dynamic event. The second advantage is that being a digital device the images can be sent directly to the computer for analysis without first having to develop the film and digitise the images.

The Kodak camera employed has a CCD chip with an array of 1008 by 1018 pixels in the horizontal and vertical directions, respectively. With the interline image transfer, the camera was capable of acquiring two images as close as 1 μs. The camera capture rate was synchronized to the laser firing rate by the Berkeley Nucleonics 500B pulse generator. Images were sent to a Pentium III computer via a Matrox Meteor II/DIG frame grabber card. The software controlling the entire process was written at the University of Saskatchewan.

3.11 PIV Image Analysis

In dual-frame PIV, during analysis each image is subdivided into an array of interrogation areas. Displacements of the particles within corresponding interrogation areas (IA's) are found essentially by superimposing the two images and shifting one until the particle images overlap. A schematic representation of two images is given in Figure 3.4.

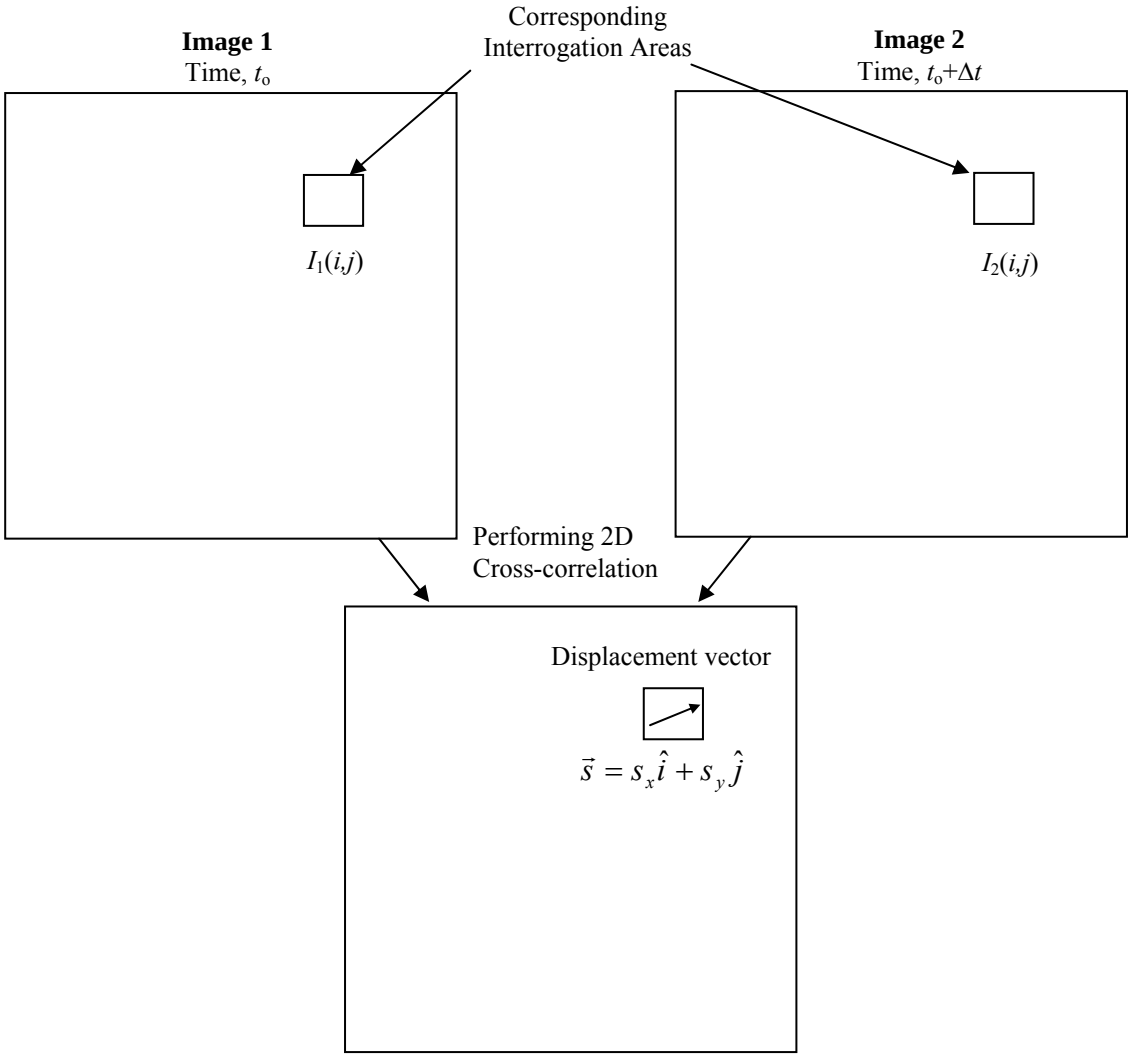

Figure 3.4: Two frames characteristic of dual-frame PIV. $I_1(i,j)$ and $I_2(i,j)$ are the image intensity functions of each respective interrogation area

Following Raffel *et al.* [1998], the components of the displacement vector can be found by using a discrete cross-correlation function,

$$R_{12}(x,y) = \sum_{i=-m}^{m}\sum_{j=-n}^{n} I_1(i,j)\cdot I_2(i+x, j+y). \tag{3.4}$$

The functions $I_1(i,j)$ and $I_2(i,j)$ are the image intensity values at location (i,j). An unexposed pixel will be black and have an intensity of zero. An image intensity of greater than zero represents an illuminated pixel which gives the position of a seed particle in the flow.

Essentially, a portion of image 1 is linearly shifted within a larger image 2 without extending over 2's borders. This is shown in Figure 3.5.

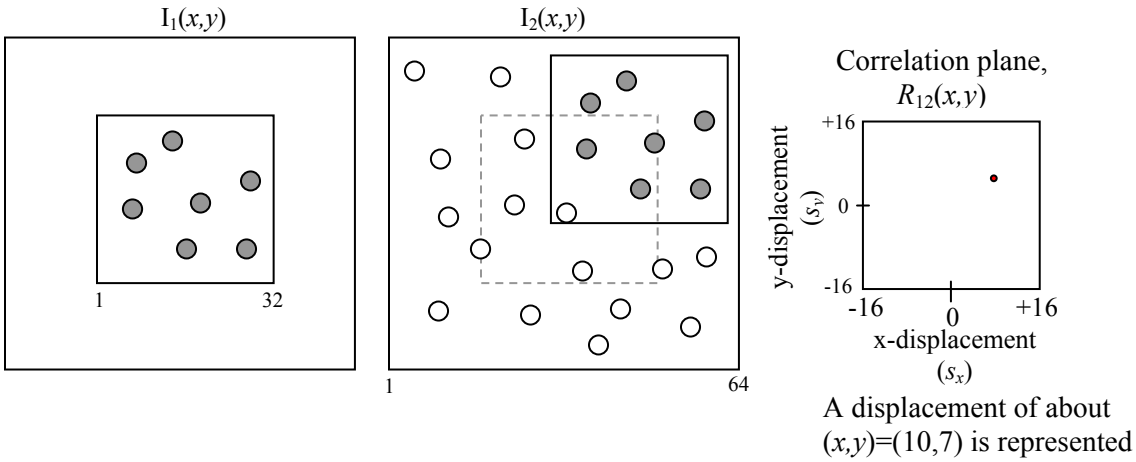

Figure 3.5: Shifting of interrogation area produces a peak on the correlation plane.

For each sample shift (s_x, s_y), the non-zero (overlapping) pixel intensities contribute greatly in the sum in equation (3.4) producing a single value of the cross-correlation function $R_{12}(x,y)$ for that shifted location. This process is repeated for a range of shifts, $-p \le s_x \le p$ and $-q \le s_y \le q$, giving a correlation plane with dimensions $(2p+1)$ x $(2q+1)$. There will occur a shift where many (ideally all) of the particle images from I_1 coincide with images in I_2 giving a large value of the cross-correlation function. By fitting a Gaussian curve to the correlation plane near the peak, the peak can be found with sub-pixel accuracy. This peak in the correlation plane gives the displacement vector for the entire interrogation area. The displacement is divided by the time between the laser pulses to give a velocity vector for that interrogation area. This procedure is repeated for all interrogation areas in the entire image.

Since this displacement vector represents that of the entire interrogation area, all particles within the IA are assumed to be moving homogeneously in that direction. No rotation or divergence is measured within a single IA, thus small interrogation areas are desirable to resolve velocity gradients. Also, since the positions are recorded at only two points in time, accelerations cannot be measured. PIV delivers an instantaneous velocity field at discrete points over the entire field of view.

The number of multiplications and summations demanded of equation (3.4) to produce even one correlation plane is quite staggering. Considering that over the entire field of view there may be several thousand correlation planes representing several thousand velocities, it becomes apparent that a computer will very quickly become overwhelmed for even moderately sized images divided into a moderate number of interrogation areas.

A much faster and less computationally intense method of calculating the cross-correlation function is to transform the two-dimensional image intensity functions $I_1(x,y)$ and $I_2(x,y)$ into the frequency domain. The cross-correlation of two functions is equivalent to a complex conjugate multiplication of their Fourier Transforms, given by,

$$R_{12} = FFT^{-1}\left(\hat{I}_1 \cdot \hat{I}_2^*\right). \tag{3.5}$$

Working with this method, two corresponding interrogation areas of equal size, $n_x n$ are removed from each frame and their two-dimensional Fast Fourier Transforms (FFT's) are computed. This is followed by a complex-conjugate multiplication of the resulting Fourier coefficients. Finally, an inverse Fourier transform yields the spatial form of the cross-correlation plane, which also has dimensions of $n_x n$. The number of operations required for the direct computation of the correlation plane is on the order of n^4, while shifting to the frequency domain reduces this to the order $n^2 \log_2 n$.

The PIV system used in this work followed the cross-correlation technique described, but also included some modifications that allow a more sophisticated measurement of velocity. Specifically, the size of the interrogation areas and their searching region were altered dynamically, and an outlier rejection algorithm was employed. The PIV analysis software, which was written in-house, allows the user to specify how many refinements to the grid to perform. In this work, a three-pass system was employed which began with interrogation areas that were 64x64 pixels. The first pass gives a course-grid displacement field of the entire field of view, and then for the second pass, the interrogation areas were reduced to 32x32 pixels. In the third pass, the interrogation areas were further reduced in size to 16x16 pixels.

Rather than simply running the cross-correlation algorithm on the finer grid, where interrogation areas from the same location are compared between the images, the displacement information from the first, coarse-grid, pass is used to shift the interrogation

area from the first image to a region on the second image where there is likely to be a higher correlation. Using this technique allows the resolution of high velocities even with small interrogation areas. In conventional, single-pass systems the dynamic velocity range is restricted since matching particle patterns must exist within the boundaries of interrogation areas at the same location in each of the two images. Using a single-pass system, the interrogation areas must remain large to ensure that particle images do not exit the IA between laser pulses, or the time between pulses must be reduced. However, reducing the time between laser pulses makes small displacements difficult to measure accurately. Larger interrogation areas are undesirable since we would like a very high spatial resolution to show details of the flow.

In the current work, the spatial resolution was increased by overlapping the interrogation areas by fifty percent. By doing this, the velocity vectors are spaced only 8 pixels apart in the final velocity field. This corresponds to a physical spacing between velocity measurements of 0.230 mm in the 100%wt glycerol case, and 0.227 mm in the 80%wt fluid. The difference is due to slight changes in the positioning of the tank and the camera between the tests.

3.12 Outlier Rejection Scheme

Because cross-correlation PIV relies on a statistical pattern matching approach, erroneous velocity measurements are possible due to such things as reflected light, regions where seeding density is low, and solid boundaries where there are no seed particle images. To minimize the number of erroneous measurements, or outliers, the PIV analysis software can incorporate an outlier rejection strategy. The current study included two separate outlier rejection schemes.

The first strategy was employed during the image analysis process. Each vector in the field was examined and if its magnitude was more than twice the mean of its eight neighbours, it was judged to be an outlier. Near the sphere, less than eight vectors may be available for this procedure. The correlation plane for this vector was re-examined, but the region that is examined for correlation peaks is restricted to an area corresponding to the mean velocity of the eight neighbours +/- a prescribed number of pixels in any direction. The spurious vector is then replaced by the velocity corresponding to the

highest correlation peak found in this new smaller region of the correlation plane. In this work, a window of +/- four pixels in any direction was chosen. This is shown in Figure 3.6.

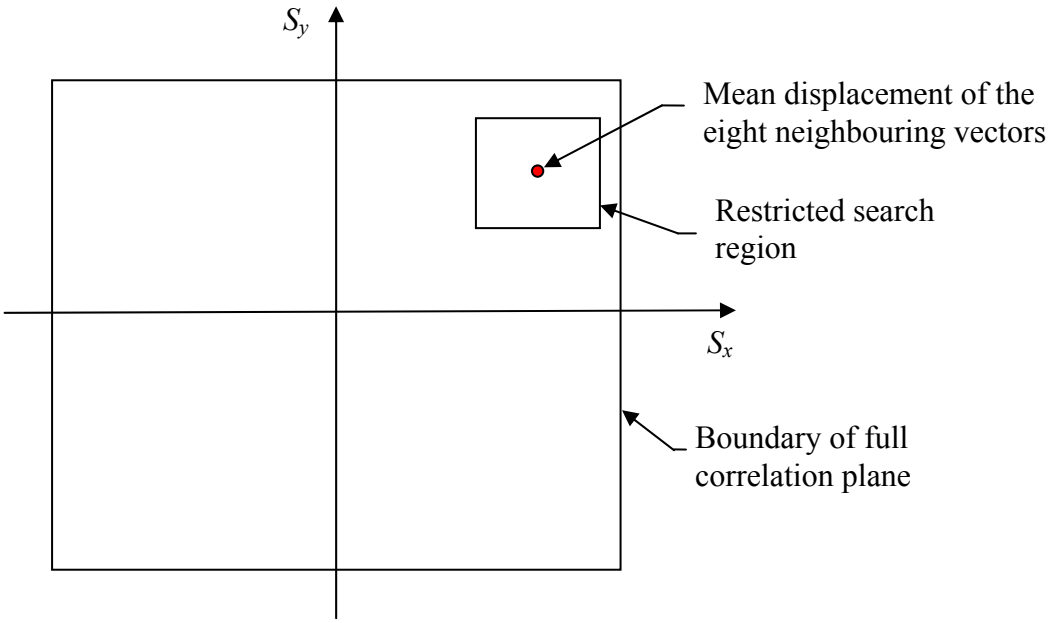

Figure 3.6: Search region on correlation plane is restricted to a small area around the mean of the neighbours when a vector is deemed an outlier.

The second strategy was employed as a post image-processing step. In this case, the correlation plane is unavailable for refined searching, so the vector field itself is used for corrective action. Each vector in the velocity field is tested to see if either of its two components is more than two pixels from the median of the measurement and its eight neighbours. If a vector is judged to be outside of this bound, then it is replaced by a Gaussian-weighted mean of the neighbouring measurements. In this case, two neighbours on either side of the spurious vector were used in the filter. This means that the bad vector is replaced with a Gaussian-weighted average of 24 neighbouring measurements. The neighbours are also tested and bad vectors are not included in the averaging. The Gaussian weighting function takes the form,

$$w = e^{-\left(r/b\right)^2}, \tag{3.6}$$

where r is the distance to the neighbour, and b is the filter width which is 8 pixels in this case. The new components, u_{new} and v_{new}, of the bad vector are then calculated by,

$$u_{\text{new}} = \frac{\sum_{\text{nb}} uw}{\sum_{\text{nb}} w}, \quad \text{and} \quad v_{\text{new}} = \frac{\sum_{\text{nb}} vw}{\sum_{\text{nb}} w}, \tag{3.7}$$

where nb represents the neighbouring vectors.

Chapter 4:
Results and Discussion

The results and discussion will be subdivided into several sections. First, the velocity history of the sphere will be shown, which relates to the equation of motion presented in Section 2.5.5. Then, the velocity fields obtained by the PIV technique will be presented. Due to the large number of velocity fields obtained during these experiments, only a few will be shown in the body of this thesis and the remainder will be given in Appendix A. Several features of the flow fields will be extracted from the two-dimensional velocity fields. These include the profile of the vertical component of velocity between the wall and the equator of the sphere, the shear stress at the equator of the sphere, the shear stress distribution along the wall, and the location of the centre of the vortex structure which develops between the sphere and the wall.

4.1 Velocity History

In this thesis, the term "velocity history" refers to the entire transient as the sphere accelerates from rest until it reaches terminal velocity. The instantaneous sphere velocity will be used to normalise the PIV velocity fields at each instant during the transient. As well, the equation of motion presented in Section 2.5.5 will be compared to the experimental velocity history.

The velocity history can be plotted as a function of time or sphere position. The PIV system has the ability to measure the position of objects with great accuracy, but there is less control over the time between the release of the sphere and when it appears in the frame. For this reason, an optical circuit using a trigger laser was employed. The PIV images were taken the instant that the sphere broke the beam of the trigger laser, thus giving direct control over the distance the sphere has traveled from release. In this way, the images obtained with the PIV apparatus were used to determine the velocity of the sphere at known distances from the release point rather than at known times.

PIV software is designed to measure the motion of the tiny seed particle images and not the position of large objects in the field of view. Therefore, a separate pattern recognition technique was used to measure the sphere velocity.

Consider a typical PIV frame as shown in Figure 4.1. The frame is populated by a large number of individual "dots" that mark the positions of the seed particles during the firing of the laser. This picture shows dark seed particles on a white background, but the colours have been reversed to facilitate printing. In reality, the background is black and the seed particles appear as bright points. In Figure 4.1, the location of the sphere can be observed as the semicircular region that is devoid of seed particle images. The laser light sheet is coming from the left of the picture. As a result, the sphere casts a shadow that can be seen to the right of the sphere.

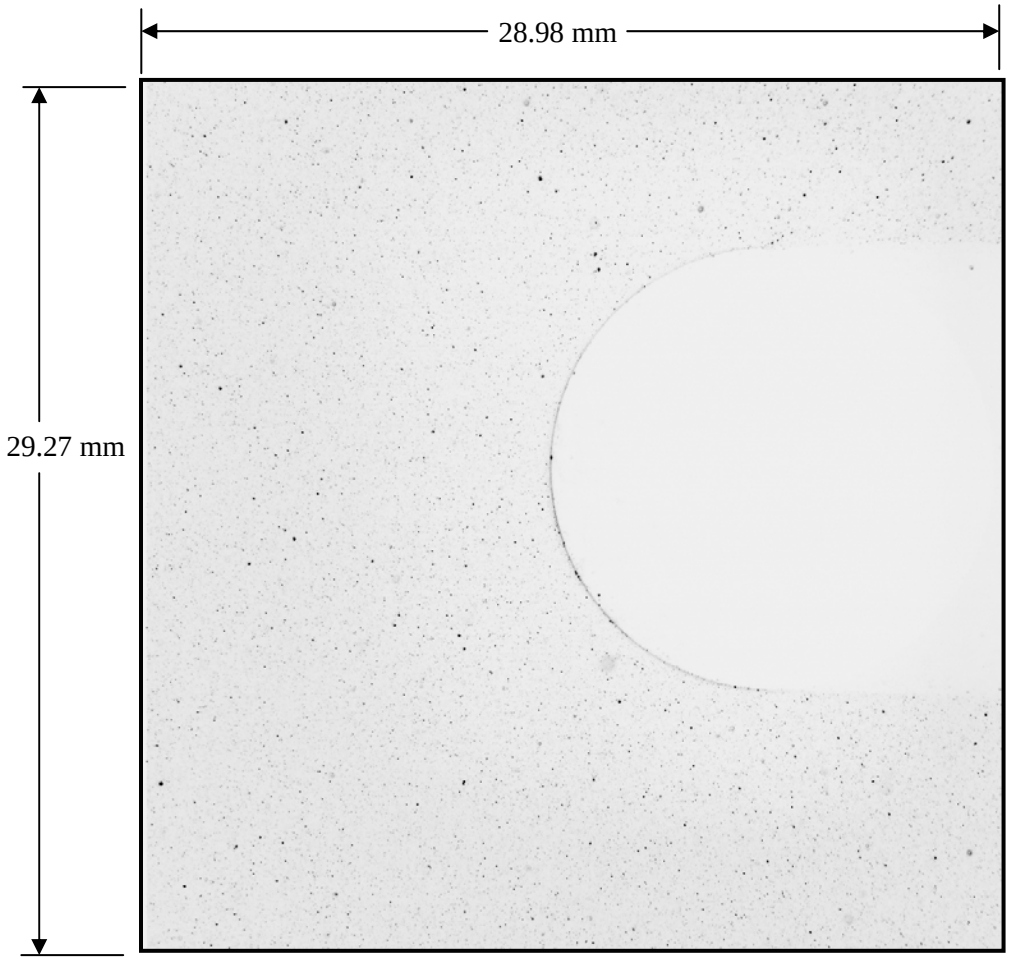

Figure 4.1: A typical PIV image. For clarity, the greyscale has been inverted and the small dots are tracer particles. The light approaches from left to right and the region devoid of tracer particles on the right side of the image is the sphere and its shadow.

To find the velocity of the sphere, the pattern matching technique in a software package called Matrox Inspector® was used. A picture of the black sphere was taken against a white background and used as a "model" that Inspector® used for pattern recognition. The model image was compared against the PIV images and translated within the frame until the highest correlation was obtained. The black pixels of the sphere in the model image matched up with the black background and had the highest correlation where there were no bright seed particle images. Conversely, the bright seed particle images matched up with the white background on the model image. This is similar to a cross-correlation PIV system, except that the entire frame is the interrogation area. It was found that Inspector was very effective at locating the sphere in each of the PIV frames.

The two images obtained for each laser pulse pair were used to obtain the sphere velocity. The distance that the sphere traveled between the images was found using the pattern-matching technique. This distance was divided by the time between the pulses to obtain the velocity. Note that since the time separation between the laser pulses was very small, there was high uncertainty in the sphere velocity obtained using this method. Uncertainty in the sphere positions has a large effect on the calculated velocity.

To reduce this uncertainty, many sphere drops were conducted at each desired location along the transient, and the velocities obtained from each were averaged. By positioning the sphere release mechanism with respect to the trigger beam, the PIV system could be triggered at any desired location along the transient with high repeatability. The coordinate, Y, is the distance the sphere travels from the release point. Drop heights of Y = 1, 2, 3, 4, 5, 6, 8, 10, 14, 18, 20, 40, and 60 mm were used. Ten separate sphere drops were conducted at the Y = 2, 5, 10, 20, and 60 mm heights. These are the locations in the transient where PIV measurements were made around the sphere. At the other locations, the sphere velocity alone was determined from an average of three drops. The time separations between the laser pulses in each case are summarised in Table 4.1.

Table 4.1:
Laser pulse separation times for PIV and sphere velocity measurement locations

Distance from release, *Y* [mm]	Number of measurements at each location	% Glycerol	Time between laser pulses [μs]
2, 5, 10, 20, 60	10	100	15000
		80	2000
1, 3, 4, 6, 8, 14, 18, 40	3	100	30000
		80	15000

The velocity history for the 80% glycerol case with a wall spacing of h/d = 6.0 is shown in Figure 4.2. Each data point represents the velocity obtained for an individual drop.

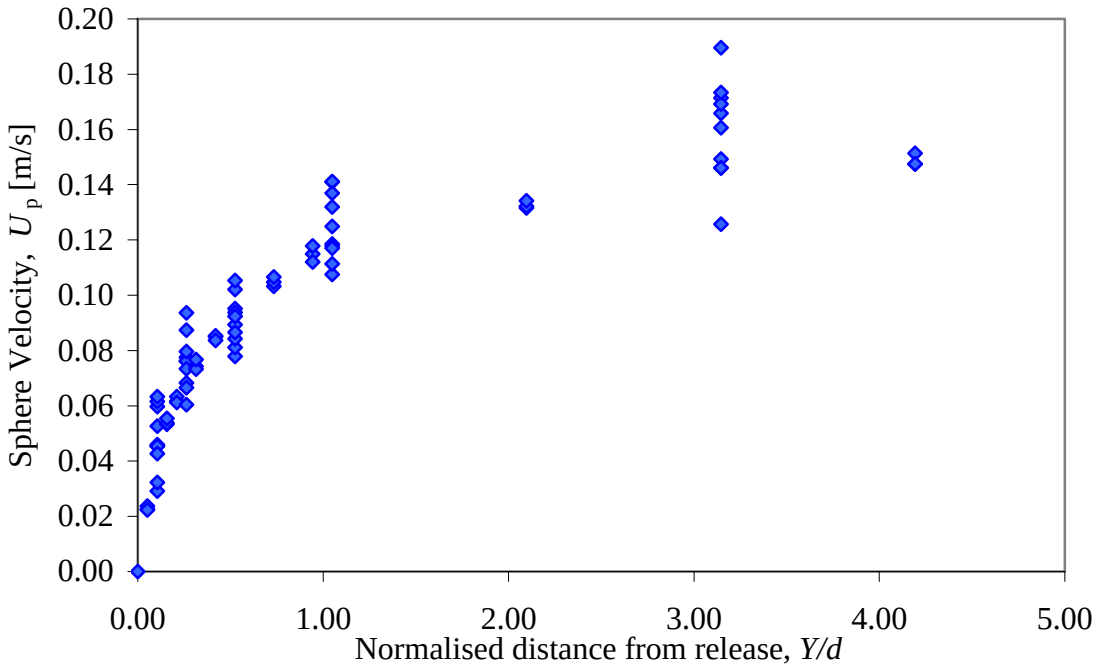

Figure 4.2: Velocity history for 80%wt glycerol with a wall spacing of h/d = 6.0. The terminal Reynolds number is Re_T = 72.

The time separation between the laser pulses has a clear effect on the data. Longer time separations allow the velocity of the sphere to be determined with greater accuracy. In Figure 4.2, for example, the small time separation of 2000 μs is used for PIV measurements at the Y/d = 3.2 location. The sphere velocities measured at this point in the transient show much greater variability than those at Y/d = 2.2 where the time separation was 15000 μs. However, a long time separation is undesirable for PIV analysis since it decreases the spatial resolution of the velocity field. Thus, a shorter time separation was chosen for the frames where PIV analysis was done. The increased variability of the measurement of sphere velocity at these locations is due to the decreased time separation, Δt, between the two images. This increases the error in velocity due to uncertainty in locating the sphere in the image. An error of one pixel in locating the sphere image when Δt is 2000 μs will lead to an error of 0.014 m/s, or 7% of terminal velocity in this case. For the 100% glycerol case, the PIV location sphere velocities have an error of 9.5% of terminal velocity.

The experimental sphere velocity data were fit to a function of the form,

$$U_p(Y) = \frac{U_T}{1 + \frac{a}{Y^b}}, \tag{4.1}$$

where U_T is the terminal velocity of the sphere, Y is the distance the sphere has fallen from the point of release, and a and b are curve fitting parameters. Given the experimental data in terms of instantaneous sphere velocity, U_p, and the distance the sphere has fallen, Y, the parameters U_T, a, and b were determined from a Levenberg-Marquardt non-linear curve fitting routine using Microcal Origin®. The results of the curve fitting for the 80% glycerol, h/d = 6.0 case are given in Figure 4.3.

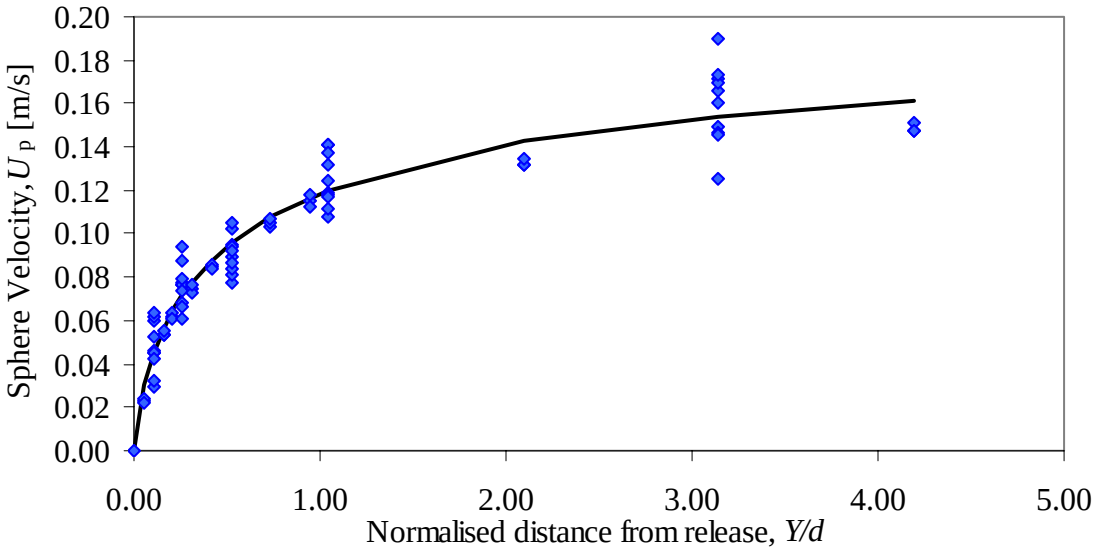

Figure 4.3: Velocity history for 80%wt glycerol with a wall spacing of h/d = 6.0, shown with curve fit line. The terminal Reynolds number is Re_T = 72.

The form of the curve fitting given in equation (4.1) gives very good agreement to the measured velocities. The parameters of the non-linear curve fitting for each case are given in Table 4.2.

Table 4.2:
Curve fitting parameters for equation 61 describing velocity histories

	80%wt Glycerol			**100%wt Glycerol**		
	h/d			***h/d***		
	6.0	1.5	1.2	6.0	1.5	1.2
U_T [m/s]	0.202	0.193	0.163	0.020	0.0103	0.00876
***a* [m]**	5.708	4.269	5.856	0.746	0.391	0.173
B	0.710	0.572	0.778	0.677	1.071	0.253

Since the fitted curves accurately reflect the trend of the measured sphere velocities, for the sake of clarity, the fitted curves alone will be used to compare the cases where the wall proximity is decreased. Figure 4.4 shows the results for the 80% glycerol case and Figure 4.5 shows the 100% glycerol case. In each figure, the velocity histories are normalised with respect to the terminal velocity of the sphere measured in the *h/d* = 6.0 case.

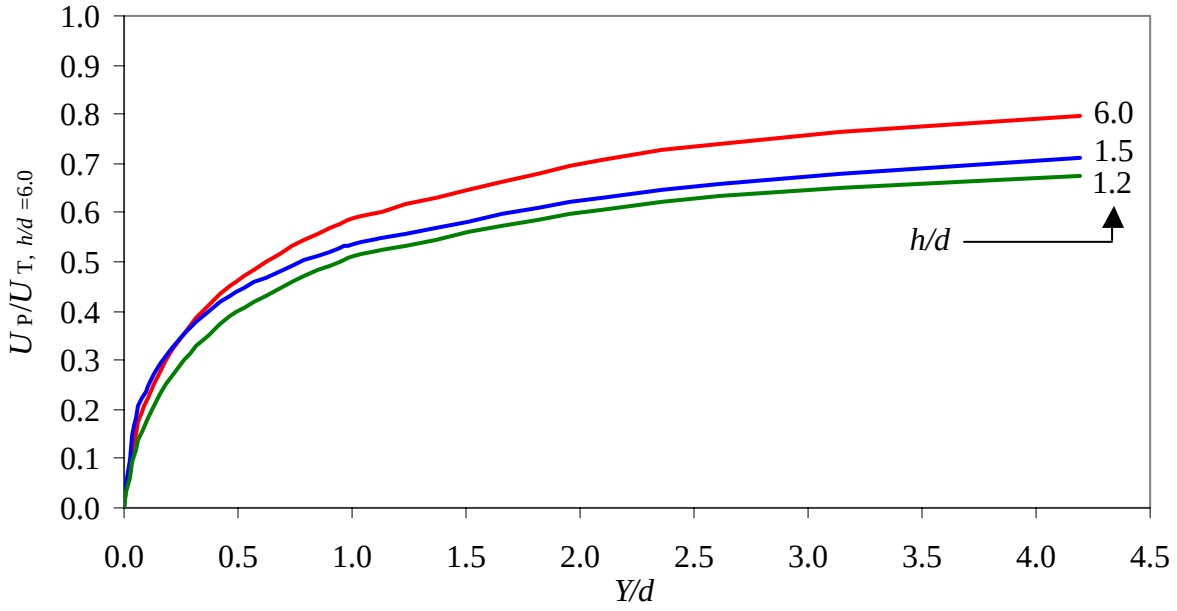

Figure 4.4: Curve fits of the velocity history for the 80%wt glycerol cases. The velocities are normalized with respect to the terminal velocity of the sphere in the h/d = 6.0 case.

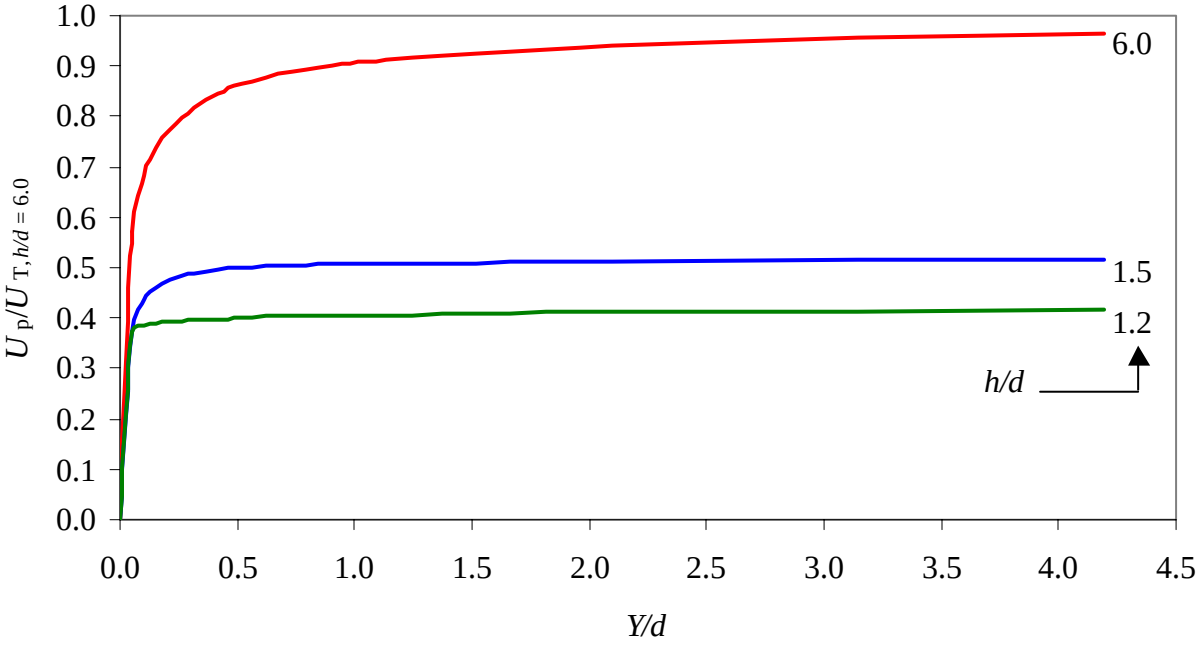

Figure 4.5: Curve fits of the velocity history for the 100%wt glycerol cases. The velocities are normalized with respect to the terminal velocity of the sphere in the h/d = 6.0 case.

As demonstrated in Figures 4.4 and 4.5, the effect of the walls is clearly to retard the motion of the sphere at terminal velocity. This is shown in the decrease in the terminal velocity as the gap narrows, which indicates that the steady drag force is being modified by the presence of the walls. The flow around the sphere is unconstrained when the walls are far away from the sphere. In this case the flow is axisymmetric and represents the infinite fluid case. However, when the solid boundaries move closer, the avenues of fluid motion are "squeezed" in the wall-normal direction and the flow around the sphere is no longer axisymmetric. This tends to increase the velocity gradients in the fluid between the surface of the sphere and the solid wall, thus increasing shear stress in the fluid. As well, the pressure distribution around the sphere is likely to be altered and the form drag changed as a result. With narrow wall spacing more fluid flows around the sphere in the wall-parallel direction, which requires the fluid to follow a longer route.

Figure 4.3 demonstrates that the curve fit of equation (4.1) follows the experimental data very well. This is very encouraging since these curve fits represent specific solutions to the equation of motion given in equation (2.44) of Section 2.5.5. However, rather than investigating the relationship between the curve fitting parameters and the physical properties of the fluid and the sphere, the equation of motion will be solved numerically. If the parameters of the curve fit could be related to such properties as the density ratio between the sphere and fluid, the fluid viscosity and especially to the ratio of wall spacing to sphere diameter, the curve fits would represent good empirical formulations of solutions to the equation of motion. This would be a great advance, as the equation of motion given in equation (2.44) is rather difficult to solve. The current study includes a numerical solution which is presented in the following section.

4.2 Numerical Solution of the Equation of Motion

According to Chang *et al.* [1998], equation (2.44) is a nonlinear Volterra type singular integro-differential equation. Due to the implicit form of the steady drag term, where the instantaneous sphere velocity appears, an analytical solution is not possible. In this thesis, a fourth-order Runge-Kutta numerical method was used to solve the equation of motion. Specific attention had to be paid to the integration involved in calculating the history force. The history force represents the past "memory" of the flow for the entire duration of acceleration. Thus, the integral is evaluated by summing all of the sphere accelerations in each time interval from zero to the current time. Therefore, all sphere accelerations must be stored for each time interval as the solution progresses. As noted earlier, the integral approaches a singularity as the time variable is equal to the dummy variable of integration. For each time step in the integral, the sum is calculated using the trapezoidal rule, however, at the last time step, to avoid the singularity, a rectangle the height of the second-last step is used. Admittedly, this introduces some error in the integration that tends to underestimate the magnitude of the history force. This error will be most pronounced at the earliest stages of the transient where the slope of the distance versus time graph is quite large. The magnitude of this error will decrease as the sphere approaches terminal velocity. Choosing an integration time step that is small may minimize the error, but this increases computation time and storage requirements.

Chang [1998] presents the results of several numerical studies along with experimental data given by Moorman [1955] in his Ph.D. thesis for solid spheres accelerating due to gravity. Moorman used photographs to track the trajectory of solid spheres falling in a tank filled with oil or a glycerin-water mixture. His results were given in terms of terminal Reynolds number Re_T and the density ratio (ρ_p/ρ_f) between the particle and the fluid. The results of the current numerical study, those of Mei and Adrian [1992], and the experimental results of Moorman [1955] are given in Figure 4.6. Moorman presented results where the terminal Reynolds number was 254 and the density ratio was 2.57. This is the case presented in Chang's paper which most closely resembles the parameters of the current study.

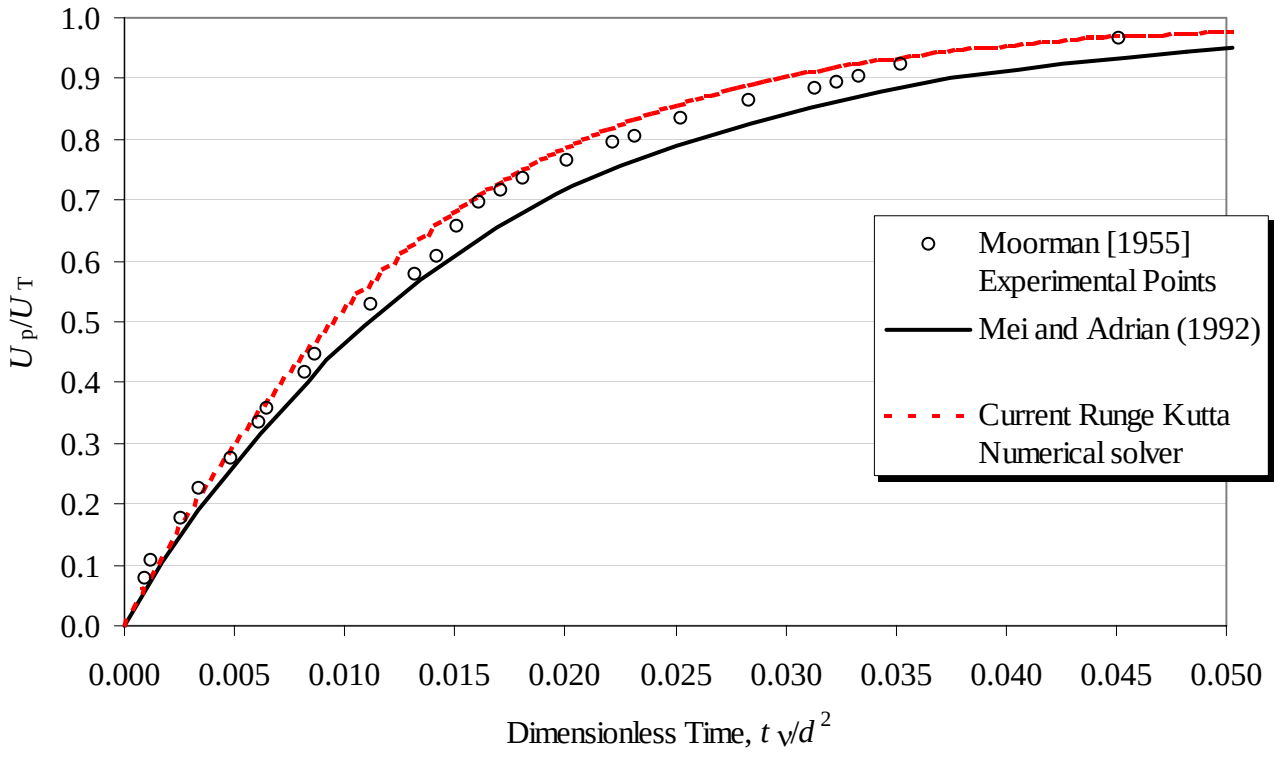

Figure 4.6: Numerical solutions to the equation of motion along with experimental results for $Re_T = 254$, $\rho_p/\rho_f = 2.57$, Chang [1998].

The results from the current experiments could not be compared directly with Moorman's experimental data since the density ratios were not the same, and the terminal Reynolds numbers do not match. A computer code was developed in the FORTRAN language that allowed the properties to be changed to give the correct density ratio and terminal Reynolds number. It appears that the computer code gives a solution that follows the experimental data of Moorman very closely within this range of Reynolds numbers. It is interesting to note that although the same equation of motion is being solved, Mei and Adrian [1992] give a result that is slightly different. This is likely due to the different forms of the drag coefficient that Mei and Adrian used rather than the Schiller-Neumann formula used in this thesis. Also, Mei and Adrian used a multi-step, fourth-order Adams-Bashforth-Moulton predictor-corrector method, whereas the current study used a fourth order Runge-Kutta Cash-Karpe method. As well, Mei and Adrian avoided the singularities at the end of the history integration by employing a 16-point

Gaussian-Legendre quadrature for the point where $t=s$, rather than using an estimated rectangle in lieu of the trapezoidal rule. The methods employed by Mei and Adrian would tend to give more accurate results, but from inspection of the experimental data in Figure 4.6, the Runge-Kutta technique appears to be very effective within the range of parameters given. Thus, this method was used with confidence throughout the current study.

With this in mind, the Runge-Kutta solver was applied to the current experiments. The properties of the sphere and fluid were measured and their related measurement uncertainties noted. The properties used are given in Tables 4.3 and 4.4 for the sphere and fluids respectively. The Ohaus Adventurer 210-g-maximum-capacity balance used for measuring the mass of the sphere was accurate to 0.0001 g, thus the uncertainty in the third decimal place was assumed to be negligible. The diameter of the sphere was measured at 20 locations using a Vernier caliper, and confirmed using 20 measurements using a micrometer. The standard deviation of the sphere diameter measurements was 0.007 mm, leading to a 95% confidence level of ± 0.01 mm.

Table 4.3
Sphere properties with uncertainty limits

Variable	Nominal Measurement	Uncertainty
Diameter, d [mm]	19.07	±0.01 from micrometer
Mass, m_p [g]	5.056	±0.0001 from electronic balance

The viscosity of the fluid was measured in the tank during the experiment with a Brookfield rotating spindle viscometer. The viscosity was measured continuously throughout each experiment, resulting in a recorded minimum, maximum and average viscosity of the fluid for each wall spacing. The density of the fluids was measured using a calibrated volume flask and the Ohaus Adventurer balance. The uncertainty in the volume of the flask was given by the manufacturer as ±0.08 mL.

Table 4.4
Fluid properties with uncertainty limits

	Variable	Nominal measurement	Uncertainty
80%wt Glycerol	Density, ρ_f [kg/m^3]	1206.26	±0.964 from flask
	Viscosity, μ_f [Pa.s]	0.0557	±0.0019 from measurement variability
100%wt Glycerol	Density, ρ_f [kg/m^3]	1255.39	±1.00 from flask
	Viscosity, μ_f [Pa.s]	1.000	±0.01 from measurement variability

Since the equation of motion is valid only for spheres descending in an unbounded fluid, the results given in Figures 4.7 and 4.8 are for the case where the wall spacing is at its maximum of $h/d = 6.0$. The results of the numerical solutions are shown with a solid line representing the nominal values of each variable and the uncertainty boundaries based on the uncertainties in the measurements are shown as thinner lines on either side.

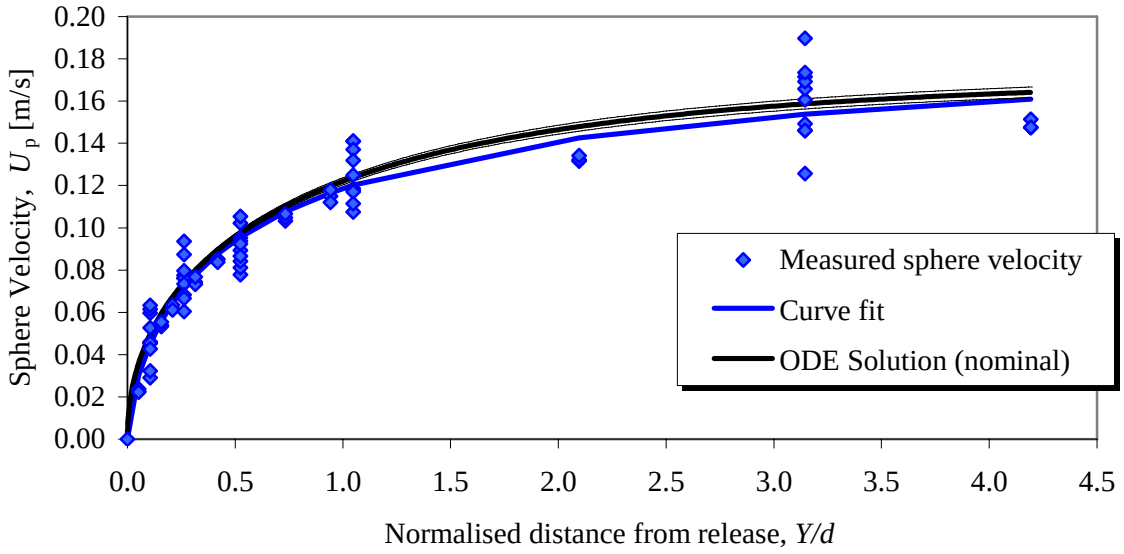

Figure 4.7: Velocity history for 80% glycerol with a wall spacing of h/d=6.0. The graph shows the individual velocity measurements, the fitted curve, and the numerical solution of the equation of motion along with the uncertainty bounds.

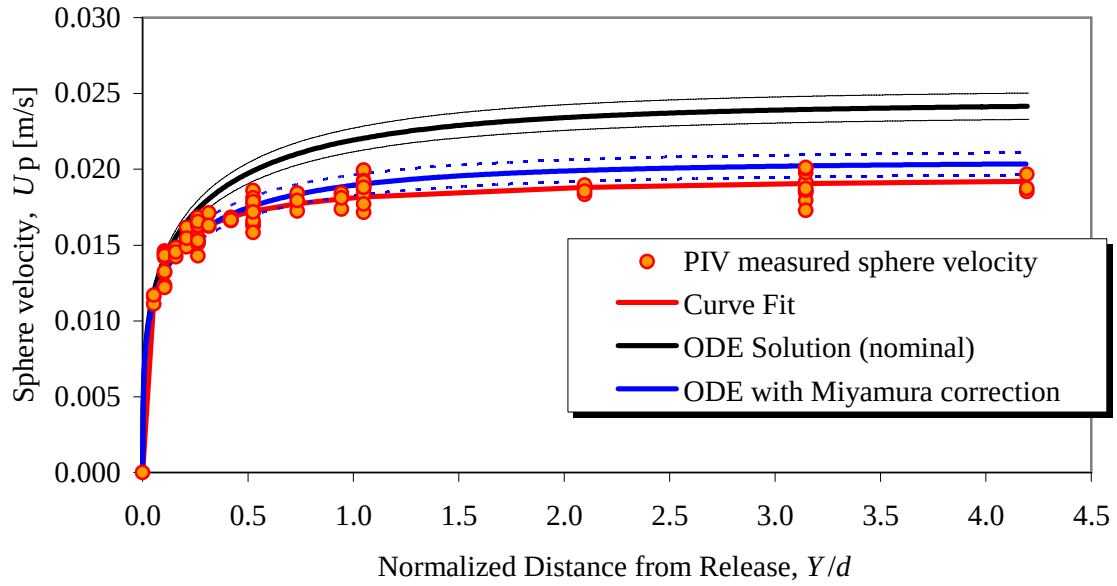

Figure 4.8: Velocity history for 100% glycerol with a wall spacing of h/d=6.0. The graph shows the individual velocity measurements, the fitted curve, and the numerical solution of the equation of motion along with the uncertainty bounds. The blue curve shows the solution with Miyamura *et al.*'s [1980] correction applied to the steady drag term.

For the 80% glycerol case, the numerical solution of the differential equation of motion appears to be able to predict the velocity history of the sphere very well. The numerical solution and the measured data almost coincide over the range of Y/d in Figure 4.7. However, the agreement is lost later in the transient as the numerical solution predicts a terminal velocity of 0.1714 m/s, while the curve fit terminates at 0.2018 m/s. This is likely a result of the lack of data at terminal velocity in this case, which affects the curve fitting. In the 100% glycerol case shown in Figure 4.8, the agreement is lost much earlier in the transient, and the predicted terminal velocity of 0.0245 m/s is much higher than the observed terminal velocity of 0.01995 m/s. As shown in Figure 2.5, Miyamura *et al*. [1980] suggest that for low Reynolds number flows, the walls will have an effect even for a wall spacing of h/d = 6.0, or $r^* = 0.167$ in their notation. Miyamura *et al*. predict that the walls at this spacing will reduce the unbounded terminal velocity by a factor of approximately 1.19, giving a terminal velocity of 0.0206 m/s. While this is only 3% higher than the observed terminal velocity of 0.01995 m/s for the 100%wt glycerol, h/d = 6.0 case, the prediction lies outside of the uncertainty boundaries due to the measurements of the properties of the fluids and the sphere.

Although the properties of the sphere and the fluids were measured with great care, the discrepancy between the numerical solution and the observed velocities is significant. The explanation may lie in confounding effects that were not accounted for. For example, the sphere was weighted by drilling a hole through the centre and filling it with lead. This resulted in surface irregularities at the “poles” where the lead slug emerged from the sphere. The equation of motion was found to be very sensitive to changes in diameter. An uncertainty of 1% in the diameter results in a 28% change in the predicted terminal velocity. This is quite startling. However, the measurement uncertainty in the diameter was a maximum of 0.07% of diameter, which leads to only 2% uncertainty in the terminal velocity. Perhaps the surface irregularities on the sphere, or the slight roughness associated with the black paint tended to alter the sphere velocities measured in the lab. These effects were not included in the equation of motion.

As well, the properties of the fluid may not have been consistent throughout the tank. Glycerol is soluble in water, and is hygroscopic which means it tends to absorb

moisture from the air. By observing objects extending into the fluid, it was noticed that the index of refraction of the fluid changed near the free surface of the glycerol mixture. This effect extended only a few centimeters into the fluid, and was assumed to be due to the glycerol absorbing water vapour from the air. Additional water content would tend to lower the viscosity of the mixture. Any objects, such as the sphere, which entered the tank would pass through this layer and pick up a film of lower viscosity fluid. Also, the viscosity measurements were made in the upper portion of the tank. It is possible that the layer of lower viscosity fluid at the surface affected the viscosity measurements. This effect would be most pronounced in the 100% glycerol case, as the viscosity of glycerol-water solutions drops sharply between 100% glycerol and 95% glycerol. Between 100% and 99% glycerol, the viscosity drops by approximately 18%. However, the equation of motion is not that sensitive to uncertainty in fluid viscosity. A 1% change in viscosity leads to only 0.9% change in terminal velocity. The measurement uncertainty of the viscosity during the 100% glycerol experiments was actually much higher, at approximately 10% of the nominal reading. This degree of uncertainty leads to a 9.3% change in the terminal velocity. However, it must be remembered that these measurements were made near the top of the tank, whereas the sphere drops were made near the mid-depth where the fluid concentration could have been slightly different, and slight differences in concentration have a large effect on viscosity near 100% glycerol. If indeed the effect was present during the experiment, it was not accounted for.

Finally, the sensitivity of the terminal velocity calculation to uncertainty in fluid density is such that a 1% change in fluid density leads to a 9% change in predicted terminal velocity. In the current study, the fluid density was measured with a carefully calibrated flask and a very sensitive scale. The uncertainty in this measurement was about 0.08% of the nominal value. This leads to a 0.7% uncertainty in the predicted terminal velocity.

With the observed measurement uncertainties of each variable taken into account, the overall uncertainty of the numerically predicted terminal velocities is about 9.5% in the 100% glycerol case, and about 2.3% in the 80% glycerol case. In neither case do the uncertainty bounds include the measured terminal velocity, so one or more of the other effects just discussed must be important. As discussed previously, Miyamura *et al*.

[1980] suggest that the walls have an effect even at a wall spacing of $h/d = 6.0$ in the 100%wt glycerol case, although the effect is not great enough to bring the terminal velocity within the uncertainty bound of the predicted terminal velocity.

4.3 Effect of Wall Proximity on Steady Drag Force

As was demonstrated in Figures 4.4 and 4.5, one of the effects of the wall proximity is to decrease the terminal velocity as the wall spacing decreases. This suggests that a factor based on the ratio of wall spacing to sphere diameter could be applied to the steady drag force term in the equation of motion. This modification would make the steady drag term increase as the wall spacing decreases. If the wall factor is defined as $f(h/d)$, then the steady drag force term of equation (2.44) becomes,

$$\vec{F}_{\mathrm{D}} = \frac{1}{f(h/d)}\frac{1}{2}\rho U_{\mathrm{p}}^{2} C_{\mathrm{D}} A, \tag{4.2}$$

where the drag coefficient is still given by the Schiller-Neumann formula in equation (2.31).

By defining the wall factor in this way, the function varies between zero when the walls touch the sphere, and one for an infinite fluid. In this study, the wall factor was determined by comparing the observed terminal velocities to the terminal velocity achieved in the h/d = 6.0 case. The resulting wall factors for the two different fluids and the three wall spacings are presented below in table 4.5.

Table 4.5
Calculated wall factor for Steady Drag

	80%wt Glycerol	**100%wt Glycerol**
h/d	***f(h/d)***	***f(h/d)***
6.0	1.000	1.000
1.5	0.958	0.517
1.2	0.808	0.439

The wall correction factor of Miyamura *et al*. [1980] given in equation (2.46) is for a sphere in steady, creeping flow between plane walls. This wall correction is compared to the results given above for the 100%wt glycerol case where the unconstrained terminal Reynolds number is 0.6. These results are compared in Table 4.6. In this table, U_{free} is calculated from the Schiller-Neumann relationship.

Table 4.6
Comparison between Miyamura *et al*. [1980] and PIV wall factors in terms of the effect on terminal velocity.

	PIV 100%wt	Miyamura [1980]
h/d	U_{free}/U_{wall}	U_{free}/U_{wall}
6.0	1.23	1.19
1.5	2.37	2.26
1.2	2.79	3.17

When comparing the wall correction factors for each wall spacing, we see that although the trend is the same in each case, with the wall constrained velocity U_{wall} decreasing with decreasing wall spacing, the magnitudes of the wall corrections are somewhat different. This may be due to the fact that Miyamura *et al.*'s wall correction is only strictly valid for zero Reynolds number. Miyamura *et al*. present their correction function as a 19^{th} order polynomial, the truncation errors on the higher order terms will have a great effect on the calculated results. For this reason, the results of Miyamura *et al*. presented in Table 4.6 are estimated from the graph shown in Figure 2.5 rather than calculated from the 19^{th} order polynomial given in equation (2.46).

4.4 Effect of Wall Proximity on the Unsteady Forces

Modifications to the steady drag force ensure that the equation of motion predicts the correct terminal velocity. The effect of the modification to the drag force is also present in the transient. However, the importance of the wall correction grows from zero as the sphere accelerates from rest since the quasi-steady drag force grows with increasing Reynolds number. The transient is dominated early on by the history and added mass forces. These forces have not yet been modified to account for the presence of the constraining walls.

Magnaudet [1995] and Legendre [1996] suggest that the added mass coefficient for a sphere in an unbounded flow is 0.5 regardless of the flow parameters. It is unclear if the added mass coefficient of 0.5 remains unaffected in the presence of constraining walls. However, the added mass coefficient may be unaffected by the walls since the

integrated effects of accelerating fluid around the sphere is the same regardless of changes to the path as the walls limit the flow in only one direction. This is not the same as the case of a sphere in a tube, or a circular cylinder between plane walls where the flow around the body is constrained in all directions. The added mass force for an accelerating sphere may be unaffected by the presence of plane walls, however a complete investigation of this phenomenon must be conducted before conclusions can be drawn.

The same cannot be said of the history force, as this force arises from the effects of diffusion of vorticity away from the surface of the sphere. In the infinite fluid case, the flow around the sphere is axisymmetric and the vorticity is free to diffuse into the fluid in any direction. However, when the walls are present, the diffusion of vorticity is blocked in the wall-normal direction. In the limiting case where the walls touch the sphere, the diffusion is completely precluded between the wall and the sphere. This effect would tend to cause the history kernel to decay more rapidly, decreasing the importance of the history force as the wall spacing decreases. This can be qualitatively observed in the 100%wt glycerol case in Figure 4.5, where the sphere reaches terminal velocity essentially within 10% of the sphere diameter for the narrowest wall spacing. Without a wall correction factor, the history force would tend to be overestimated which would tend to underpredict the sphere velocity during the transient.

Unfortunately, these presumed corrections to the transient forces cannot be verified by comparing the numerical solution to the experimentally measured velocity histories. This is due to the fact that the wall factor for the quasi-steady drag was derived by comparing the ratio of observed terminal velocity for the cases where the walls had an influence to the terminal velocity observed for the widest wall spacing. This is a purely empirical formulation, and since the terminal velocities in the infinite fluid cases were *not* matched by those predicted by the numerical solution, the wall correction factors given in Table 4.5 will not ensure the terminal velocity is asymptotically matched when the wall spacing has an effect. Thus the experimental data for the velocity history in the close-walled cases cannot be compared to the numerical solutions with the steady-drag force correction factor included.

4.5 The Velocity Field around the Accelerating Sphere

So far, the motion of the sphere as it accelerates through the fluid under the influence of gravity and the ways in which the forces acting on the sphere are separated have been discussed. The solution to the classical problem of a sphere moving at terminal velocity is very well established, however the transient forces acting on the sphere prior to the terminal phase are less well understood. The transient forces are separated into the added mass force and the history force, each of which is associated with a different aspect of the dynamics of the fluid that surrounds the moving sphere. With this in mind, a view of the velocity field in the fluid should shed some light on the nature of these transient forces. Comparing velocity fields early in the transient to those near the terminal velocity will show how the velocity field is established, and demonstrate how the transient forces change throughout the acceleration phase. As well, the velocity fields around the sphere can be compared for various wall proximities.

Due to the large number of velocity fields obtained during this experiment, only a few examples of the complete, two-dimensional velocity field will be presented here. A complete set is given in Appendix A. As well, since the spatial resolution is very high, the spacing between the individual velocity vectors is very small. Therefore a number of vectors have been omitted from each velocity field in order to focus attention on important aspects of the flow. A note will be presented with each figure to explain how much data are omitted.

As noted in Section 4.1, each velocity field is an ensemble average of ten separate velocity fields taken at the same location in the transient. Before the averaging, the data are filtered to remove spurious vectors, although in some instances a small number of these bad vectors may remain in the velocity field. In each case the velocity field will be presented in two frames of reference. The left half of the axis of symmetry shows the velocity field relative to the moving sphere. In the right half, the instantaneous sphere velocity has been subtracted from each vector, which changes the frame of reference to show the flow around a stationary sphere. Each velocity field includes a reference vector to establish a scale for the velocity vectors in that frame. In each case, the magnitude of the reference vector is the instantaneous sphere velocity. The coordinate axes in each

velocity field are attached to the centre of the sphere. In addition, the coordinate Y is the distance from the centre of the sphere at release to the centre of the sphere at its current position during the transient. In each velocity field, the distance the sphere has dropped is normalised with the sphere diameter and is given as Y/d, where d is the diameter of the sphere. The instantaneous sphere velocity, U_P, is normalised with the terminal velocity of the sphere, U_T, and is given as a percentage.

The velocity fields shown in this section will be taken from the 80%wt glycerol case. First, two different times during the transient will be compared for the widest wall spacing (h/d = 6.0). The sphere reaches a terminal Reynolds number of 72 in this case. At this Reynolds number, a symmetric, closed wake pattern is expected to form behind the sphere. Second, the effect of the walls will be demonstrated by showing velocity fields taken at the same drop height, Y/d, but for different wall spacings.

Begin by considering Figure 4.9 where the velocity field early in the transient is shown. In this case the sphere has dropped only 2 mm, about 10% of the sphere diameter, and has reached 23.7% of the terminal velocity. In these figures, every eighth row of vectors is shown.

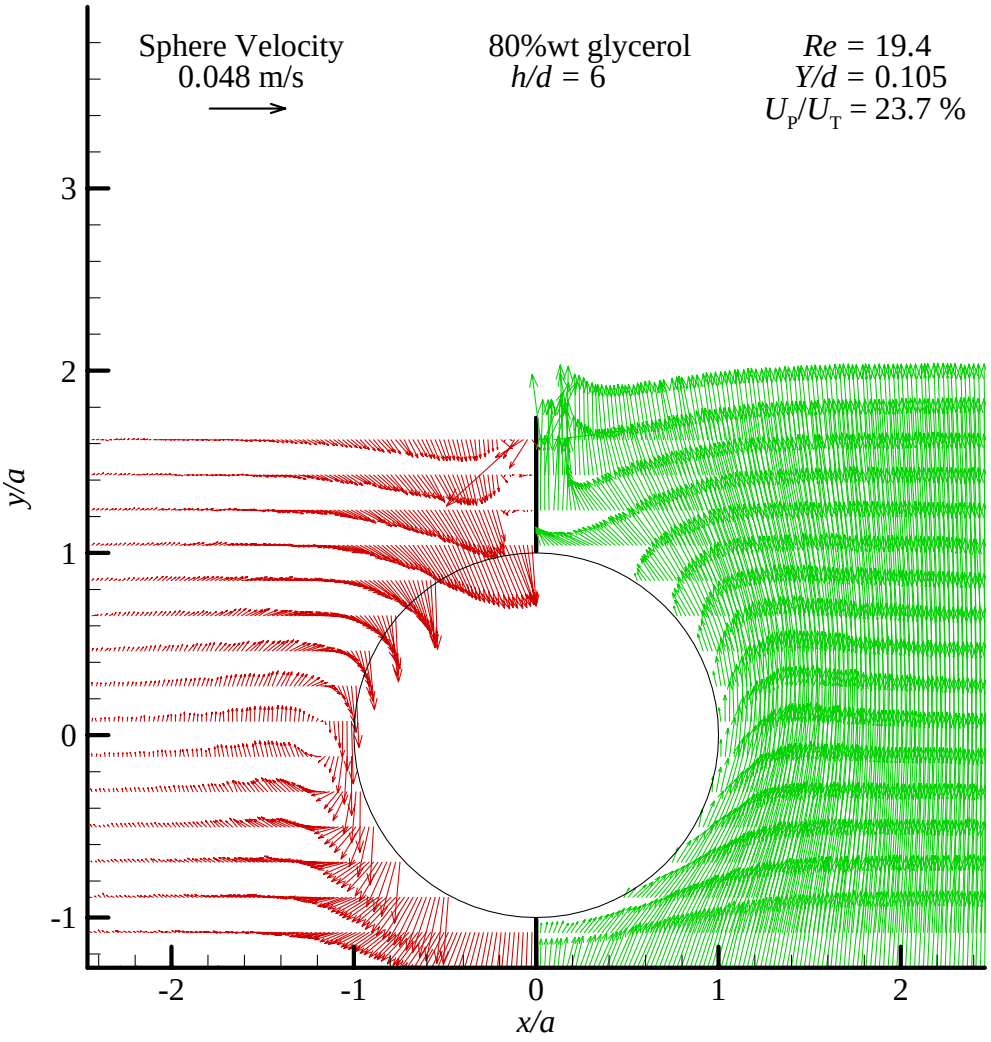

Figure 4.9: Velocity field around a falling solid sphere. The left side shows velocities with respect to the moving sphere while the right is with respect to a stationary sphere. 80%wt glycerol, h/d = 6.0, Y/d = 0.105, U_P = 48.7 mm/s, Re = 19.4, U_P/U_T = 23.7%. For clarity, only every eighth row of vectors is shown.

The general trend of the fluid motion is shown in the left half of Figure 4.9 with respect to the moving sphere. In the infinite fluid case shown, the fluid directly in the path of the moving sphere is pushed downward by the motion of the sphere. This causes fluid to move upward around the equator, and finally return directly behind the sphere as the sphere passes. The velocity profile at the equator of the sphere shows that the velocity vectors have a sign reversal, meaning the fluid is changing direction. Near the surface of the sphere, fluid is moving in the direction of the sphere due to the no-slip

condition. Further into the fluid, a point of zero velocity is found, beyond which the fluid is moving in the opposite direction of the sphere. The figure shows that the fluid velocity drops to negligible values within one sphere diameter from the sphere's surface. This shows that the plane walls of the tank do not influence the velocity field, and the fluid behaves as an infinite fluid. Thus, the velocity field in this case should be axisymmetric. There is a small region directly above the sphere where the velocity profile appears to be discontinuous. This is where the suction cup of the release mechanism was located, and the PIV system cannot make measurements in this region.

Figure 4.10 shows the velocity field around the sphere as it approaches terminal velocity for the same wall spacing and fluid concentration as in Figure 4.9. However, in Figure 4.10 the flow is nearly steady, and the vorticity generated at the surface of the sphere during the transient has had time to diffuse farther into the fluid. The flow remains axisymmetric, however, as opposed to a creeping flow case, there is no fore-and-aft symmetry as a wake pattern develops. With respect to the moving sphere, shown in the left half of the figure, the fluid appears to rotate about a point of zero velocity. This point will be referred to as the centre of rotation throughout this thesis. During the transient, this centre of rotation moves from the surface of the sphere at the equator out into the fluid. In the case of creeping flow around a sphere, the flow has fore and aft symmetry and this centre of rotation would move away from the sphere surface horizontally along the equatorial line of symmetry. In the 80%wt glycerol case, the high Reynolds number causes the centre of rotation to also trail behind the sphere.

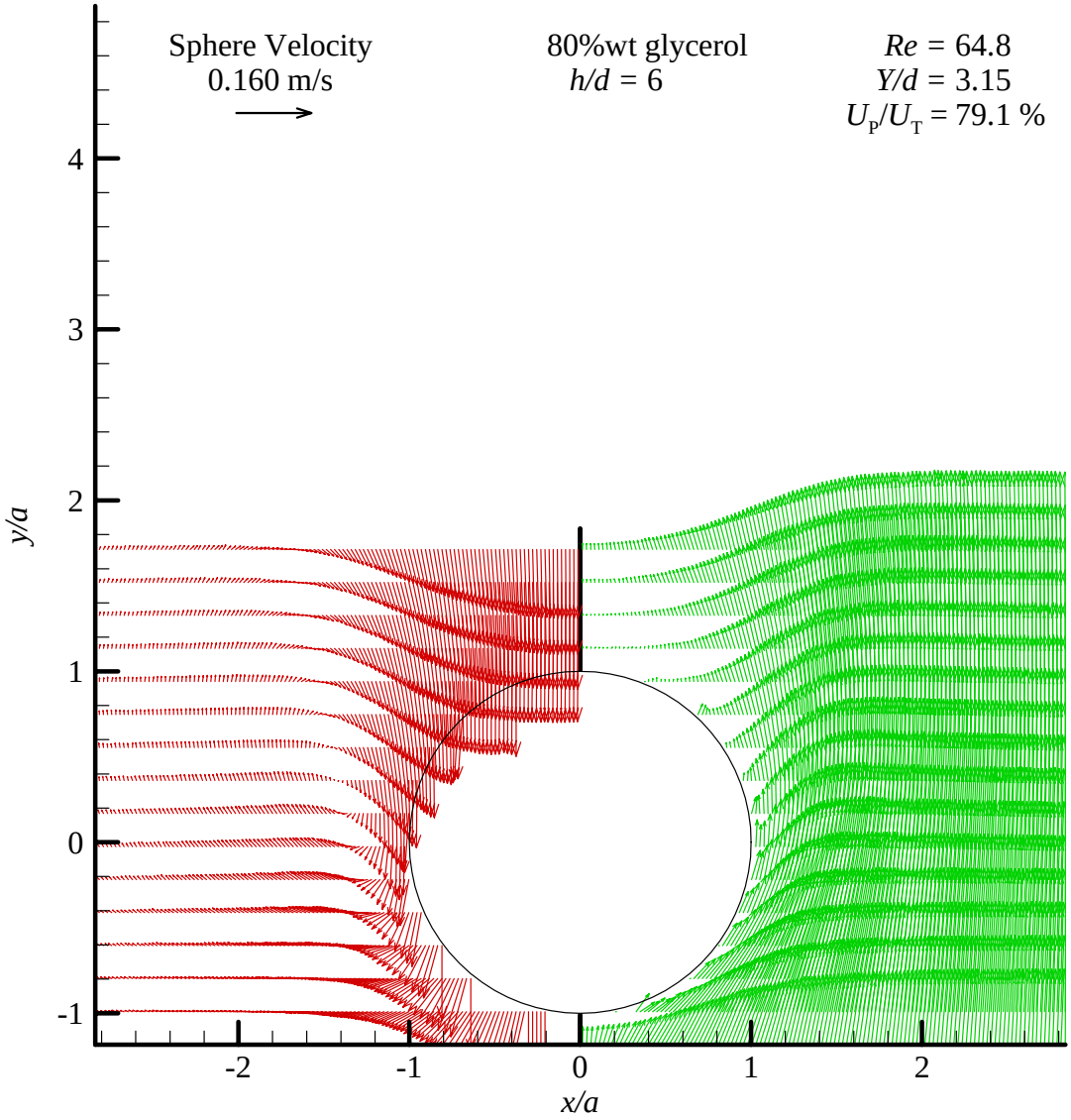

Figure 4.10: Velocity field around a falling solid sphere. The left side shows velocities with respect to the moving sphere while the right is with respect to a stationary sphere. 80%wt glycerol, h/d = 6.0, Y/d = 3.15, U_P = 159.7 mm/s, Re = 64.8, U_P/U_T = 79.1%. Every eighth row of vectors is shown.

Comparing Figures 4.9 and 4.10, we see that the velocity gradients in the fluid near the surface of the sphere grow throughout the transient. This leads to high shear stresses near the sphere surface. As the sphere approaches terminal velocity the shear stresses at the equator of the sphere increase. A more detailed examination of this effect will be shown following the presentation of velocity fields where the walls have an effect.

For comparison to Figure 4.10, velocity fields obtained late in the transient during the closer wall spacing tests will be shown in Figures 4.11 and 4.12.

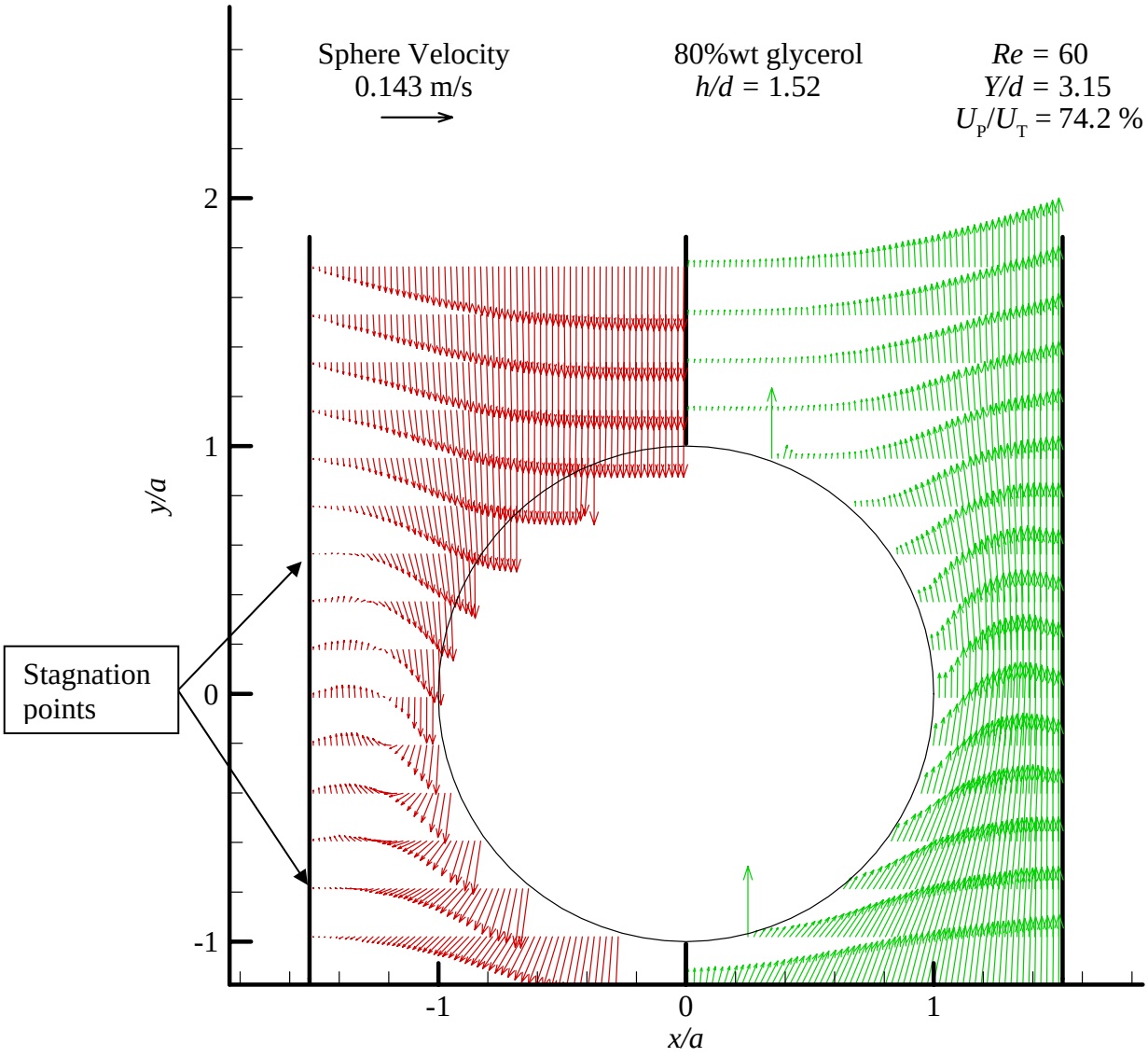

Figure 4.11: Velocity field around a falling solid sphere. The left side shows velocities with respect to the moving sphere while the right is with respect to a stationary sphere. 80%wt glycerol, h/d = 1.5, Y/d = 3.15, U_P = 143 mm/s, Re = 60, U_P/U_T = 74.2%. Every eighth row of vectors is shown.

Figure 4.11 shows the velocity field for a wall spacing of h/d = 1.5 for the 80%wt glycerol case at the same location (Y/d = 3.15) as was shown in Figure 4.10 for the unbounded case. The fluid motion has been constrained between the surface of the sphere and the wall. Examining the velocity profile at the equator of the sphere, it is

apparent that there are velocity gradients at the wall as well as at the surface of the sphere. This means that the motion of the sphere creates shear stresses not only at the surface of the sphere, but also along the plane walls.

It must be remembered that the sphere is moving between parallel plates, and these vector fields represent the velocities only in one plane of the fluid. The fluid is unconstrained in the page-normal direction, thus the velocity profiles will change on planes with other azimuthal positions. The effect of the walls is to restrict the motion of the fluid between the walls and the sphere surface, thus more fluid passes around the sphere in the page-normal direction. Examining the wake structure in the left half of Figure 4.11, the recirculating region beside the sphere is bound by two stagnation points on the wall where shear stress falls to zero. All of the fluid outside these stagnation points, in this plane, moves in the same direction as the sphere.

In Figure 4.12, the wall spacing is further decreased. With $h/d = 1.2$ the terminal velocity field shows no recirculation beside the sphere. In this case, the proximity of the walls has completely blocked the fluid from moving around the sphere in the plane shown. All of the fluid is now passing around the sphere in the page-normal direction.

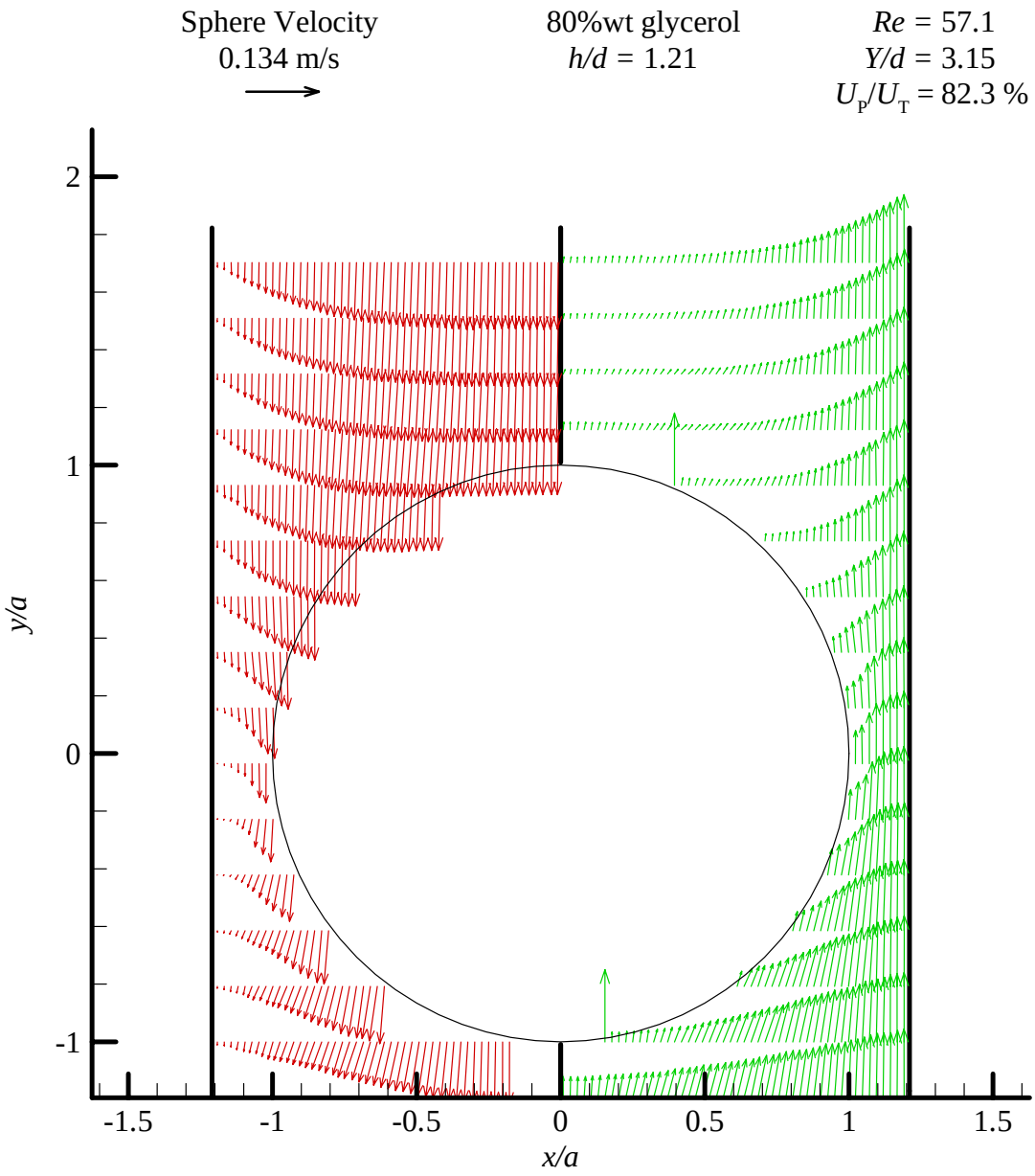

Figure 4.12: Velocity field around a falling solid sphere. The left side shows velocities with respect to the moving sphere while the right is with respect to a stationary sphere. 80%wt glycerol, h/d = 1.2, Y/d = 3.15, U_P = 134 mm/s, Re = 57, U_P/U_T = 82.3%. Every eighth row of vectors is shown.

With the elimination of the recirculating region beside the sphere, the velocity gradients at the wall do not change sign. All of the fluid moves in the same direction as the sphere in this plane, thus the shear stresses along the wall and at the surface of the sphere are in the same direction.

Without some scalar characterization of the images, it is very difficult to compare one velocity field to another in meaningful ways. It is with this in mind that we return to the idea of the centre of rotation. Consider only the left half of Figure 4.10. The path of the fluid can be seen more clearly with the addition of stream traces as shown in Figure 4.13. Stream traces represent the path that a fluid particle would take through the velocity field.

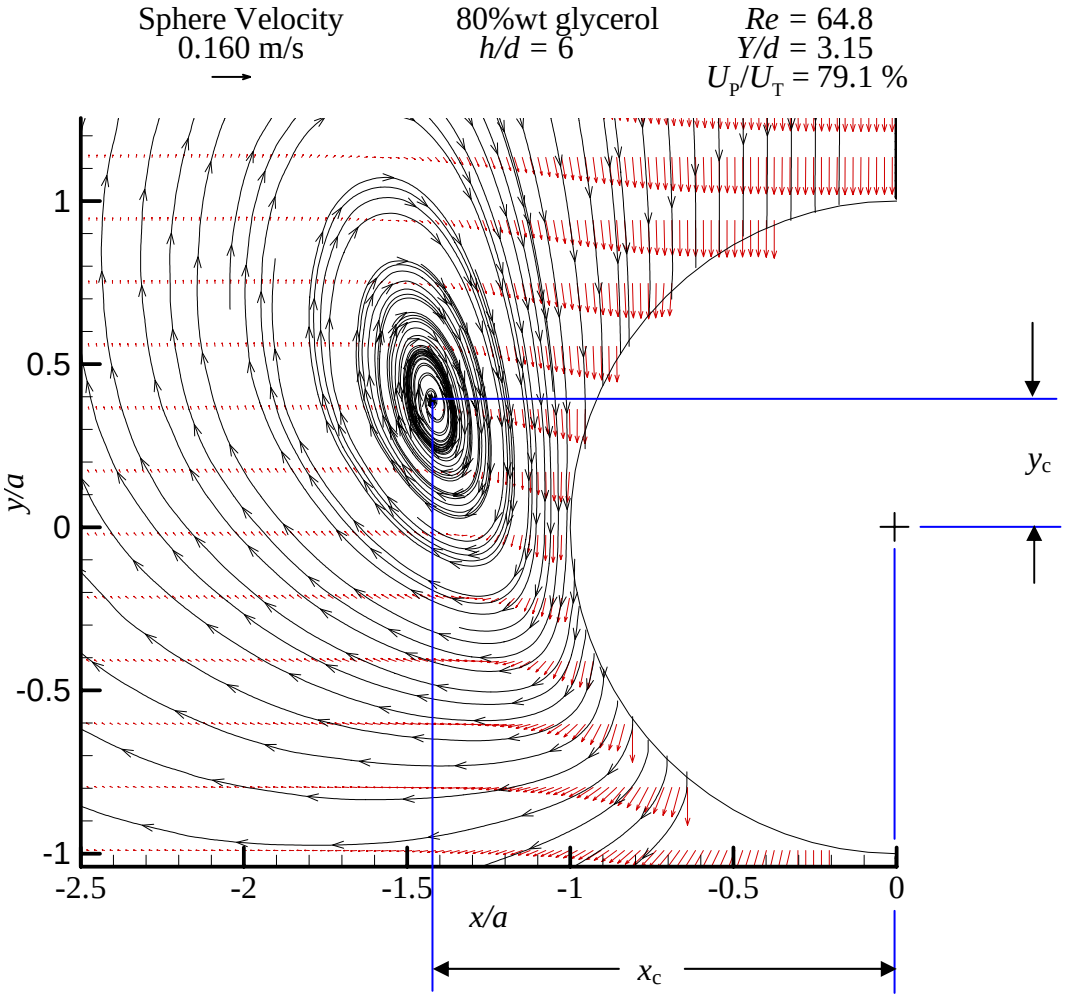

Figure 4.13: Stream traces are added to the unbounded fluid case to identify the flow patterns. The coordinates x_c and y_c represent the location of the centre of fluid rotation with respect to the centre of the sphere. 80%wt glycerol, h/d = 6.0, Y/d = 3.15, U_P = 160 mm/s, Re = 65, U_P/U_T = 79%. Every eighth row of vectors is shown.

The addition of stream traces makes the centre of rotation of the fluid very apparent. Figure 4.13 shows the infinite fluid case for 80%wt glycerol late in the transient. In the figure the coordinates x_c and y_c represent the location of the centre of rotation with respect to the centre of the sphere. The centre of rotation moves out into the fluid as the sphere accelerates to terminal velocity. Figure 4.14 shows the location of the centre of rotation at the five different points along the transient where PIV measurements were made for the 80%wt glycerol, h/d = 6.0 case.

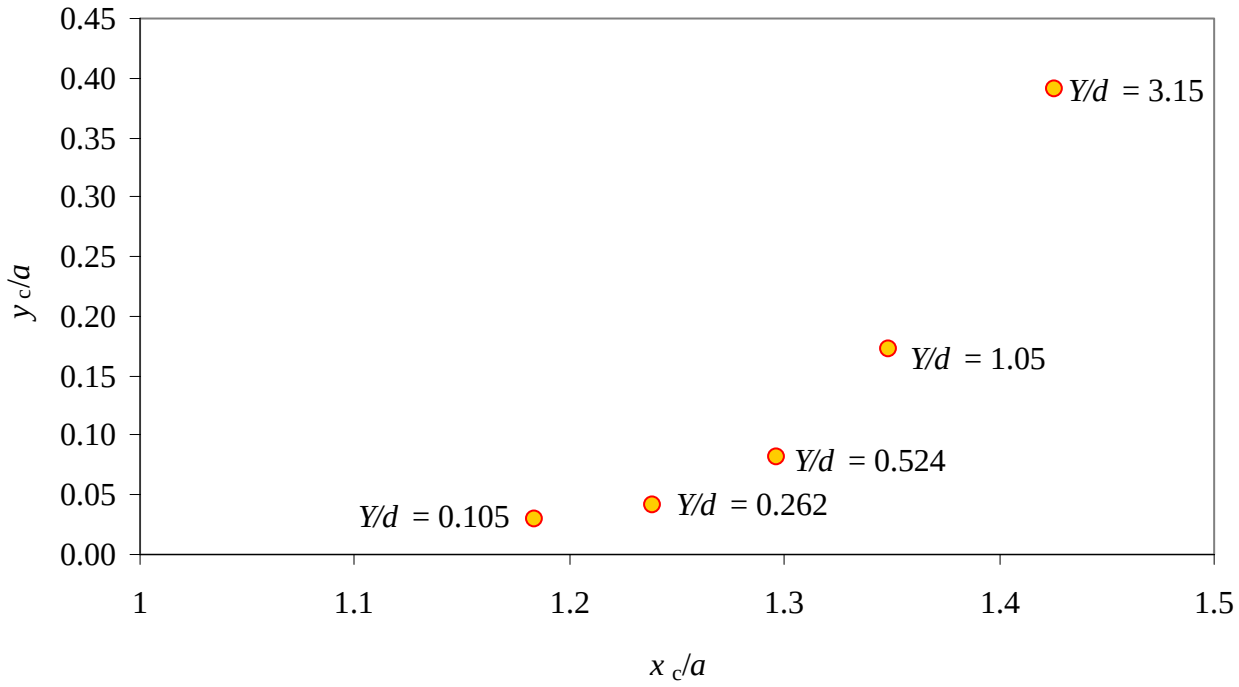

Figure 4.14: Evolution of the centre of rotation for 80%wt glycerol, h/d = 6.0. The location of the centre of rotation is normalised with the sphere radius.

A clear trend is observed where the centre of fluid rotation moves quite rapidly away from the surface of the sphere horizontally, and then begins to trail the sphere as it accelerates to terminal velocity. In this figure, x_c/a = 1 is the sphere surface. Presumably, at the instant that the sphere is released from rest, the centre of rotation of the fluid sits right on the surface of the sphere at the equator. That location would be (1, 0) in Figure 4.14, which tends to fit the trend of the observed data. Due to the viscosity

of the fluid and the no slip condition at the surface of the sphere, the centre of rotation is very quickly moved out into the fluid as the sphere accelerates. As well, Figure 4.14 shows the flow pattern losing its fore-and-aft symmetry as the centre of rotation diverges from the equatorial plane and trails behind the sphere. Unfortunately, the evolution of the centre of rotation tells us nothing of the evolution of the *shape* of the vortex structure.

Figure 4.15 shows the evolution of the centre of rotation as the wall spacing narrows. In this case the spacing is $h/d = 1.5$, and the diffusion of vorticity is constrained by the walls. The vertical scale is $1/10^{th}$ that of Figure 4.14.

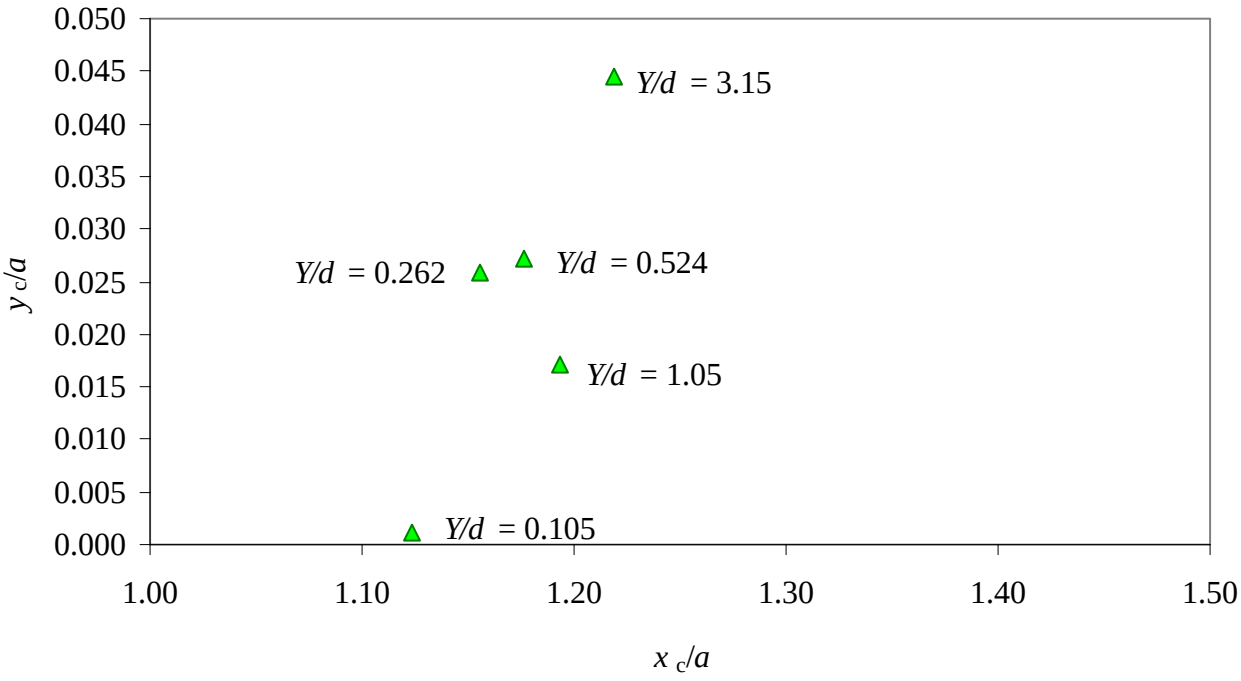

Figure 4.15: Evolution of the centre of rotation for 80%wt glycerol, $h/d = 1.5$. The location of the centre of rotation is normalised with the sphere radius.

In this case, although there is a trend for the centre of rotation to move away from the sphere and trail behind, the effect is very much reduced. Once the centre of rotation is established, it hardly moves with respect to the sphere as the sphere accelerates to terminal velocity. As noted earlier, as the walls move closer, the vortex structure is

completely eliminated between the sphere and the wall, thus there is no centre of rotation in this plane for the h/d = 1.2 case for 80%wt glycerol.

No centre of rotation data could be obtained for the 100%wt glycerol. In the h/d = 6.0 case, the centre of rotation is outside of the field of view. Quite tellingly, the h/d = 1.5 case shows no fluid rotation between the sphere and the wall, which demonstrates the importance of viscosity in terminating the vortex structure in this region. For higher viscosities, the vortex structure is eliminated for wider wall spacings. The h/d = 1.2 case shows no vortex structure either. The exact relationship between the fluid viscosity, wall spacing and vortex elimination could not be established since only three wall spacings and two fluid viscosities were examined in this study.

4.6 Velocity Profiles at the Equator

Reference has been made to the velocity profile at the equator of the sphere several times in this thesis. The velocity profile at this location is important as it shows how the fluid is moving in the gap between the walls and the surface of the sphere. It is in this region where the effect of the wall proximity will be manifested. Specifically, the velocity profile will demonstrate how shear stresses in the fluid change throughout the transient and for different wall spacings.

First, consider the widest wall spacing, h/d = 6, for the 80%wt glycerol case. In each case, the vertical component of velocity, v, has been normalised with the instantaneous sphere velocity. The profiles compared in Figure 4.16 are taken from the earliest time in the transient (Y/d = 0.105) and the latest time (Y/d = 3.15).

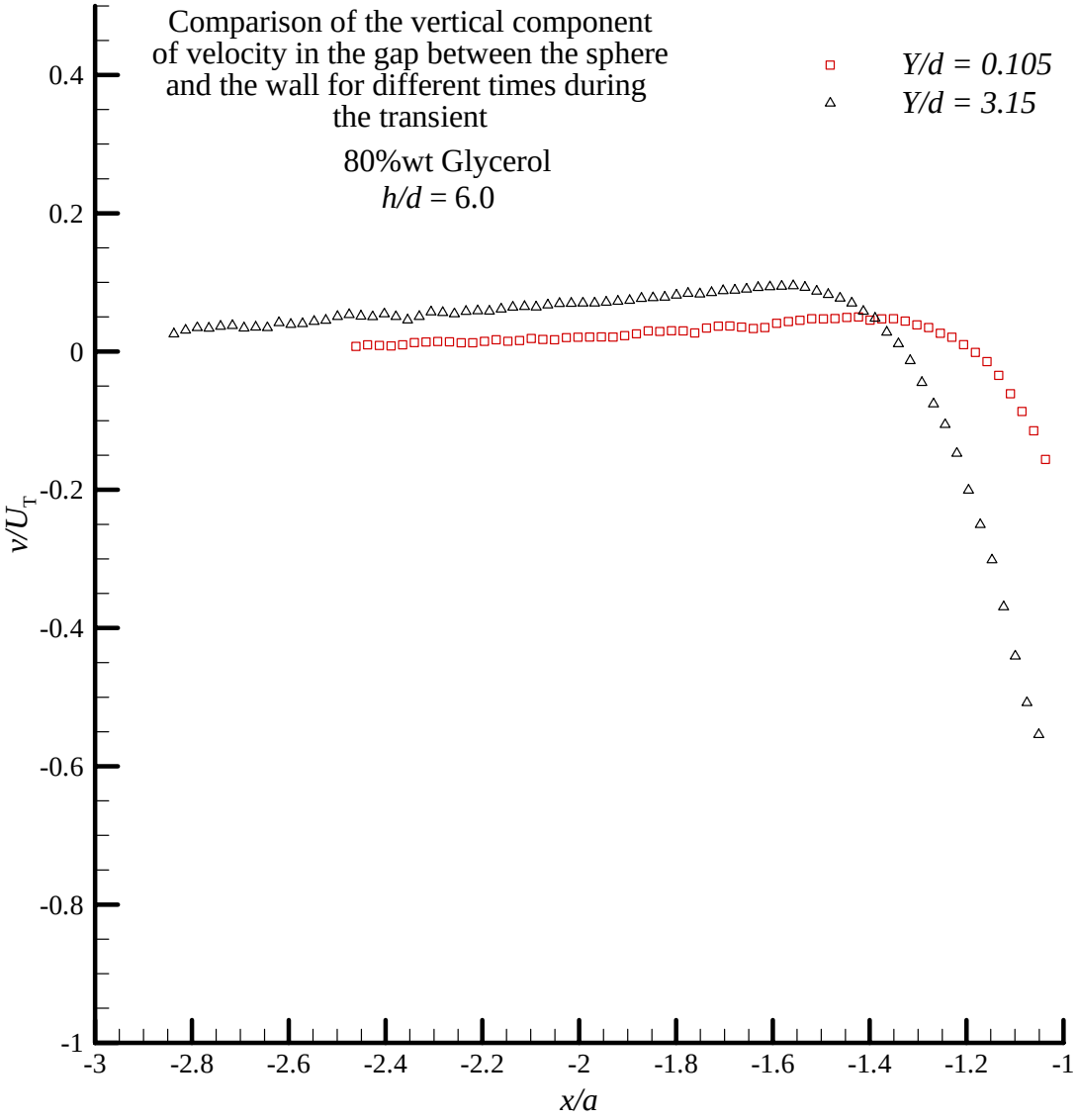

Figure 4.16: Velocity profile at the equator of the falling sphere at two times in the transient for 80%wt glycerol, $h/d = 6$. Fluid velocities are normalised with respect to the terminal sphere velocity.

In Figure 4.16 the square symbols are the fluid velocities early in the transient where the sphere has reached 23% of terminal velocity, while the black symbols are taken when the sphere is nearly 80% of its terminal velocity. In these figures, $x/a = -1$ represents the surface of the sphere.

The data in Figure 4.16 show the velocity of the fluid matching the sphere velocity at the sphere's surface, and decaying to zero far away from the sphere in each case. Early in the transient the slope of the velocity profile is lower at the surface of the

sphere and the gradient increases throughout the transient. This indicates that the shear stress at the sphere increases throughout the transient. As the transient evolves, Figure 4.16 shows higher velocities far from the sphere later in the transient. Whenever the velocity goes above zero, this indicates that the fluid is moving in the opposite direction than the sphere, which indicates a recirculating region.

Figure 4.17 compares the velocity profiles in the 80%wt glycerol case where the wall spacing is h/d = 1.5. In this case the latest time in the transient shown is Y/d = 1.05, since it was found that the Y/d =3.15 case did not give valid data since the camera and release mechanism were jarred. However, the times shown give a good indication of how the velocity profile changes from the infinite case. In this case, the no-slip condition means the fluid velocity is zero at the wall. This introduces a shear stress at the wall acting in the same direction as the shear stress on the sphere. As with the infinite fluid case, the slope of the velocity profile at the sphere, and thus the shear stress, increases throughout the transient. Near the wall, the fluid velocities are positive indicating the fluid is moving upwards around the sphere as it passes. These upward fluid velocities near the wall remain fairly consistent throughout the transient, while the velocities near the sphere increase as the sphere accelerates. This tends to suggest that more of the fluid is moving around the sphere in other azimuthal planes as the sphere velocity increases. This is likely due to the constriction imposed by the walls in this plane.

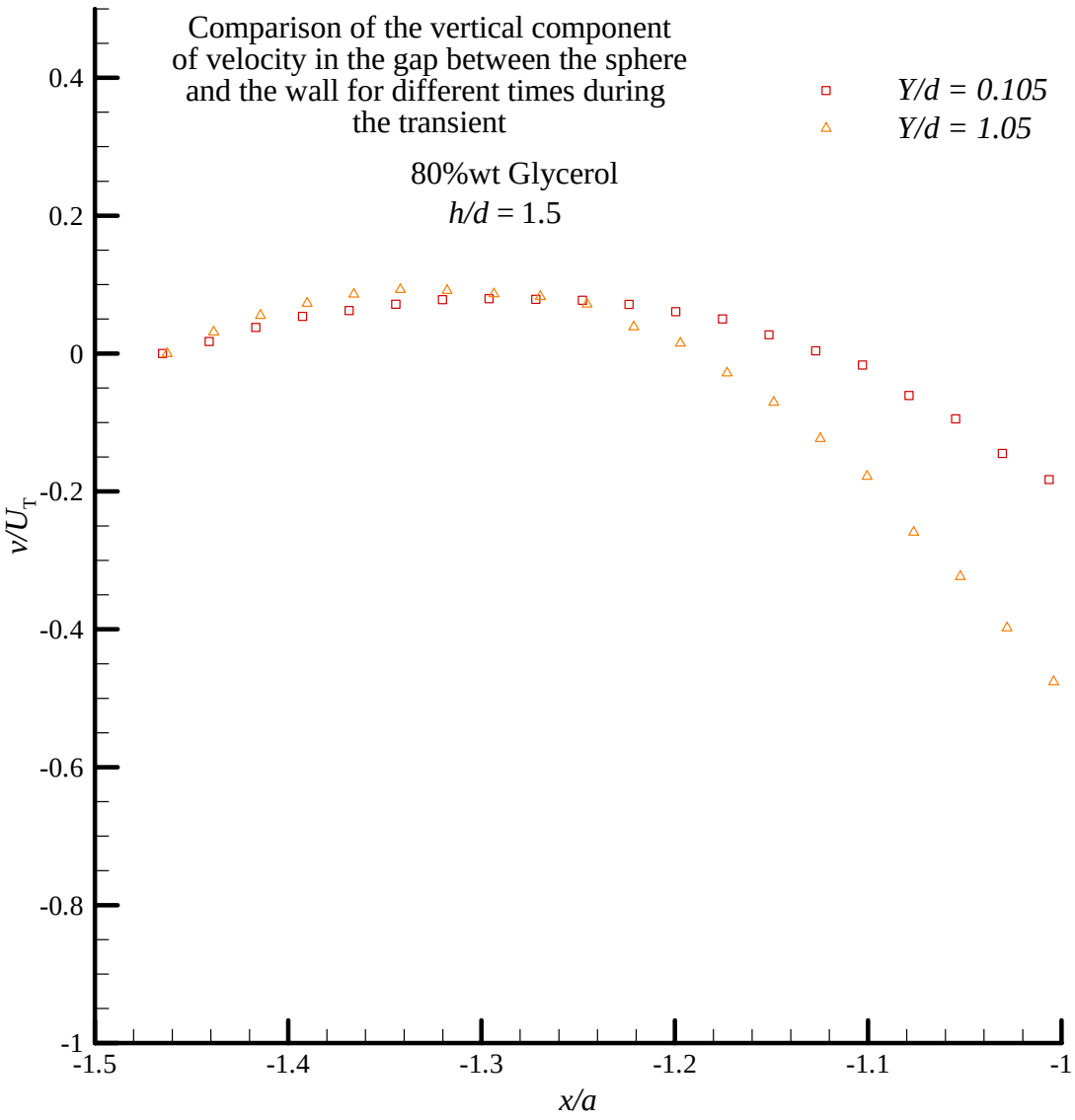

Figure 4.17: Velocity profile at the equator of the falling sphere at two times in the transient for 80%wt glycerol, h/d = 1.5. Fluid velocities are normalised with respect to the terminal sphere velocity.

Figure 4.18 shows the narrowest wall spacing of h/d = 1.2 for the 80%wt glycerol case. In this case, there are no positive velocities on the profile for either location in the transient which indicates that the recirculating vortex structure has been completely eliminated in this plane. All of the fluid now moves around the sphere in the page-normal direction. As with the previous two figures, the velocity gradient at the sphere increases throughout the transient, and momentum diffuses away from the sphere as it accelerates.

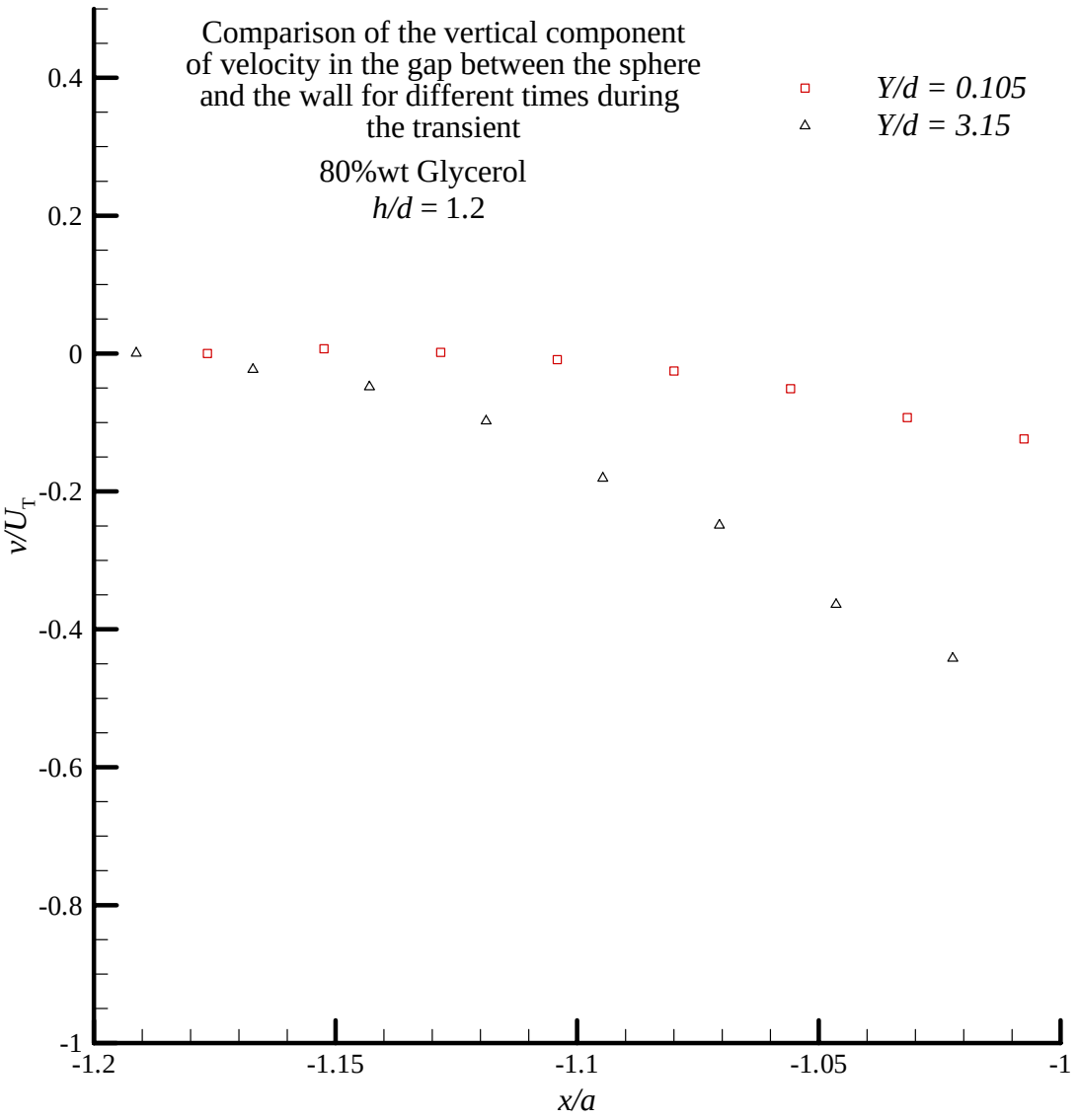

Figure 4.18: Velocity profile at the equator of the falling sphere at two times in the transient for 80%wt glycerol, h/d = 1.2. Fluid velocities are normalised with respect to the terminal sphere velocity.

The velocity profiles for the 100%wt glycerol cases show a somewhat different trend. The infinite fluid case is shown in Figure 4.19.

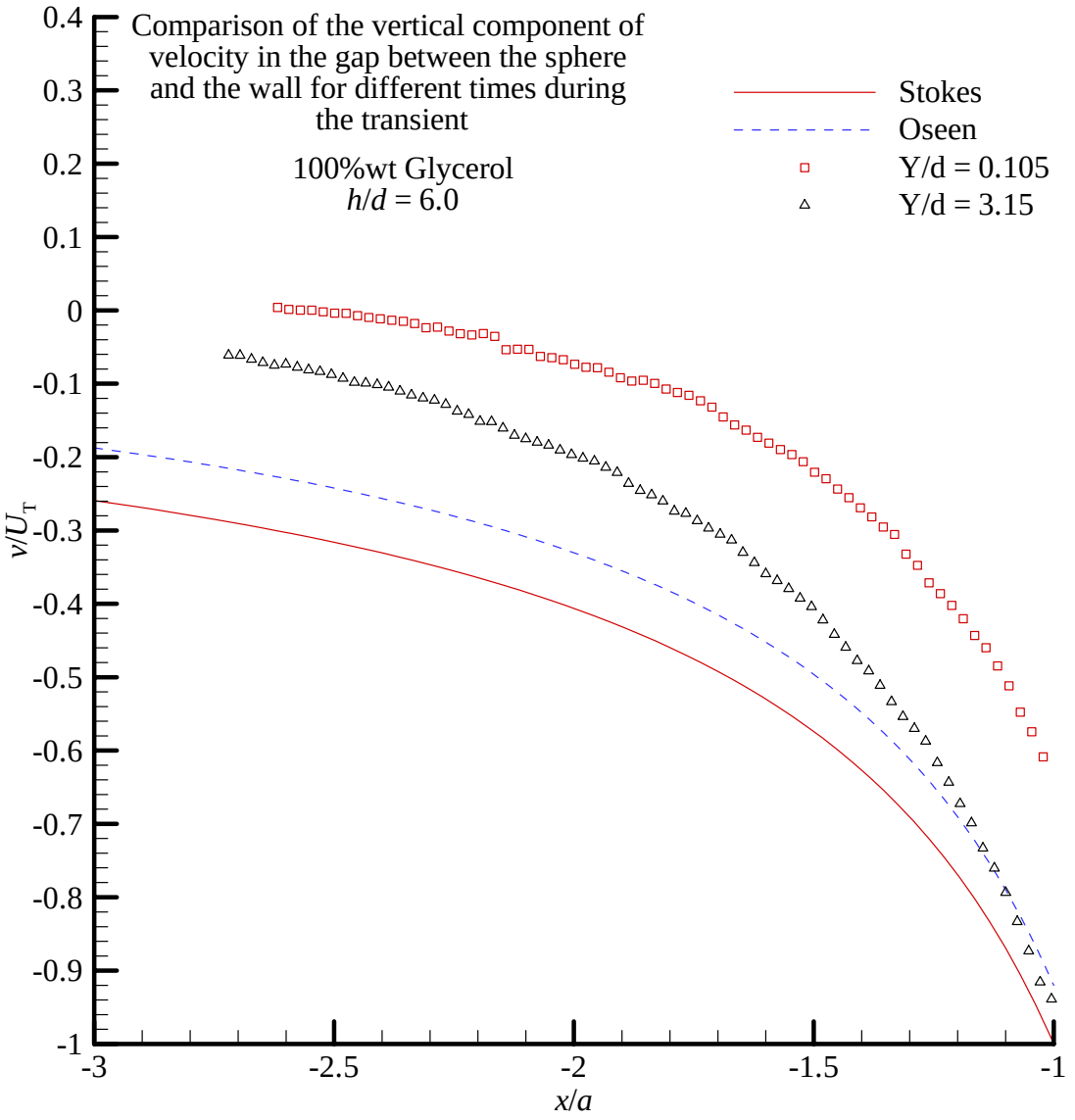

Figure 4.19: Velocity profile at the equator of the falling sphere at two times in the transient for 100%wt glycerol, $h/d = 6$. Fluid velocities are normalised with respect to the terminal velocity of the sphere. Stokes' solution and Oseen's approximation have been included for comparison.

In the 100%wt glycerol cases, the high viscosity of the fluid allows the momentum of the sphere to be transported into the fluid very quickly. In Figure 4.19, no positive velocities exist. However, since the velocity field is axisymmetric in this case, there must be a region of positive velocity outside of the field-of-view allowing fluid to

move to the rear of the sphere. As with the lower viscosity case, the 100%wt glycerol shows that the velocity gradient at the sphere increases throughout the transient. Since the case shown in Figure 4.19 represents an unbounded fluid with a low terminal Reynolds number, the velocity profiles predicted from Stokes' solution from equation (2.20) and Oseen's approximation from equation (2.27) are shown for comparison to the experimental data. Here we see the limitation of these solutions for real flows. Stokes' solution is only valid for zero Reynolds number so is not strictly comparable to the current study. However, the "infinite drift" predicted by Stokes is demonstrated since the motion of the sphere has an effect on the fluid far from the sphere. Oseen's approximation is scaled with Reynolds number and represents a better fit than Stokes, although this solution predicts infinite drift as well. The Reynolds number used for the Oseen solution was $Re = 0.452$ which is the same Reynolds number as the $Y/d = 3.15$ case in the experimental data. Even at this low Reynolds number, the Oseen solution overpredicts the velocities in the fluid, suggesting that Oseen's solution is only applicable for a very small range of Reynolds number and only close to the sphere.

Figure 4.20 shows the $h/d = 1.5$ case for 100%wt glycerol. In this case, the velocity profiles are nearly coincident. This means that the velocity profile in this plane is fully developed by the time the sphere has moved 10% of its diameter. In this case there is no recirculation of the fluid around the sphere in this plane.

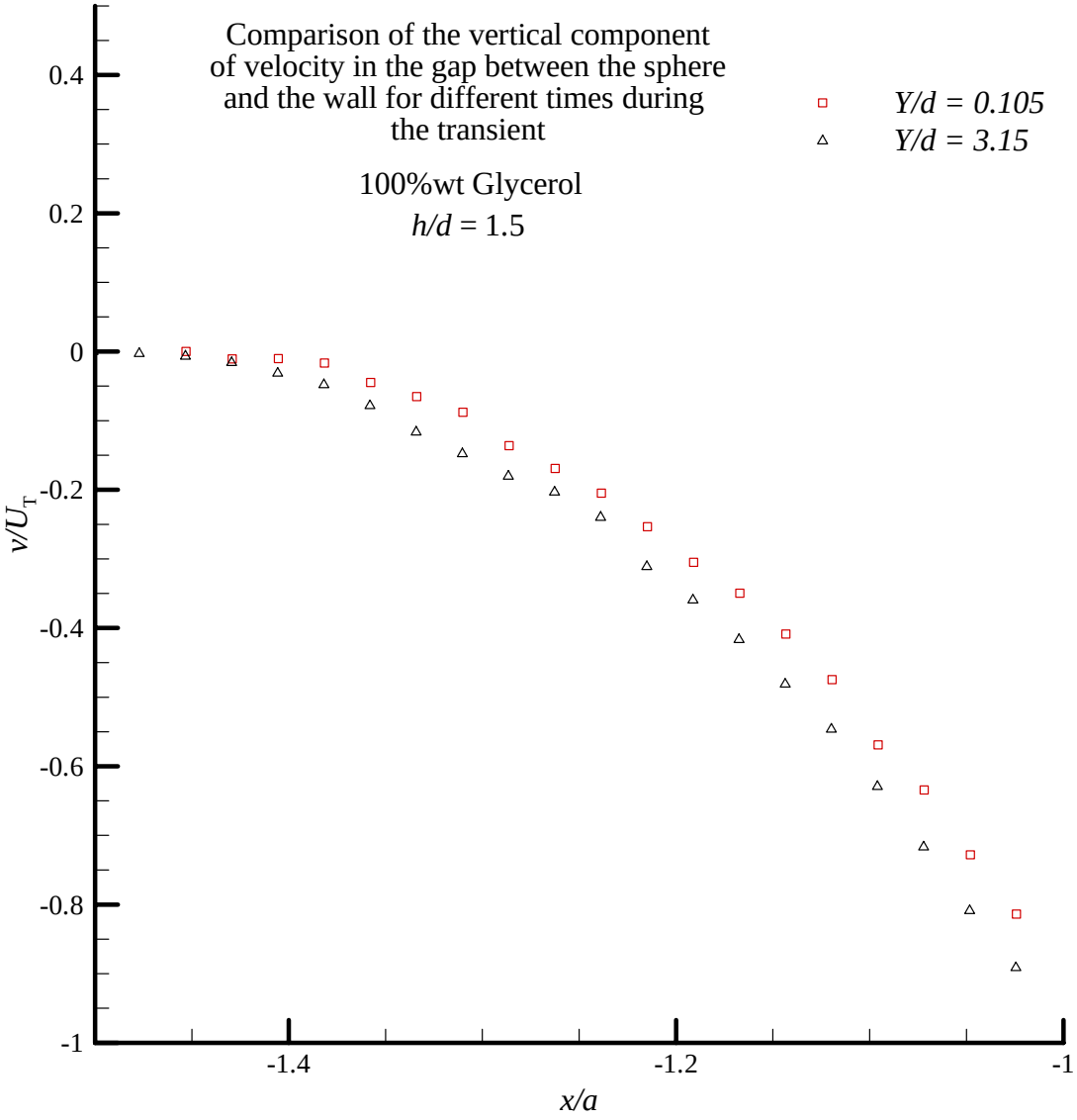

Figure 4.20: Velocity profile at the equator of the falling sphere at two times in the transient for 100%wt glycerol, h/d = 1.5. Fluid velocities are normalised with respect to the terminal velocity of the sphere.

The vortex structure between the sphere and the wall has been eliminated for a wider wall spacing than in the 80%wt glycerol case. Finally, Figure 4.21 shows the wall spacing of h/d = 1.2 for the 100%wt glycerol case.

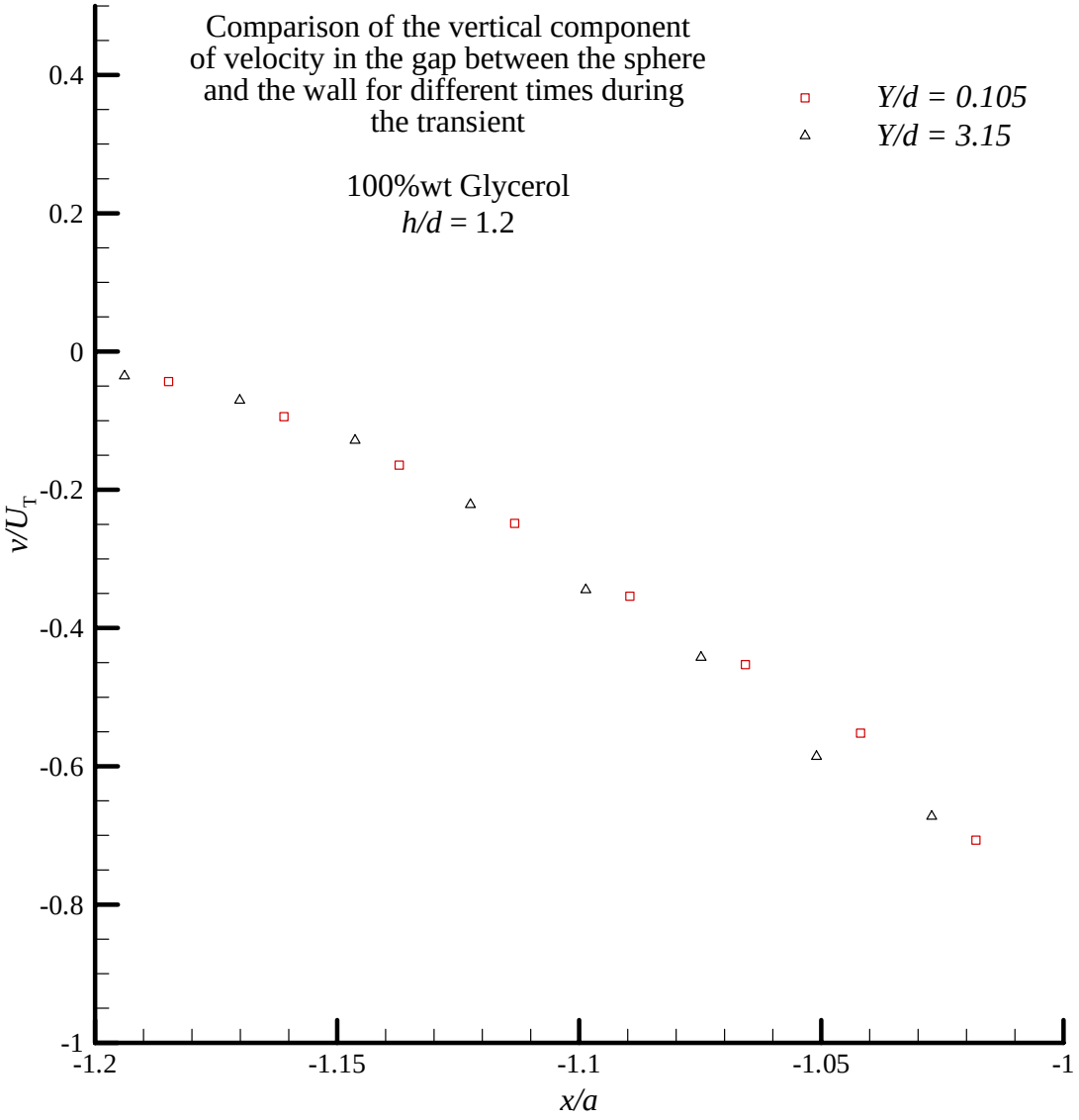

Figure 4.21: Velocity profile at the equator of the falling sphere at two times in the transient for 100%wt glycerol, h/d = 1.2. Fluid velocities are normalised with respect to the terminal velocity of the sphere.

This case is very similar to the h/d = 1.5 case shown in Figure 4.20 since the flow becomes fully developed very early in the transient in the plane shown at this wall spacing as well. Comparing these two figures, the main difference is the curvature of the profile which is greater in the h/d = 1.5 case. The h/d = 1.2 case shows an approximately

linear velocity profile indicating that as the wall spacing decreases, the flow in the region between the sphere and the walls becomes very similar to Couette flow.

4.7 Shear Stresses at the Sphere Surface and at the Wall

Two import features of the velocity profiles just discussed are the velocity gradient at the surface of the sphere, and the velocity gradient at the wall. These velocity gradients have been used to determine the shear stress at the surface of the sphere at its equator, as well as the distribution of the shear stresses along the plane wall. In each case a third order polynomial was fit to the first three velocity vectors in the fluid. At the wall, the velocity was forced to be zero due to the no slip condition. At the surface of the sphere, the velocity was forced to be the instantaneous sphere velocity. The first derivative of the polynomial then allowed the slope of the velocity profile to be determined at the wall and at the surface of the sphere. Figures 4.22 and 4.23 show the shear stress at the equator of the sphere for the 80%wt and 100%wt glycerol cases, respectively.

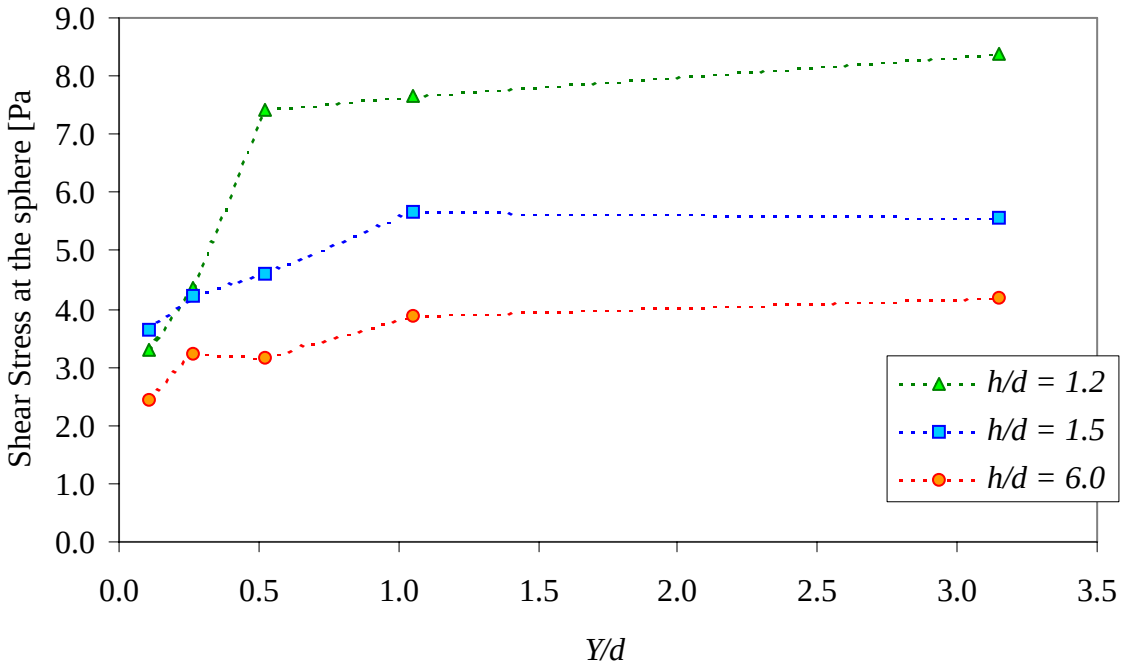

Figure 4.22: Shear stress at the surface of the sphere at the equator for 80%wt glycerol, comparing the different wall spacings throughout the transient.

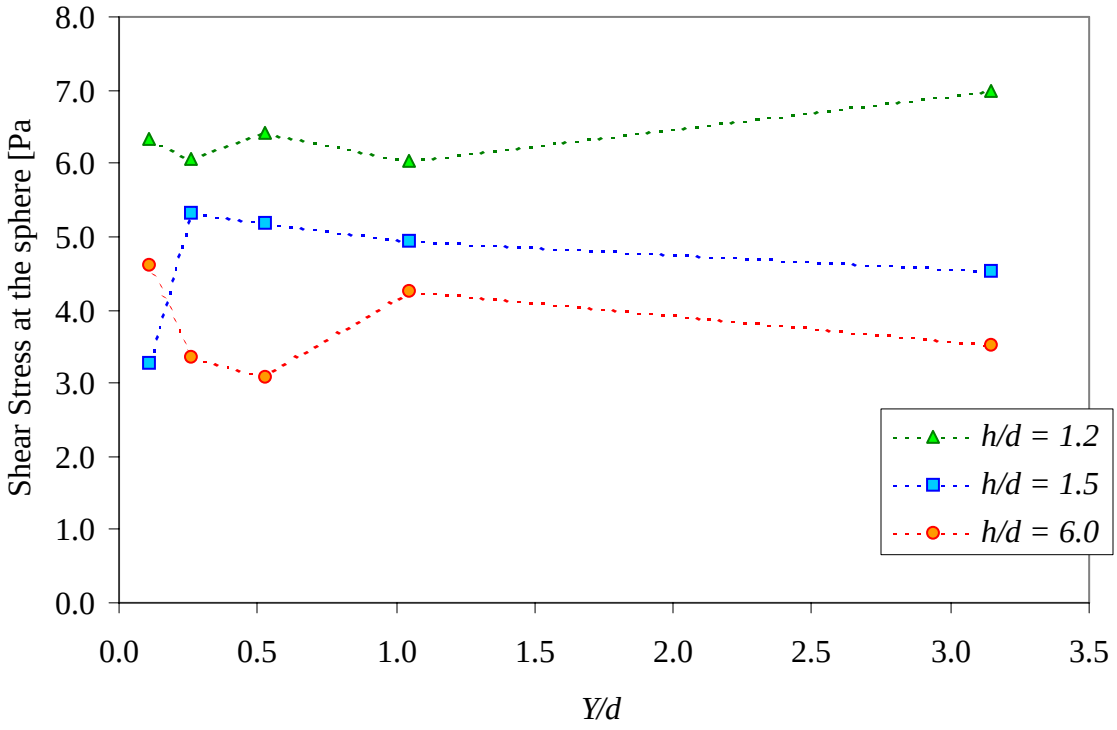

Figure 4.23: Shear stress at the surface of the sphere at the equator for 100%wt glycerol, comparing the different wall spacings throughout the transient.

The 80%wt cases shown in Figure 4.22 demonstrate that the shear stress at the sphere continually increases throughout the transient. The sphere is experiencing a gradual acceleration from rest, rather than an impulsive start, therefore the shear stresses at the sphere will continue to increase until the sphere reaches terminal velocity. The earliest point in the transient yields approximately the same shear stress regardless of the wall spacing. This result is consistent with the observation that the vorticity generated at the surface of the sphere has not had time to diffuse into the fluid and has not yet interacted with the walls. The shear stress at the sphere surface rapidly increases early in the transient in the h/d = 1.2 case, and continues to increase throughout the transient but at a decreasing rate. The h/d = 1.5 case shows a similar increase in shear stress, but this trend is lower in magnitude and approaches a lower shear stress at terminal velocity. In the h/d = 1.2 case, the shear stress reaches its final value very early in the transient indicating that the flow develops very quickly. In the h/d = 1.5 case, the shear stress at the sphere surface increases more gradually. In Figure 4.15 it was shown that the centre of rotation

in this case did not move a great deal with respect to the centre of the sphere throughout the transient. This indicates that the flow pattern between the sphere and the wall is very quickly established for this wall spacing. The vortex structure bound between the sphere and the wall maintains its size and shape in this plane, while the velocity vectors within it increase in magnitude. Thus, as the velocity of the sphere increases, the velocity gradient increases as well causing the shear stress to grow throughout the transient. As the $h/d = 6$ case is relatively unconstrained by walls and is axisymmetric, the vorticity generated at the surface of the sphere is free to expand into the fluid at the same rate in all azimuthal directions. This tends to lower the shear stresses in the plane under consideration, since there is no wall to constrain the fluid motion.

The 100%wt glycerol cases show a similar trend in the shear stress at the equator of the sphere. However, in these cases, the sphere achieves terminal velocity much more quickly than the 80%wt glycerol case. As the sphere accelerates to terminal velocity, the flow becomes fully developed and the velocity field stops changing. At this point the shear stress at the sphere becomes constant.

The shear stress at the wall will be treated next. In this case, the slope of the velocity profile at the wall was calculated for each row of vectors in the entire velocity field. This yields a shear stress distribution along the wall for each location in the transient where PIV data was taken. Because finding the shear stress requires the slope of the velocity profile to be found, the shear stress is quite sensitive to uncertainty in the velocity measurements. The shear stress distributions obtained were thus quite "noisy" and a three-point moving average scheme was employed to smooth the data. Unfortunately, in the 100%wt glycerol case, the small magnitude of the velocity vectors near the walls greatly increased the uncertainty in the slope of the velocity profile. The resulting shear stress distribution in the 100%wt glycerol cases were simply too noisy to obtain meaningful data and will not be shown. The wall shear stress distribution for the 80%wt glycerol cases is shown in Figure 4.24 for the $h/d = 1.5$ case. The data are presented for each of the five locations during the transient where PIV measurements were made.

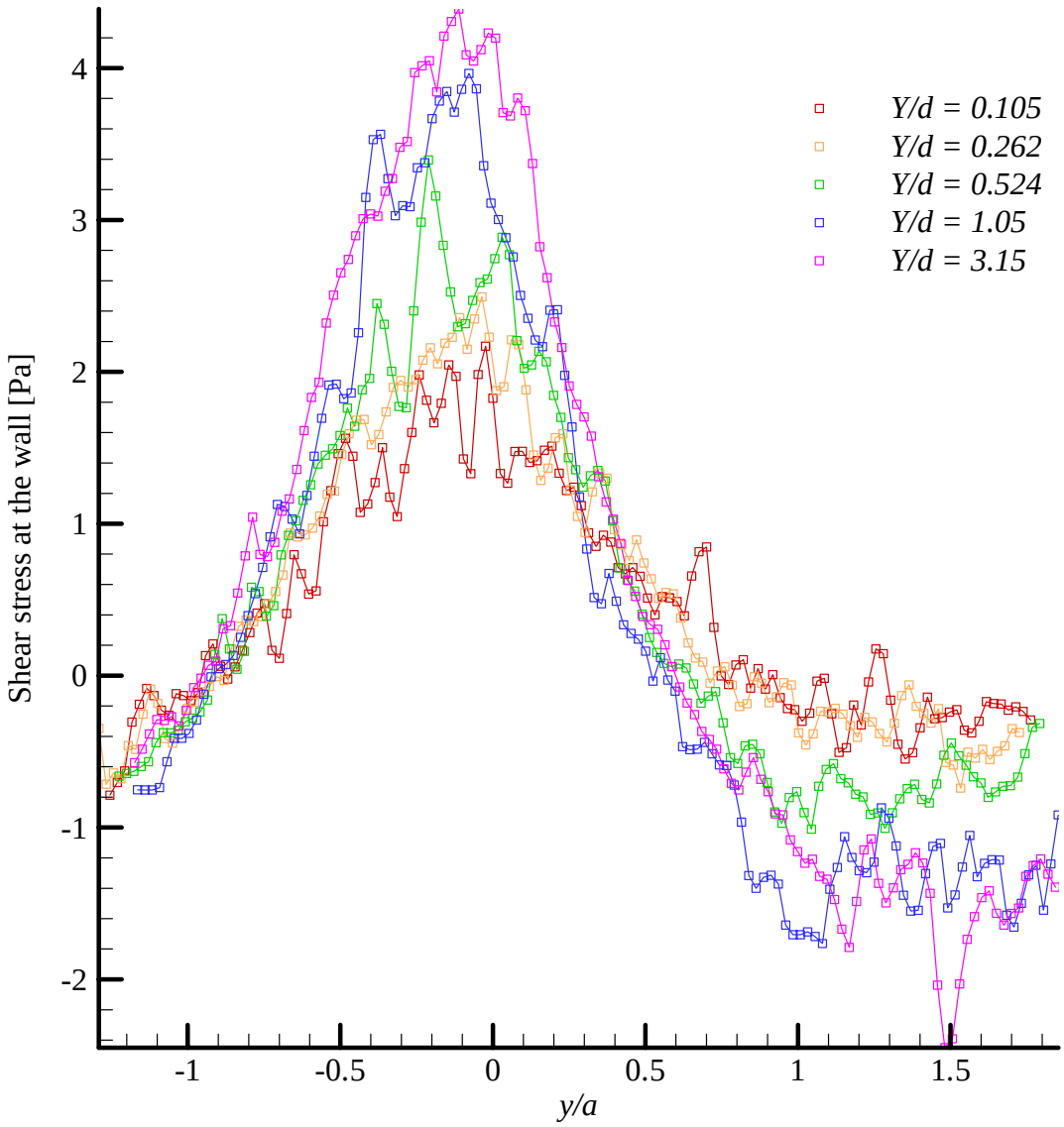

Figure 4.24: Shear stress at the wall for 80%wt glycerol, h/d = 1.5. The distance along the wall is normalised with the sphere radius.

Lines have been used to connect the data points in Figure 4.24. These have been included to facilitate the viewing of the different data sets only, and do not indicate anything about the shear stress between the individual data points. This figure shows that the maximum shear stress corresponds to the centre of the sphere, shown at $y/a = 0$, at each location in the transient. Also, each of the wall shear stress distributions crosses zero stress at roughly the same location along the wall. This sign reversal indicates that the fluid is changing direction. Where the shear stress is positive, the fluid is moving in the opposite direction to the sphere, and the fluid moves in the same direction as the

sphere when the shear stress at the wall is negative. This is best illustrated with a sample vector field showing stream traces. The vector field shown in Figure 4.25 is late in the transient where Y/d = 3.15 for the 80%wt glycerol, h/d = 1.5 case.

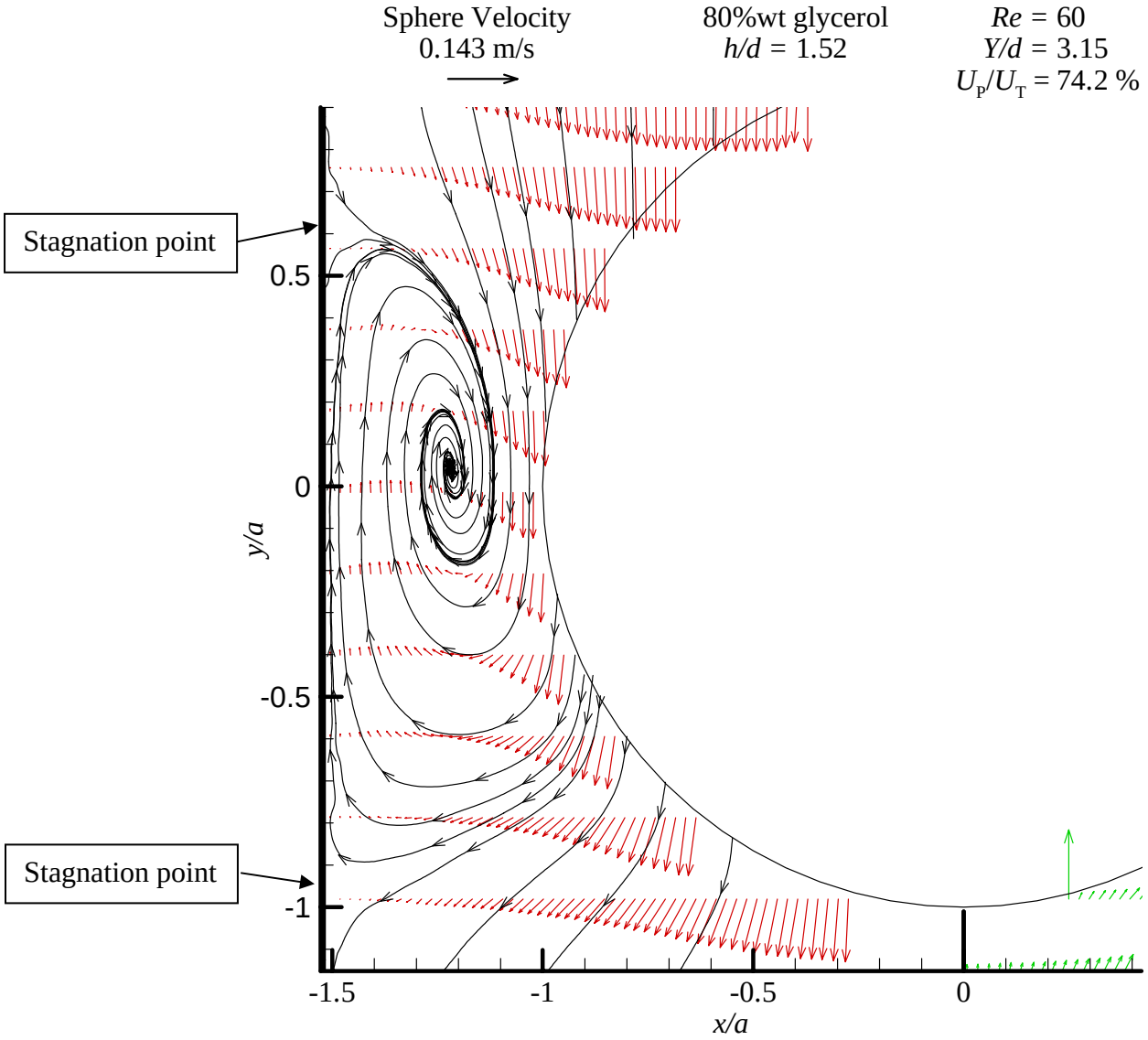

Figure 4.25: A close-up of the vortex structure between the wall and the sphere for the 80%wt glycerol, h/d = 1.5 case. Stream traces show the path of the fluid indicating stagnation points at the wall above and below the sphere. The vortex structure exists within these stagnation boundaries, while all of the fluid outside moves in the same vertical direction as the sphere. Every eighth row of vectors is shown.

The sign reversal of the shear stress at the wall, indicated in Figure 4.24, defines the stagnation points as indicated in Figure 4.25. Since the sign reversal in Figure 4.24 occurs at roughly the same location along the wall at each location in the transient, the boundary of the vortex structure between the sphere and the wall is established very early and does not change throughout the transient. While the extent of the vortex structure does not change, the magnitude of the velocity vectors within it become larger as the sphere accelerates. This causes the shear stress at the wall to increase in magnitude as the sphere approaches terminal velocity. Due to the uncertainty in the wall shear stress data, the rate at which the shear stress changes during the transient could not be established. It can, however, be reasoned that the wall shear stress will change quickest early in the transient since this is where the velocity of the sphere changes most rapidly.

Figure 4.26 shows the distribution of the shear stress at the wall for the 80%wt glycerol, h/d = 1.2 case. Figure 4.26 does not show the same sign reversal that was present in the h/d = 1.5 case for the 80%wt glycerol. This absence indicates that there is no longer a vortex structure between the sphere and the wall. All of the fluid in this gap moves in the same direction as the sphere. This means that fluid must move around the sphere in the page-normal directions.

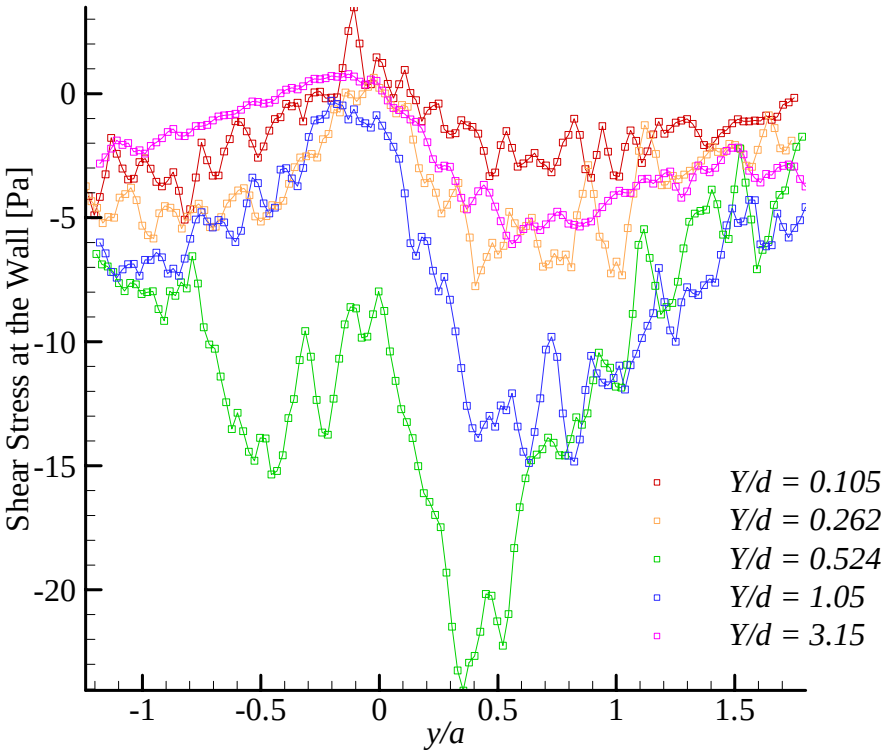

Figure 4.26: Shear stress at the wall for 80%wt glycerol, h/d = 1.2. The distance along the wall is normalized with the sphere radius.

There is not a clear trend of increasing or decreasing shear stress as the sphere moves along the transient. It can be said that the maximum shear stress at the wall occurs as the centre of the sphere passes. The Y/d = 0.524 case in particular does not appear to be consistent with the other curves. This may be due to measurement uncertainty, or perhaps indicates a transition phenomenon.

Chapter 5:
Conclusions and Recommendations for Future Work

The aim of this research was to use particle image velocimetry (PIV) to obtain full field velocity measurements around a sphere as it accelerates under the influence of gravity from rest to terminal velocity between plane walls. The measurement plane was perpendicular to the plane walls and included the centre of the sphere. Velocity fields were successfully obtained at five points during the transient for three different wall spacings and two different fluids. The wall spacings were h/d = 6.0, h/d = 1.5, and h/d = 1.2. A glycerol and water mixture was used for the test fluids. The 100%wt glycerol, unbounded case yielded a terminal Reynolds number of 0.6, which is within the traditional bounds of creeping flow. The 80%wt glycerol mixture gave a terminal Reynolds number of 72. Using Y to denote the distance the sphere has fallen from the release point, PIV measurements were made at locations where Y/d = 0.105, 0.262, 0.524 1.05 and 3.15.

The following conclusions may be made:

1. PIV is an effective technique for examining the two-dimensional velocity field at an instant in time.

   The velocity fields obtained in this research had very high spatial resolution. The spacing between the velocity vectors was approximately 0.5 mm. This means that each velocity field is composed of about 4000 individual velocity measurements. The strength of the PIV system is that this high volume of data is obtained very quickly. However, while PIV is very well suited to making velocity measurements in steady flows, it is less well suited to transient flows where the velocity field is changing in time. This is due to the limits on the repetition rate of the laser illumination, as well as the limited bandwidth on data transfer from the recording medium. In the current study, the lasers could be fired at a maximum of 15 Hz.

2. The PIV system was used in a novel way to measure the instantaneous velocity of the sphere.

Using separate pattern matching software, the shadow cast by the sphere was located in each of the two PIV frames, allowing the sphere velocity to be measured from these images as well as the velocity field in the fluid. The instantaneous sphere velocity was obtained at many points along the transient. These sphere velocity measurements were used to build a velocity history in each case. The $h/d = 6.0$ case was compared to the equation of motion given by Chang *et al.* [1998]. It was found that the equation of motion was able to predict the velocity of the sphere very well for the 80%wt glycerol case, however in the 100%wt case the equation consistently overpredicted the velocity of the sphere probably due to a small wall effect which remains at very low Reynolds number even for the relatively large wall spacing of $h/d = 6.0$. Also, the equation of motion uses the properties of the fluid and of the sphere to predict the sphere velocity. The equation is highly sensitive to uncertainty in these measured quantities. Due to the uncertainty in the measurement of the fluid and sphere properties, the equation of motion could not be experimentally verified in the 100%wt glycerol case.

3. A simple empirical equation was fit to the velocity history data in each case. It was found that this simple equation gave excellent agreement to the measured velocity history of the solid sphere in both the infinite fluid case, and cases where the walls affect the flow.

This equation represents a specific solution to the equation of motion, and the three parameters for the curve fit are related to the properties of the fluid and the sphere, as well as the wall spacing. Since the equation of motion is very difficult to solve, a simple empirical formula would be very beneficial. However, to be useful, the specific connection between the fluid properties, sphere properties, wall spacing and the curve fitting parameters needs to be established.

4. The terminal velocity of the sphere is reduced as the wall spacing decreases.

A comparison of the terminal velocities reached for different wall spacings led to a suggestion that the quasi-steady drag force term in the equation of motion be modified by a wall correction term. While the magnitude of the wall correction term was evaluated for the three wall spacings examined in each case, the precise form of the wall correction function was not determined. It is possible that the wall correction term is a function of the wall spacing alone, but with only three data points for each fluid, this could not be verified. If the correct form of the wall correction function for the quasi-steady drag force is to be obtained, it is recommended that the terminal velocity be examined for many more wall spacings. While the correction to the quasi-steady drag term made the predicted terminal velocity asymptotically match the observed terminal velocity in each case, this correction does not indicate how the transient forces are changed in the presence of walls. Because the history force arises due to the diffusion of vorticity away from the surface of the accelerating sphere, it will likely be altered by the presence of walls, which tend to block this diffusion. It is less clear how, or even if, the added mass force will change in the presence of constraining walls. Magnaudet [1995] and Legendre [1996] suggest that the added mass coefficient for a sphere is 0.5 regardless of the flow parameters, however they were investigating unbounded flows. A more complete understanding of the full three-dimensional velocity field is needed to determine if the presence of walls does indeed change the added mass coefficient, and to determine how the history force changes with wall proximity.

5. In the unbounded cases, the PIV images provide a velocity field that represents a slice through an axisymmetric, three-dimensional velocity field. In the unbounded cases, each slice in the azimuthal coordinate will be the same. The motion of the sphere induces the quiescent fluid to move in a vortex structure as it moves from the leading edge of the sphere, around its equator, and then around to

the trailing edge. The centre of rotation of this vortex structure moves away from the surface of the sphere at the equator at the instant the sphere is released. The centre of rotation moves quickly away from the sphere surface due to fluid viscosity, and trails the sphere in a fashion that is dependent upon the Reynolds number.

As the wall spacing decreases, the vortex structure is squeezed between the surface of the sphere and the wall. This constriction leads to high shear stresses at the wall as well as at the surface of the sphere. Since the motion of the fluid is constrained in this plane, more mass moves around the sphere in the other azimuthal directions, meaning the flow loses its axisymmetry. There is a critical wall spacing which terminates the vortex structure between the wall and the sphere altogether. Below this critical value, all of the fluid in the gap moves in the same direction as the sphere, while the fluid circulates around the sphere in the other azimuthal directions. This critical wall separation was between h/d = 1.2 and 1.5 for the 80%wt glycerol case, and between h/d = 1.5 and 6.0 for the 100%wt glycerol case. Due to the limited number of wall spacings examined, the exact wall spacing where the vortex is eliminated in the gap could not be established. There is clearly an effect of both the fluid properties and the wall spacing on the elimination of the vortex in the gap. This is an interesting topic, and should be investigated further with more wall spacings examined.

6. The shear stress distribution at the wall reaches a maximum at the point where the equator of the sphere passes. The peak of the shear stress distribution increases in magnitude as the sphere approaches terminal velocity. The maximum shear stress at the wall was determined to be approximately 4 Pa, when the sphere was at a position of Y/d = 3.15 along the transient in the 80%wt glycerol case. The distribution of the shear stresses along the wall was determined by examining the slope of the velocity profile near the wall. Due to the small velocities near the wall, the shear stress distribution for the 100%wt glycerol case was too noisy to obtain meaningful data.

The vortex structure observed between the wall and the sphere caused the velocities near the wall to be in the opposite direction than the velocity of the sphere for the 80%wt glycerol case. Outside of the vortex structure, the velocities near the wall are in the same direction as the sphere. This reversal of direction means that there are stagnation points at the wall where the shear stress reverses direction. It was observed that these stagnation points are established very early in the transient and their location remains consistent with respect to the sphere throughout the transient.

7. The shear stress at the surface of the sphere at the equator increases throughout the transient as it approaches an asymptotic value at the terminal velocity. The proximity of the walls tends to increase the shear stress at the equator of the sphere. For the 80%wt glycerol case, the shear stress at the equator of the sphere approaches 8, 6, and 4 Pa for the h/d = 1.2, 1.5 and 6.0 cases, respectively. The 100%wt case shows more uncertainty in the measurement of the shear stress, however it can be seen that the proximity of the walls tends to increase the shear stress in this case as well. Also, it is shown that the transient occurs very quickly for the 100%wt glycerol case, and the sphere attains terminal velocity at or before Y/d = 0.105 for every wall spacing. The terminal shear stresses at the equator for the 100%wt glycerol case are approximately 6.5, 5, and 4 Pa for the h/d = 1.2, 1.5 and 6.0 cases respectively.

It must be noted that these measurements represent the shear stress at only one point on the sphere. The measurements were made at the equator of the sphere at the location that is normal to the plane walls. The shear stress will vary for other locations on the sphere surface. A complete examination of the state of shear stress at the surface of the sphere would require the full three-dimensional velocity field.

Recommendations for Future Work

It is recommended that a numerical study of the flow around an accelerating sphere be undertaken. This will allow the three-dimensional velocity field to be established and many features of the flow to be elucidated. Specifically, the three-dimensional flow field will allow an evaluation of the added mass coefficient for an accelerating sphere. The effects of constraining walls on the added mass coefficient could then be properly established.

The data set obtained in the current study will be a useful experimental verification of the results obtained from any numerical study. Of particular interest would be the distribution of shear stress at the surface of the sphere, and how the magnitude and distribution of the shear stresses change throughout the transient with and without the presence of walls. As well, the three-dimensional velocity field would shed light on how the distribution of momentum around the sphere changes as the wall spacing narrows. The current study has shown that the vortex structure between the sphere and the walls is squeezed and then eliminated as the walls approach the sphere, thus more mass of fluid moves around the sphere in directions other than through the gap. A numerical study would show what is happening in the rest of the fluid, and perhaps lead to a connection between the wall spacing, fluid properties and the suppression of the vortex in the gap between the sphere and the wall.

References

Anderson, J. D. Jr., Fundamentals of Aerodynamics (3rd Edition), McGraw-Hill, Inc., New York, 2001.

Chang, T. J., Yen, B. C., "Gravitational Fall Velocity of Sphere in Viscous Fluid", *Journal of Engineering Mechanics*, Vol. 124, No. 11, pp. 1193-1199, November 1998.

Clift, R., Grace, J. R., Weber, M. E., Bubbles, Drops, and Particles, Academic Press, New York, 1978.

Delvin, K., The Millenium Problems, 2003, Basic Books, New York, p. 133.

Glycerin Producers Association, Physical Properties of Glycerin and its Solutions; 295 Madison Ave, New York 17, N.Y. USA, 1963.

Happel, J., and Brenner, H., Low Reynolds Number Hydrodynamics, Noordhoff International Publishing, Netherlands, 1973.

Magnaudet, J.J.M., "The Forces Acting on Bubbles and Rigid Particles", Fluids Engineering Division Summer Meeting, Vancouver, Canada, ASME, June 22 – 26, 1997.

Mei, R. & Adrian, R.J., "Flow Past a Sphere with an Oscillation in the Free-Stream Velocity and Unsteady Drag at Finite Reynolds Number," *Journal of Fluid Mechanics*, Vol. 237, pp. 323-341, 1992.

Mei, R., Lawrence, C.J., and Adrian, R.J., "Unsteady Drag on a Sphere at Finite Reynolds Number with Small Fluctuations in the Free-Stream Velocity", *Journal of Fluid Mechanics*, Vol. 233, pp. 613-631, 1991.

Miyamura, A., Iwasaki, S., and Ishii, T., "Experimental Wall Correction Factors of Single Solid Spheres in Triangular and Square Cylinders, and Parallel Plates", *International Journal of Multiphase Flow*, Vol. 7, pp. 46-47, 1980.

Popham, A. E., The Drawings of Leonardo da Vinci, Reynal & Hitchcock, New York, 1945, p. 281.

Prandtl, L., and Tietjens, O. G., Applied Hydro- and Aeromechanics, United Engineering Trustees, Inc., New York, 1934, pp. 295 and 302: also, Dover Publications, Inc., New York, 1957.

Proudman, I. and Pearson, J. R. A., "Expansion at small Reynolds numbers for the flow past a sphere and a circular cylinder", *Journal of Fluid Mechanics*, v2, pp. 237-262, 1957.

Raffel, M., Willert, C. E., Kompenhans, J., Particle Image Velocimetry – A Practical Guide, Springer, New York, 1998.

Schlichting, H., Boundary Layer Theory (7th edition), McGraw-Hill Book Company, New York, 1979.

Shapira, M., and Haber, S., "Low Reynolds Number Motion of a Droplet Between Two Parallel Plates", *Int. J. of Multiphase Flow*, Vol. 14, No. 4, pp. 483-506, 1988.

Van Dyke, M., An Album of Fluid Motion, Parabolic Press, Stanford, 1982.

Wakiya, S., "Effect of a Submerged Object on a Slow Viscous Flow: Influence of a Plane Wall on the Unsteady Motion of a Sphere", *Res. Rep. Fac. Eng. Niigata Univ. (Japan)*, Vol. 10, pp.15-24, 1961.

Appendix A.
Mean Velocity Field Results around Falling Solid Sphere

This appendix contains the results of Particle Image Velocimetry (PIV) measurements made around a solid sphere accelerating from rest to terminal velocity between two parallel plane walls.

The ratio of wall spacing to sphere diameter (*h/d*) was varied to determine the effect of wall proximity on the motion of the fluid around the sphere. A wide wall spacing of $h/d = 6.0$ was used to mimic an infinite fluid. The wall spacings of $h/d = 1.5$ and $h/d = 1.2$ were used to show the effects of closer wall proximities.

For each of these wall spacings, a series of PIV images was obtained to build a velocity history of the accelerating sphere. The ratio of distance from release to sphere diameter is given as *Y/d*. Using a triggering laser, PIV images could be obtained at a specific *Y/d* location with high repeatability. Using this feature, the PIV data could be averaged from a number of individual images taken at the same *Y/d* location. Each PIV image presented in this appendix is an ensemble average of the data from ten separate drop sequences taken at that location. The PIV images were taken at locations of $Y/d =$ 0.105, 0.262, 0.524, 1.05, and 3.15. These give a representative picture of the flow around the sphere as it develops during the transient.

The test fluids were solutions of glycerol and water. The two cases examined were 100%wt glycerol, and 80%wt glycerol. A summary of the test conditions for each PIV image presented in this appendix is given in Table A1.

Each of the figures in this appendix is presented in the same format. The origin of the coordinate system is located at the centre of the sphere, and the coordinate aces are normalised with the sphere radius. All of the velocity vectors are normalised with the instantaneous sphere velocity, which is given in a key as a numerical value and reference vector. Also appearing in the key for each image are the weight percent glycerol, the normalised wall spacing (*h/d*), the instantaneous Reynolds number (*Re*), the normalised distance the sphere has fallen from the release point (*Y/d*), and the fraction of the terminal velocity (U_p/U_T) that the sphere has obtained. The flow around the sphere is symmetrical about the plane through the centre of the sphere that is parallel to the walls. The left side of the plane of symmetry shows the velocity relative to an observer in the fluid as the sphere moves past. The right side of the plane of symmetry shows velocities relative to the sphere

Table A1: Test conditions for PIV images presented in Appendix A.

Page	%wt Glycerol	*h/d*	*Re*	*Y/d*	U_p/U_T [%]	U_p [mm/s]
97	100	6.0	0.318	0.105	67.3	13.4
98	100	6.0	0.362	0.262	76.6	15.3
99	100	6.0	0.407	0.524	86.1	17.2
100	100	6.0	0.444	1.05	94	18.7
101	100	6.0	0.452	3.15	95.7	19.1
102	100	1.5	0.218	0.105	84.8	8.75
103	100	1.5	0.253	0.262	98.6	10.2
104	100	1.5	0.236	0.524	92	9.50
105	100	1.5	0.236	1.05	91.8	9.48
106	100	1.5	0.254	3.15	99.1	10.2
107	100	1.2	0.193	0.105	86.5	7.58
108	100	1.2	0.195	0.262	57.6	7.68
109	100	1.2	0.197	0.524	88.5	7.75
110	100	1.2	0.201	1.05	90.1	7.90
111	100	1.2	0.211	3.15	94.5	8.28
112	80	6.0	19.4	0.105	23.7	48.0
113	80	6.0	30.8	0.262	37.6	76.0

114	80	6.0	36.8	0.524	45.0	90.8
115	80	6.0	50.6	1.05	61.8	124.8
116	80	6.0	64.8	3.15	79.1	160.0
117	80	1.5	22.1	0.105	27.4	53.0
118	80	1.5	29.8	0.262	36.8	71.2
119	80	1.5	37.0	0.524	45.8	88.5
120	80	1.5	48.0	1.05	59.4	114.8
121	80	1.5	60.0	3.15	74.2	143.0
122	80	1.2	15.1	0.105	21.8	35.5
123	80	1.2	25.6	0.262	36.9	60.1
124	80	1.2	35.3	0.524	50.8	82.8
125	80	1.2	45.5	1.05	65.6	106.9
126	80	1.2	57.1	3.15	82.3	134.0

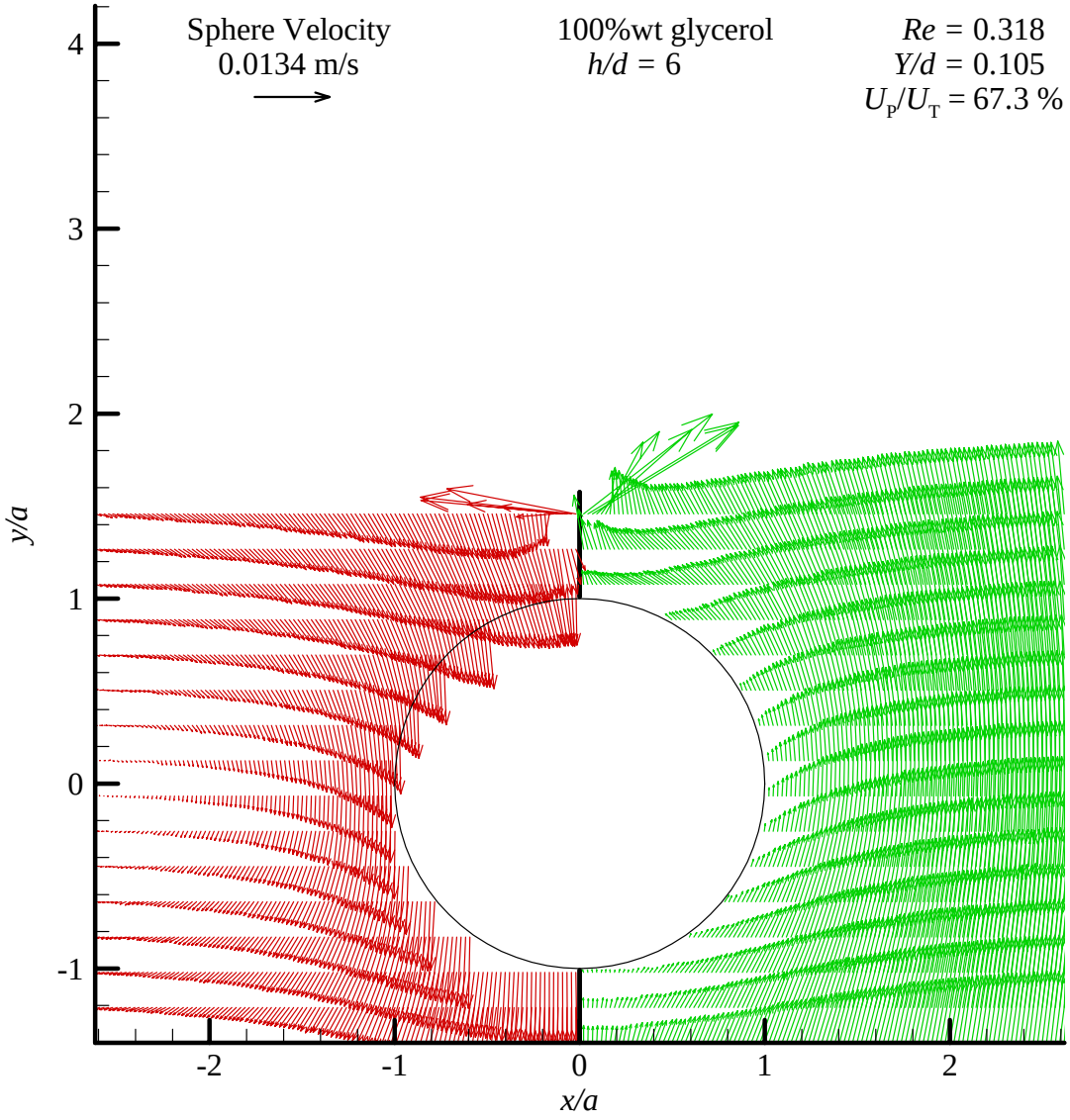

Figure A-1: Velocity field around a falling solid sphere. The left side shows velocities with respect to the moving sphere while the right is with respect to a stationary sphere. 100%wt glycerol, h/d=6.0, Y/d=0.105, U_P=13.4 mm/s, Re=0.318, U_P/U_T=67.3%. Every eighth row of vectors is shown.

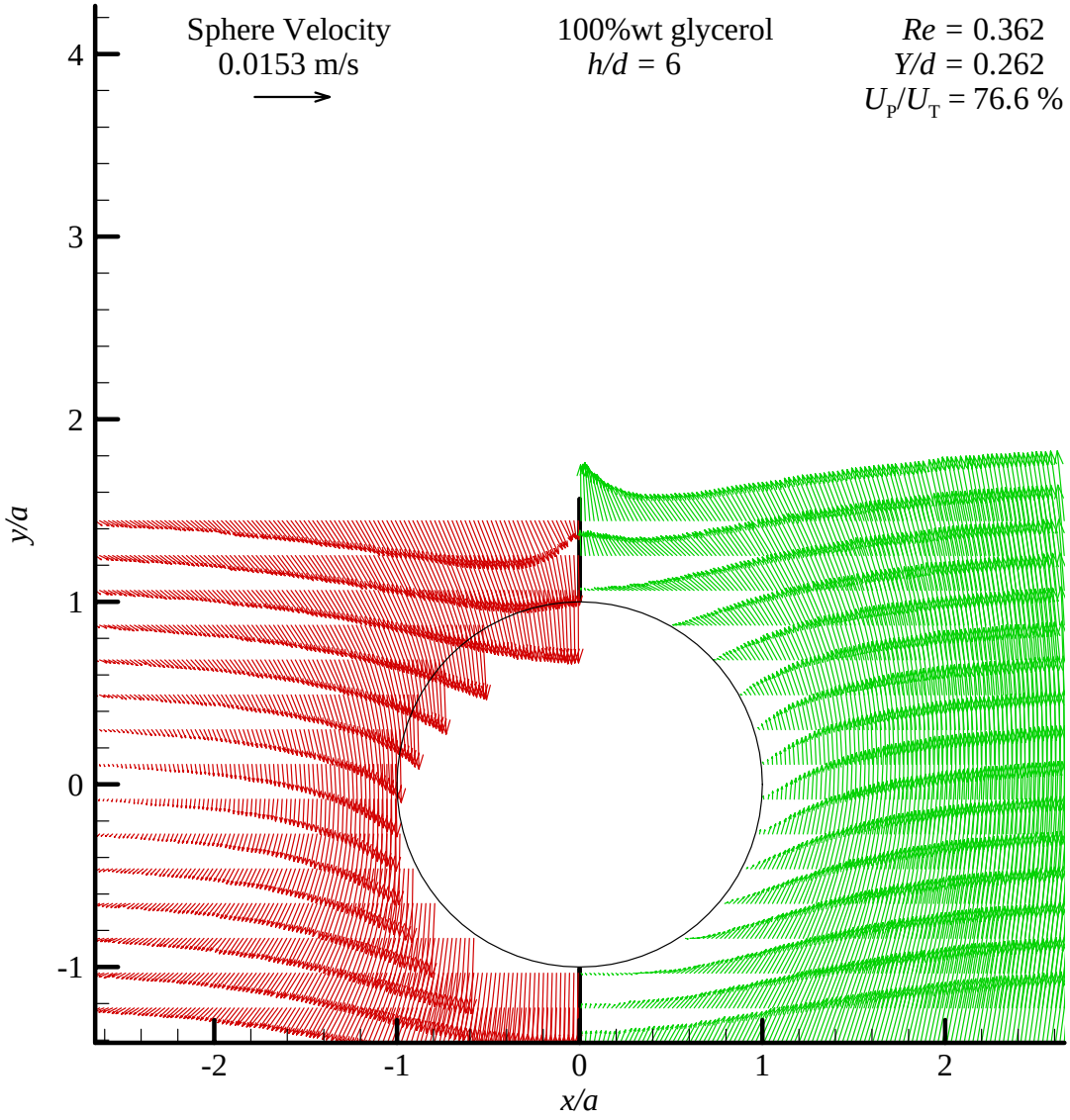

Figure A-2: Velocity field around a falling solid sphere. The left side shows velocities with respect to the moving sphere while the right is with respect to a stationary sphere. 100%wt glycerol, h/d=6.0, Y/d=0.262, U_P=15.3 mm/s, Re=0.362, U_P/U_T=76.6%. Every eighth row of vectors is shown.

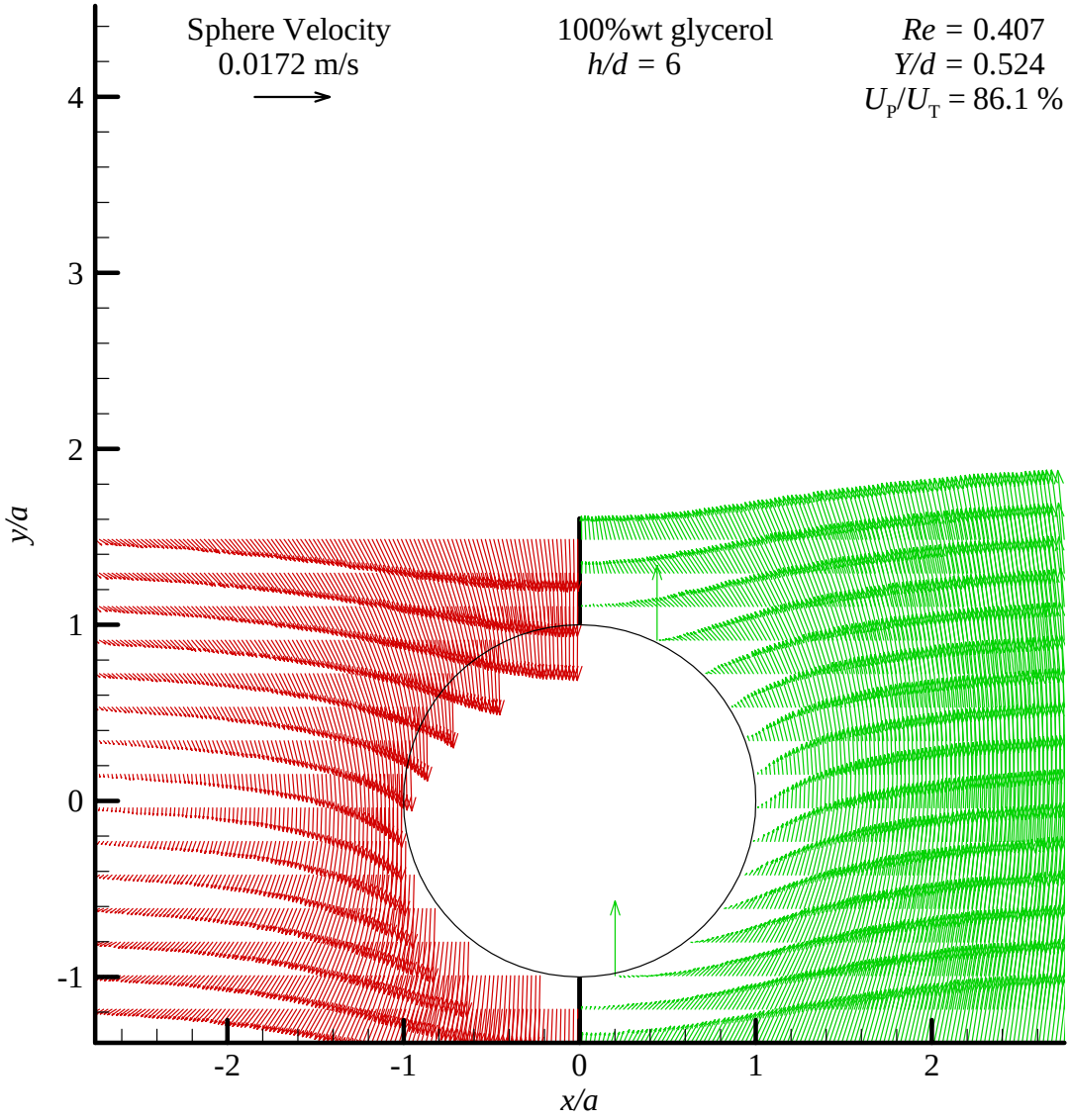

Figure A-3: Velocity field around a falling solid sphere. The left side shows velocities with respect to the moving sphere while the right is with respect to a stationary sphere. 100%wt glycerol, h/d=6.0, Y/d=0.524, U_P=17.2 mm/s, Re=0.407, U_P/U_T=86.1%. Every eighth row of vectors is shown.

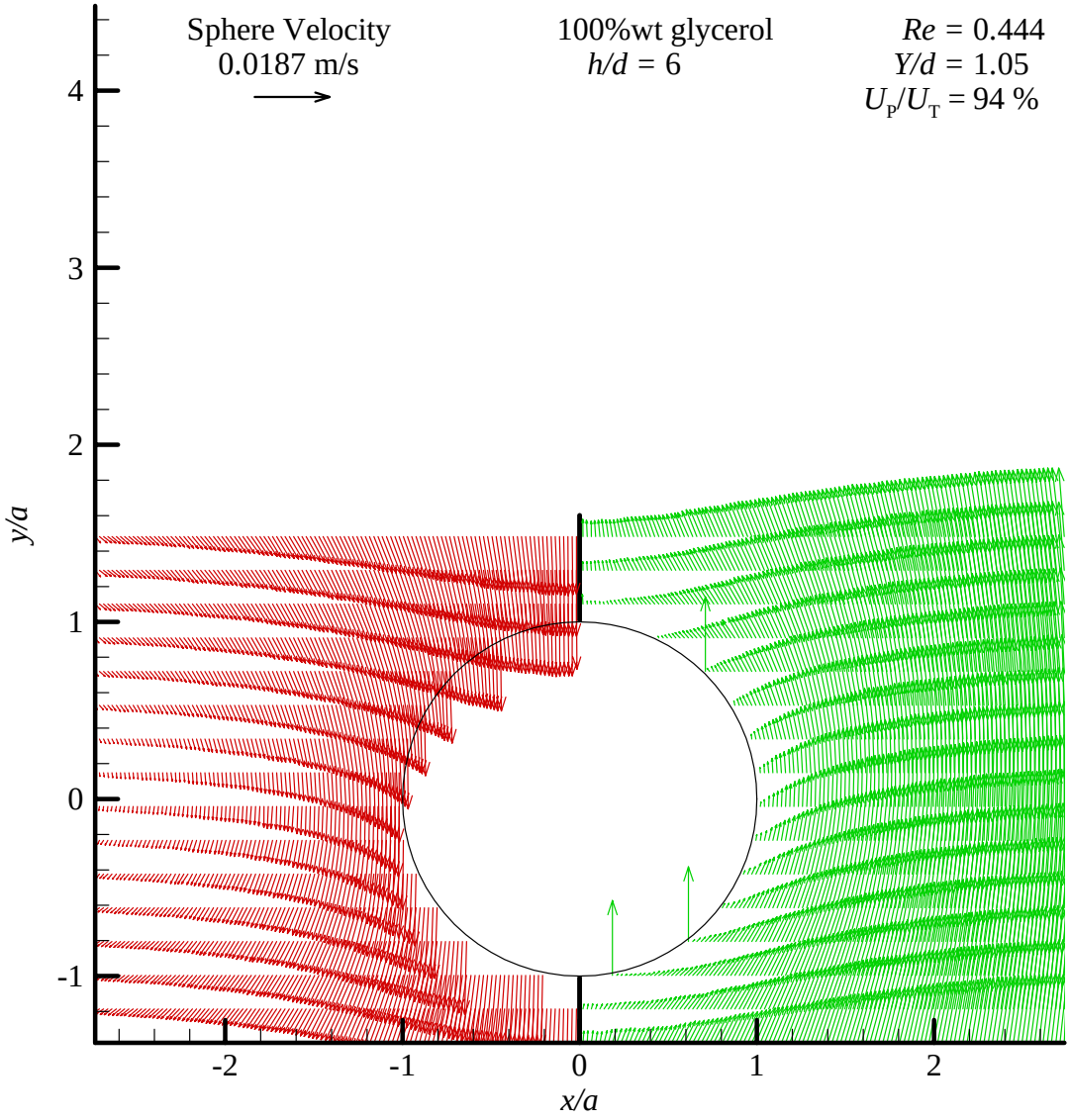

Figure A-4: Velocity field around a falling solid sphere. The left side shows velocities with respect to the moving sphere while the right is with respect to a stationary sphere. 100%wt glycerol, h/d=6.0, Y/d=1.05, U_P=18.7 mm/s, Re=0.444, U_P/U_T=94%. Every eighth row of vectors is shown.

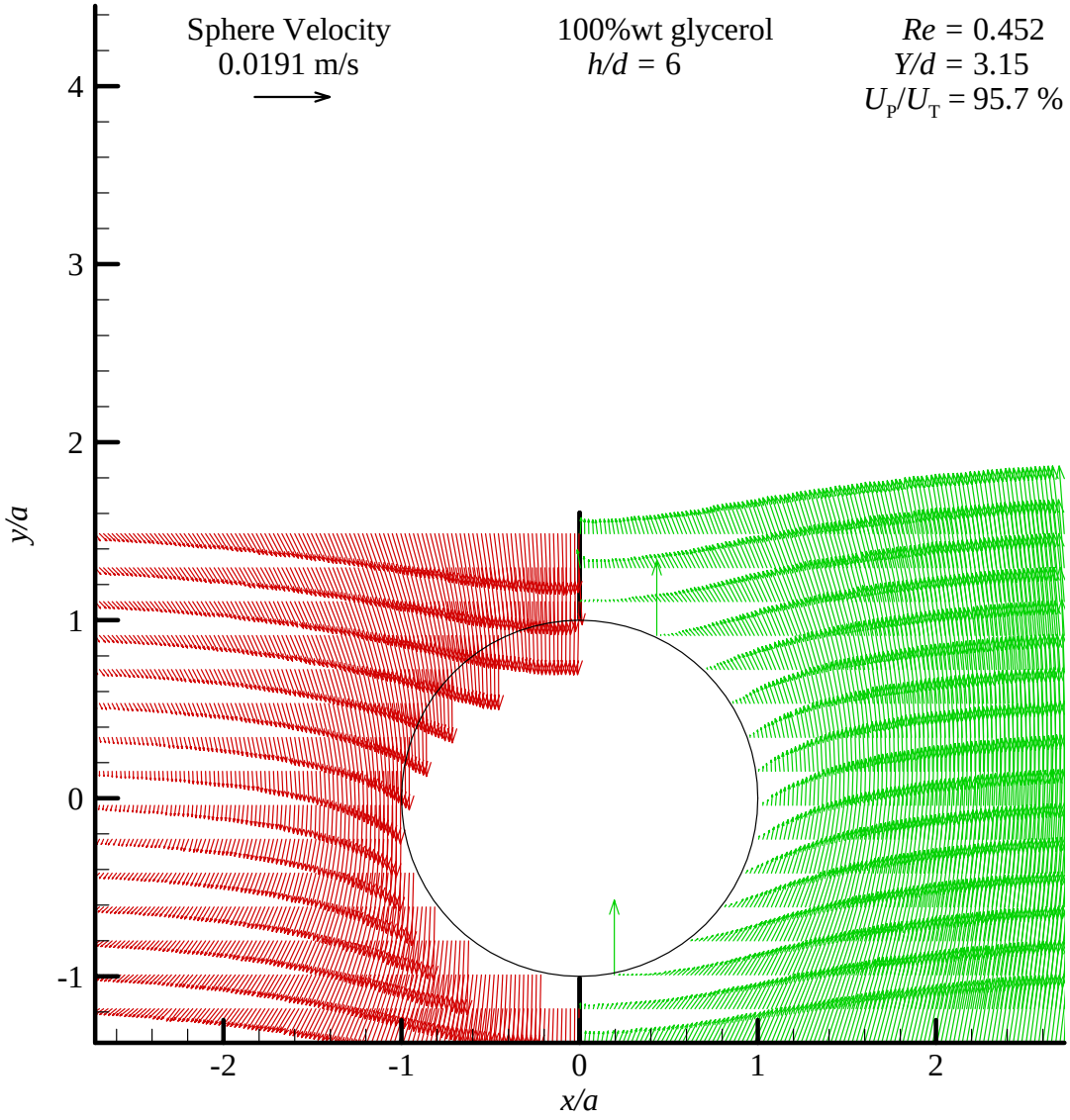

Figure A-5: Velocity field around a falling solid sphere. The left side shows velocities with respect to the moving sphere while the right is with respect to a stationary sphere. 100%wt glycerol, h/d=6.0, Y/d=3.15, U_P=19.1 mm/s, Re=0.452, U_P/U_T=95.7%. Every eighth row of vectors is shown.

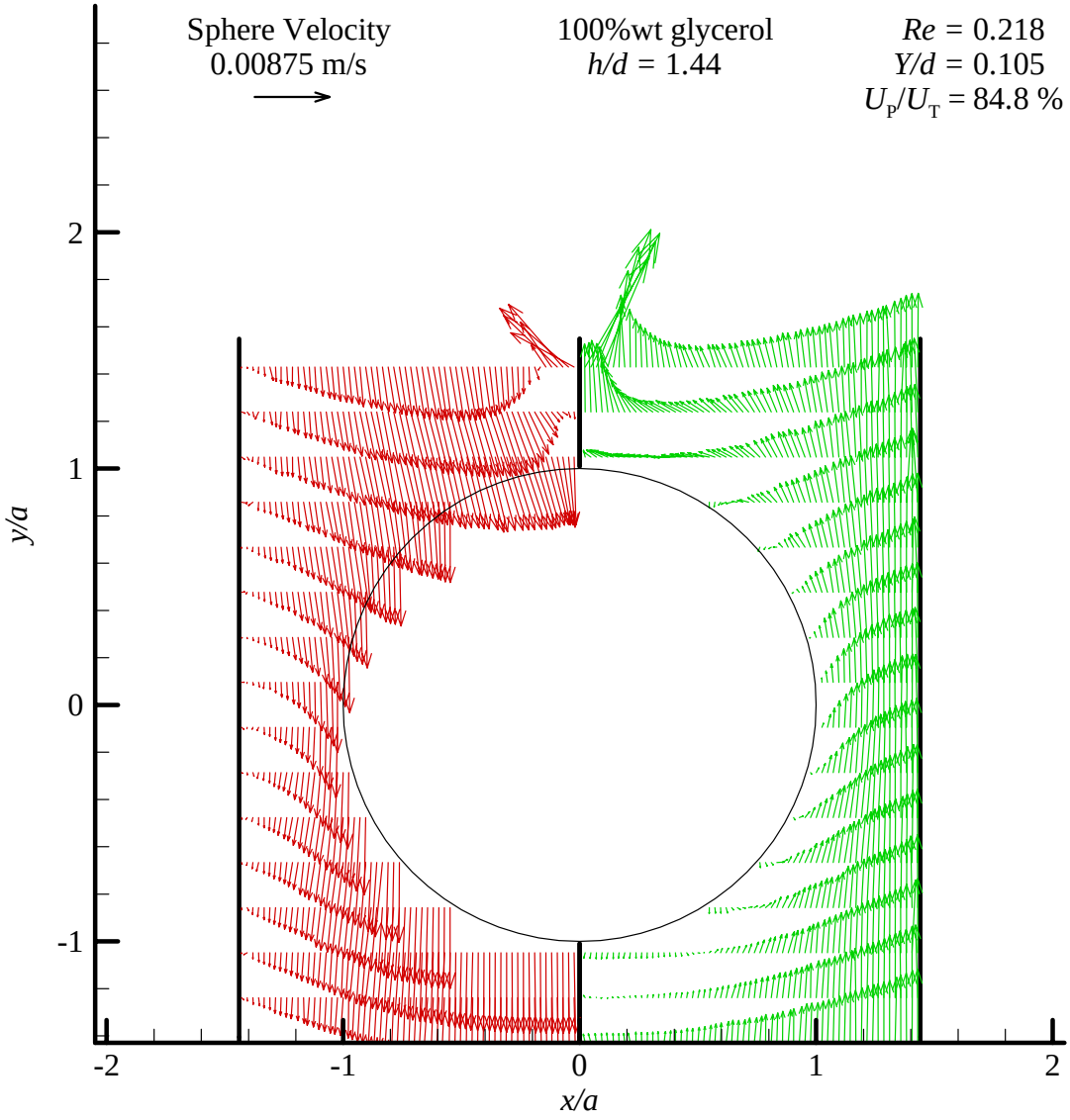

Figure A-6: Velocity field around a falling solid sphere. The left side shows velocities with respect to the moving sphere while the right is with respect to a stationary sphere. 100%wt glycerol, h/d=1.5, Y/d=0.105, U_P=8.75 mm/s, Re=0.218, U_P/U_T=84.8%. Every eighth row of vectors is shown.

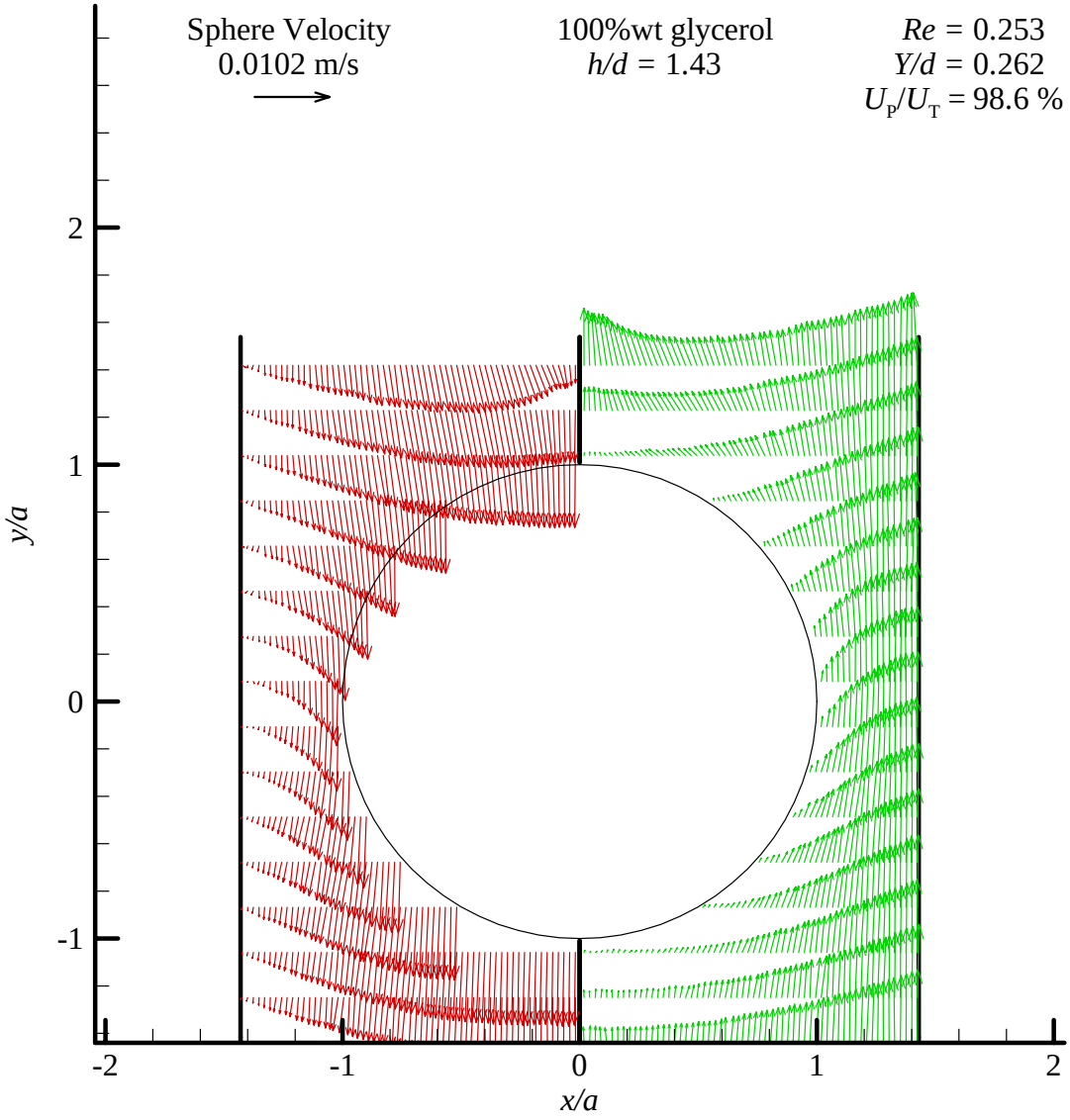

Figure A-7: Velocity field around a falling solid sphere. The left side shows velocities with respect to the moving sphere while the right is with respect to a stationary sphere. 100%wt glycerol, h/d=1.5, Y/d=0.262, U_P=10.2 mm/s, Re=0.253, U_P/U_T=98.6%. Every eighth row of vectors is shown.

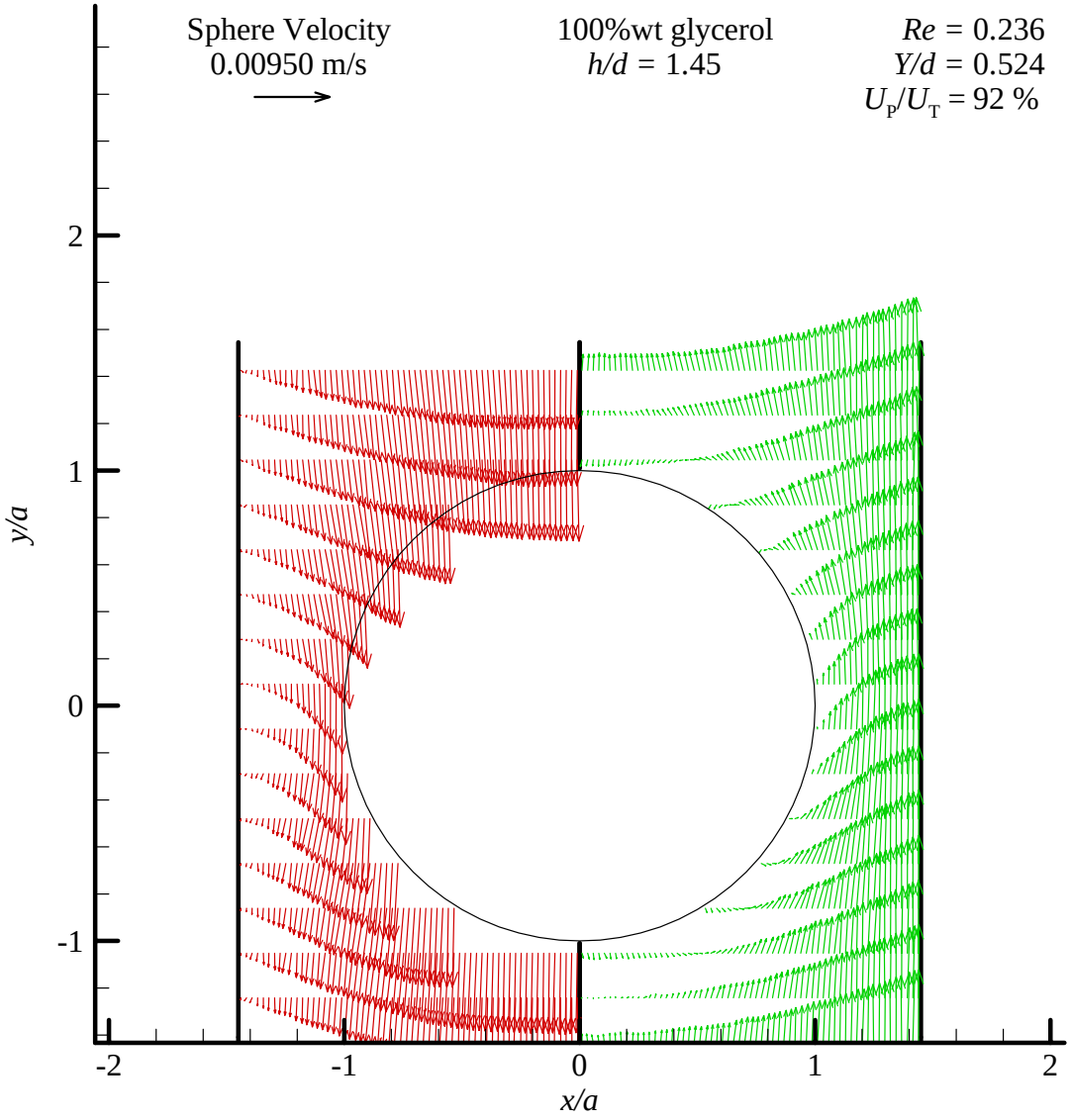

Figure A-8: Velocity field around a falling solid sphere. The left side shows velocities with respect to the moving sphere while the right is with respect to a stationary sphere. 100%wt glycerol, h/d=1.5, Y/d=0.524, U_P=9.5 mm/s, Re=0.236, U_P/U_T=92%. Every eighth row of vectors is shown.

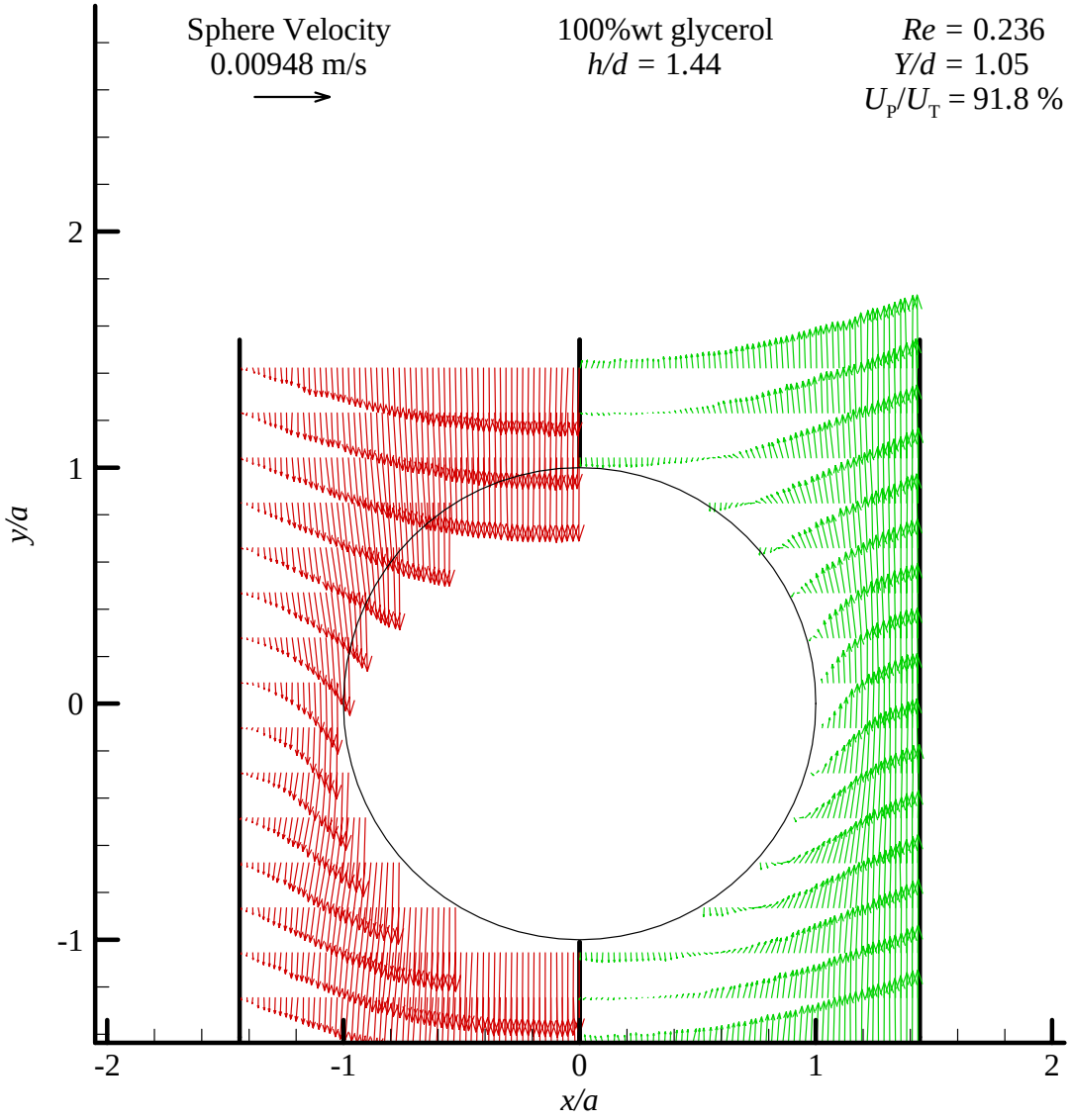

Figure A-9: Velocity field around a falling solid sphere. The left side shows velocities with respect to the moving sphere while the right is with respect to a stationary sphere. 100%wt glycerol, h/d=1.5, Y/d=1.05, U_P=9.48 mm/s, Re=0.236, U_P/U_T=91.8%. Every eighth row of vectors is shown.

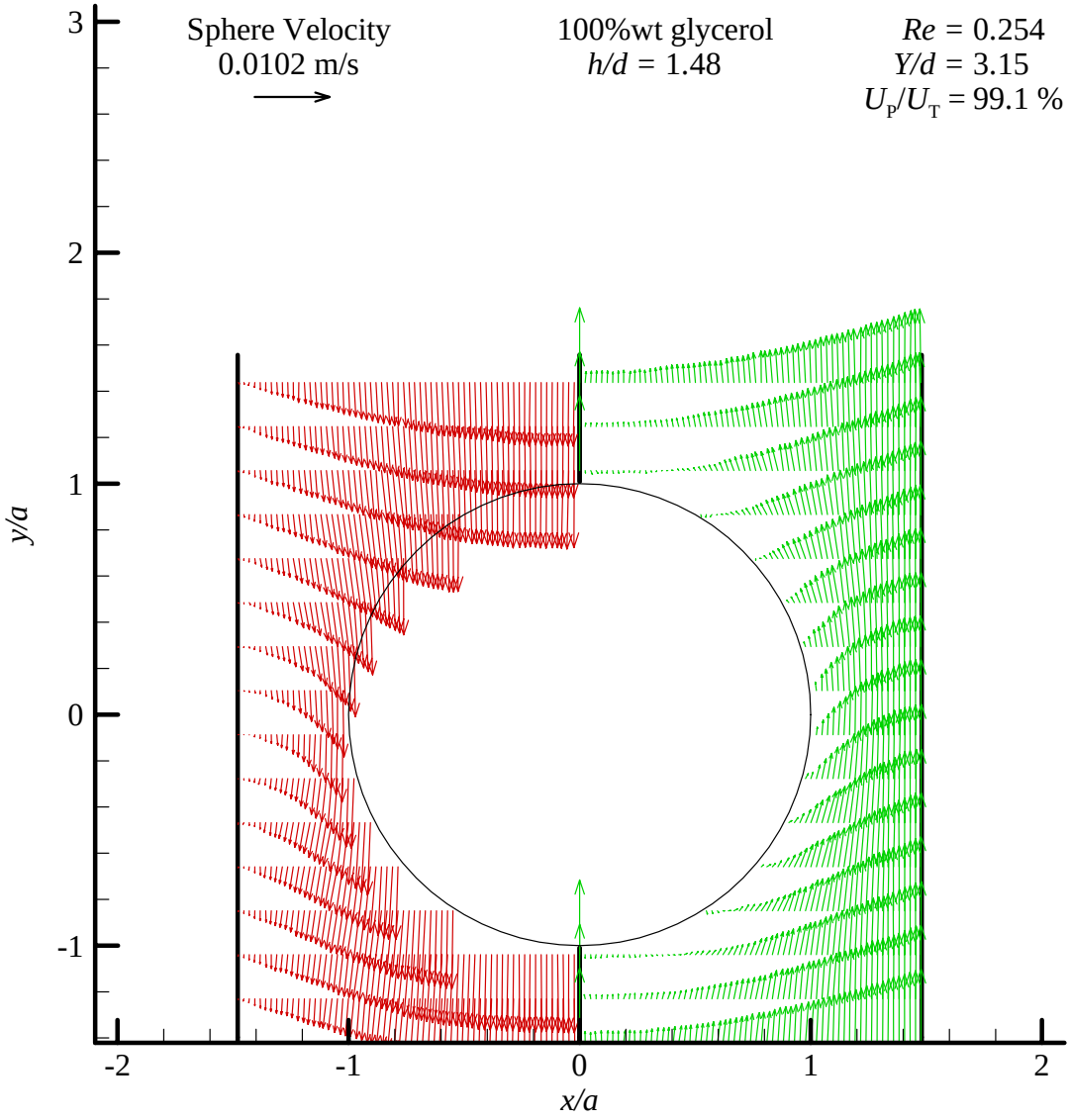

Figure A-10: Velocity field around a falling solid sphere. The left side shows velocities with respect to the moving sphere while the right is with respect to a stationary sphere. 100%wt glycerol, h/d=1.5, Y/d=3.15, U_P=10.2 mm/s, Re=0.254, U_P/U_T=99.1%. Every eighth row of vectors is shown.

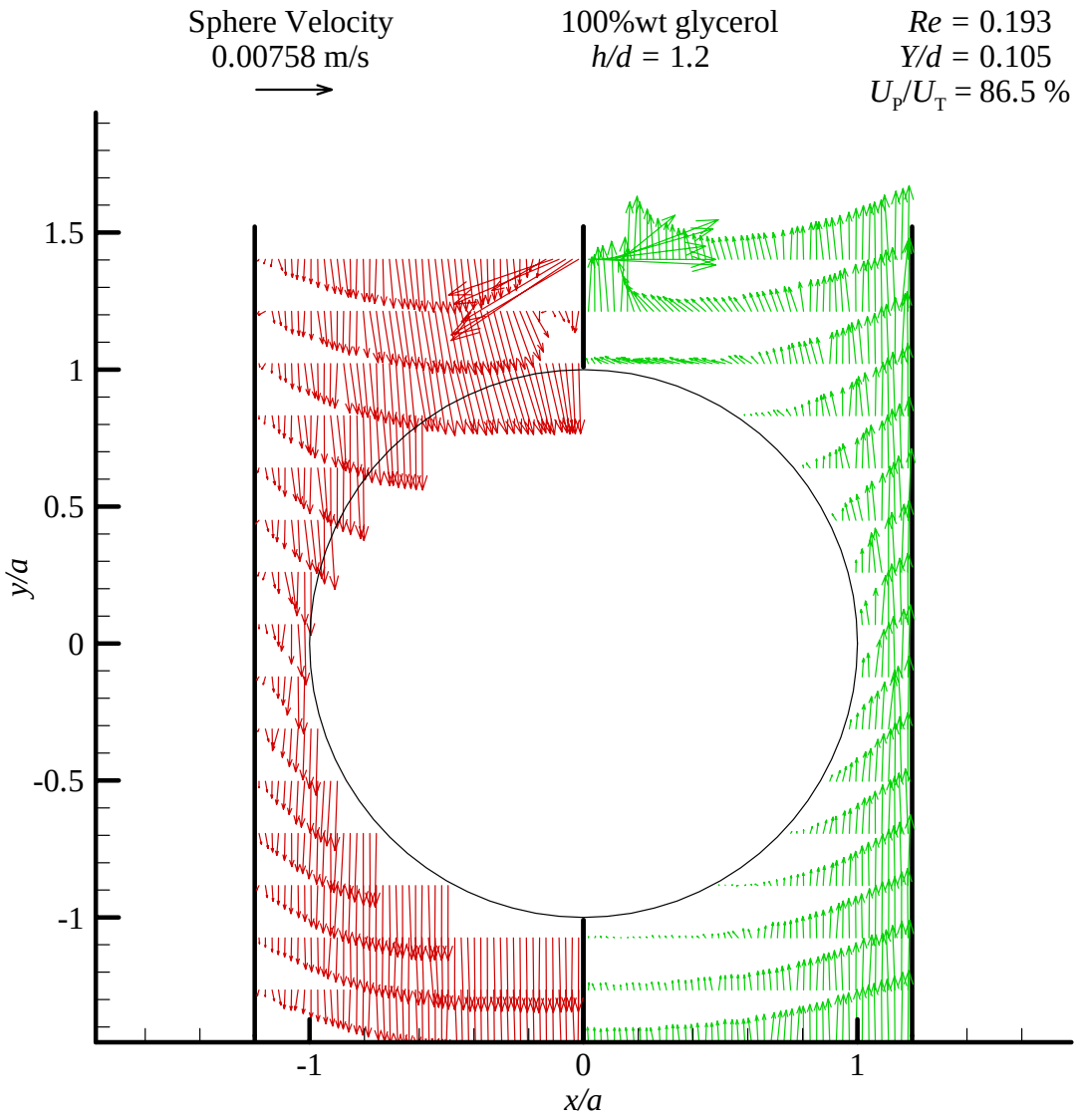

Figure A-11: Velocity field around a falling solid sphere. The left side shows velocities with respect to the moving sphere while the right is with respect to a stationary sphere. 100%wt glycerol, h/d=1.2, Y/d=0.105, U_P=7.58 mm/s, Re=0.193, U_P/U_T=86.5%. Every eighth row of vectors is shown.

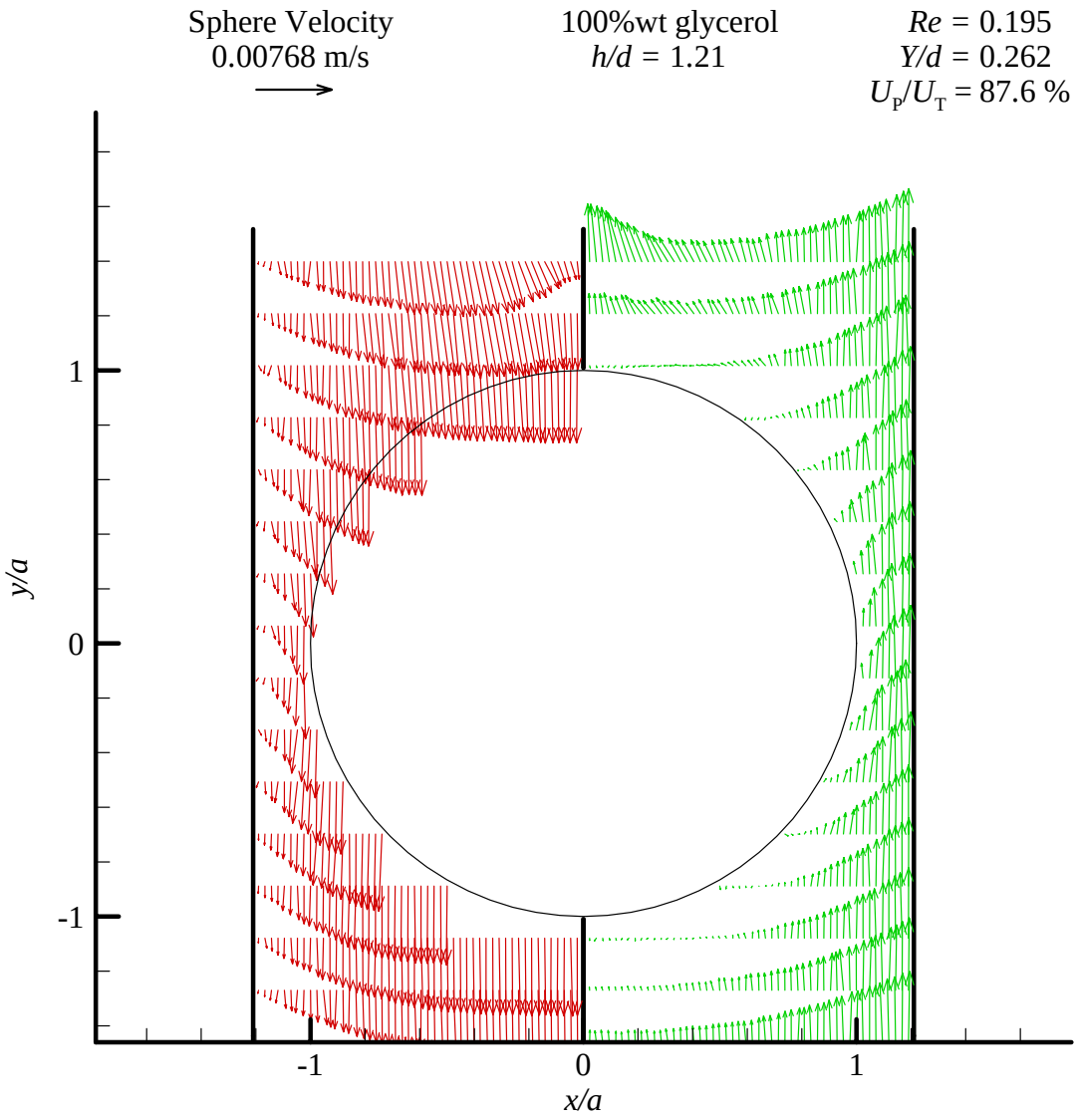

Figure A-12: Velocity field around a falling solid sphere. The left side shows velocities with respect to the moving sphere while the right is with respect to a stationary sphere. 100%wt glycerol, h/d=1.2, Y/d=0.262, U_P=7.68 mm/s, Re=0.195, U_P/U_T=87.6%. Every eighth row of vectors is shown.

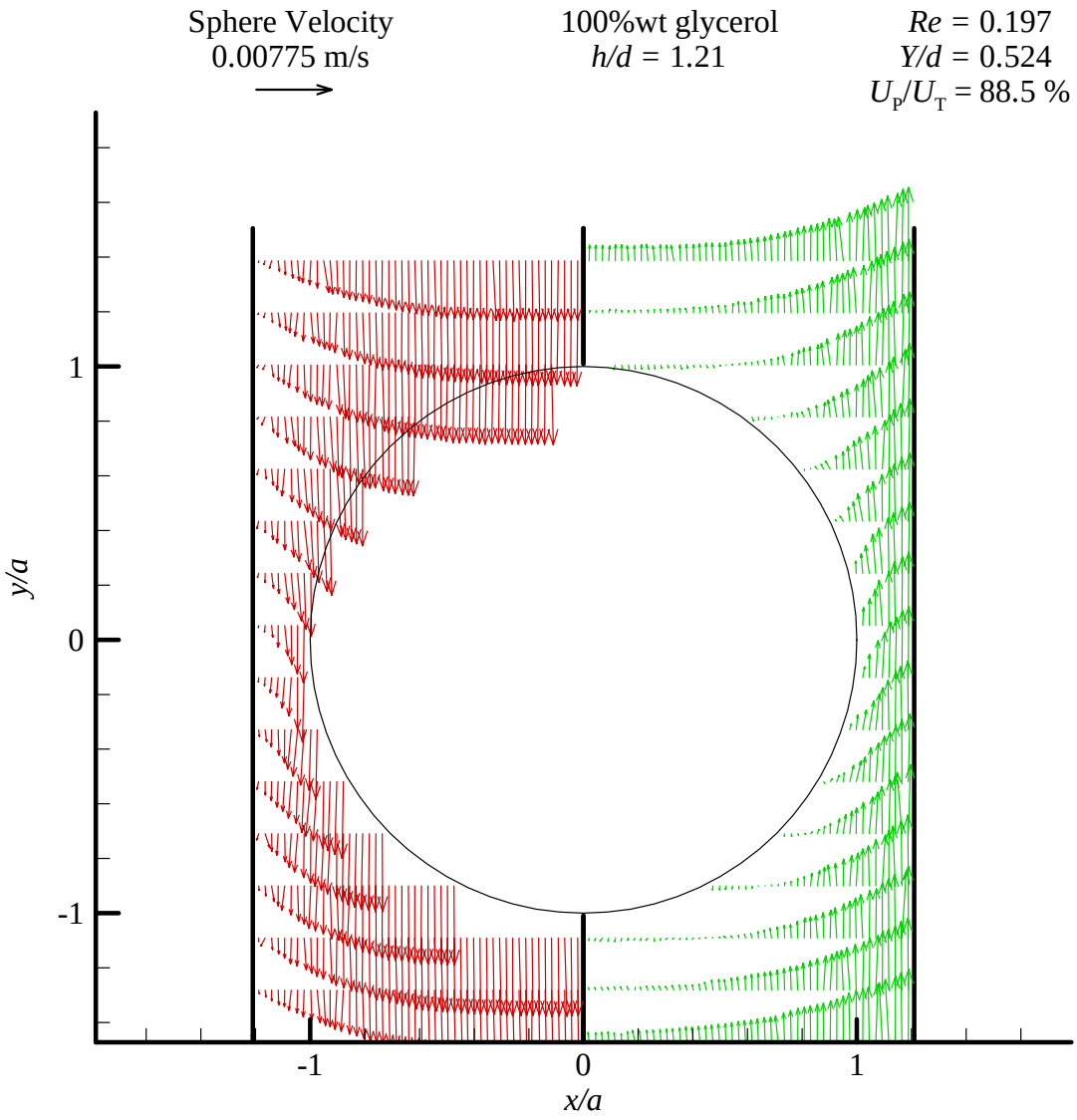

Figure A-13: Velocity field around a falling solid sphere. The left side shows velocities with respect to the moving sphere while the right is with respect to a stationary sphere. 100%wt glycerol, h/d=1.2, Y/d=0.524, U_P=7.75 mm/s, Re=0.197, U_P/U_T=88.5%. Every eighth row of vectors is shown.

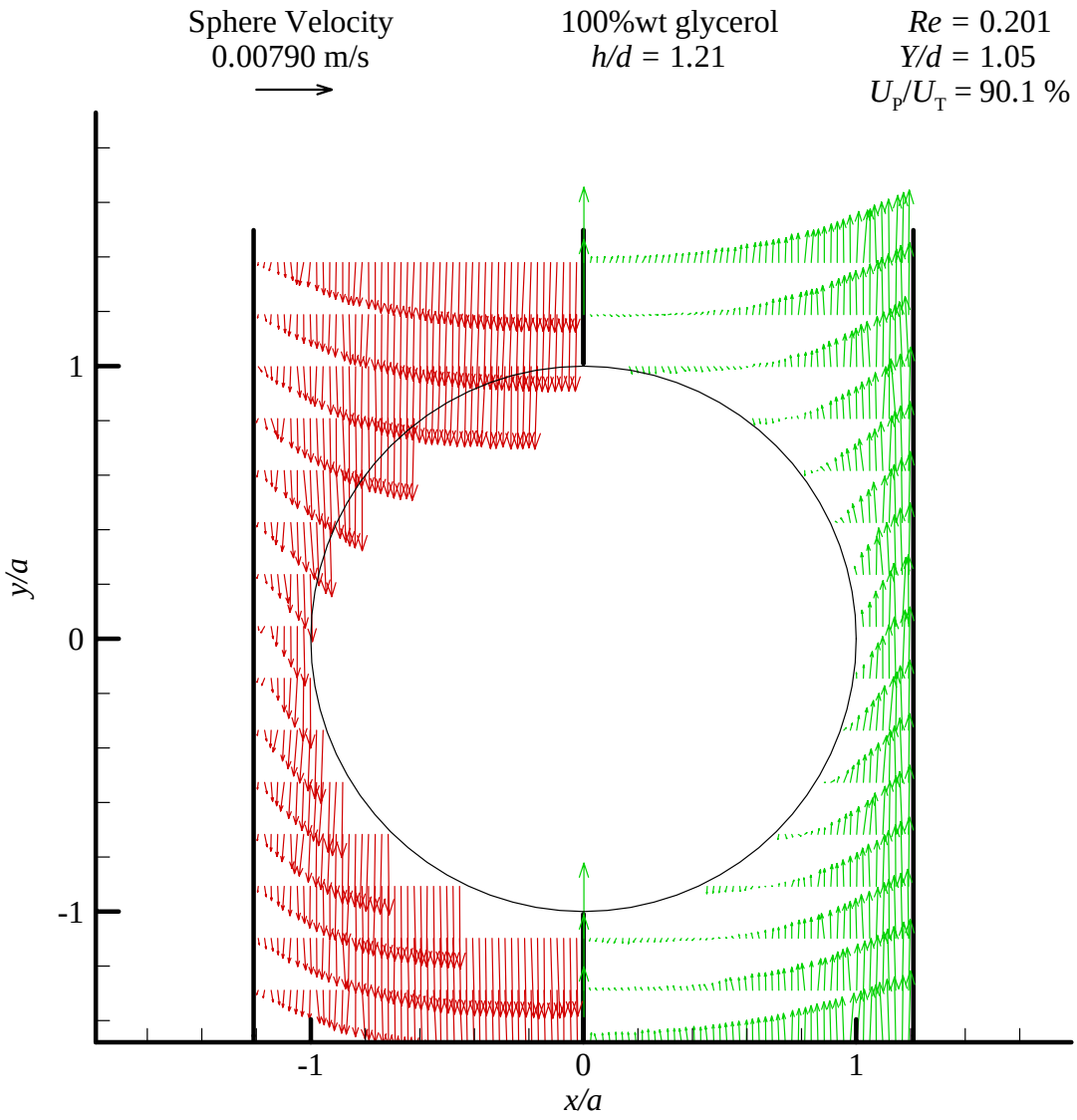

Figure A-14: Velocity field around a falling solid sphere. The left side shows velocities with respect to the moving sphere while the right is with respect to a stationary sphere. 100%wt glycerol, h/d=1.2, Y/d=1.05, U_P=7.90 mm/s, Re=0.201, U_P/U_T=90.1%. Every eighth row of vectors is shown.

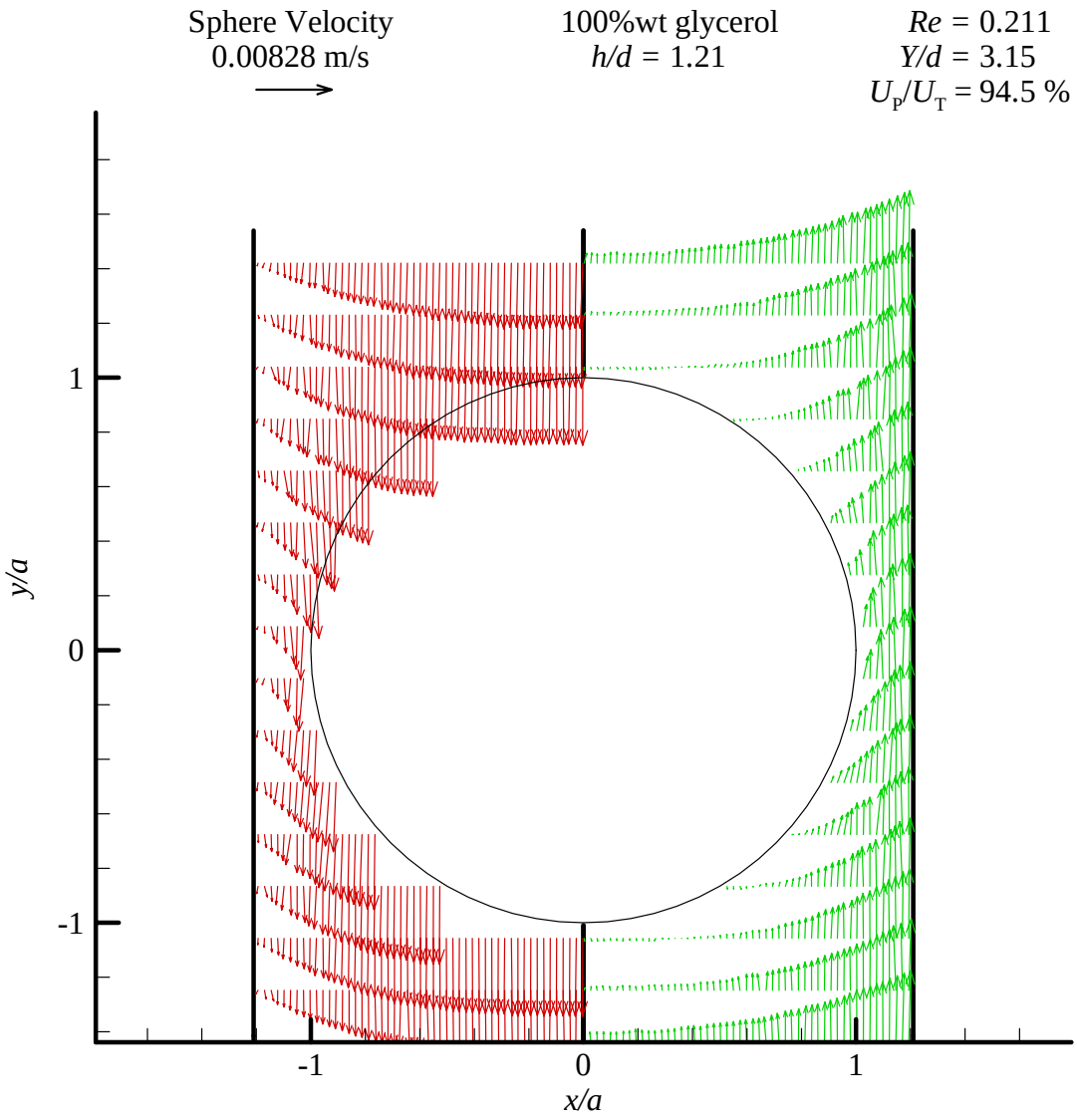

Figure A-15: Velocity field around a falling solid sphere. The left side shows velocities with respect to the moving sphere while the right is with respect to a stationary sphere. 100%wt glycerol, h/d=1.2, Y/d=3.15, U_P=8.28 mm/s, Re=0.211, U_P/U_T=94.5%. Every eighth row of vectors is shown.

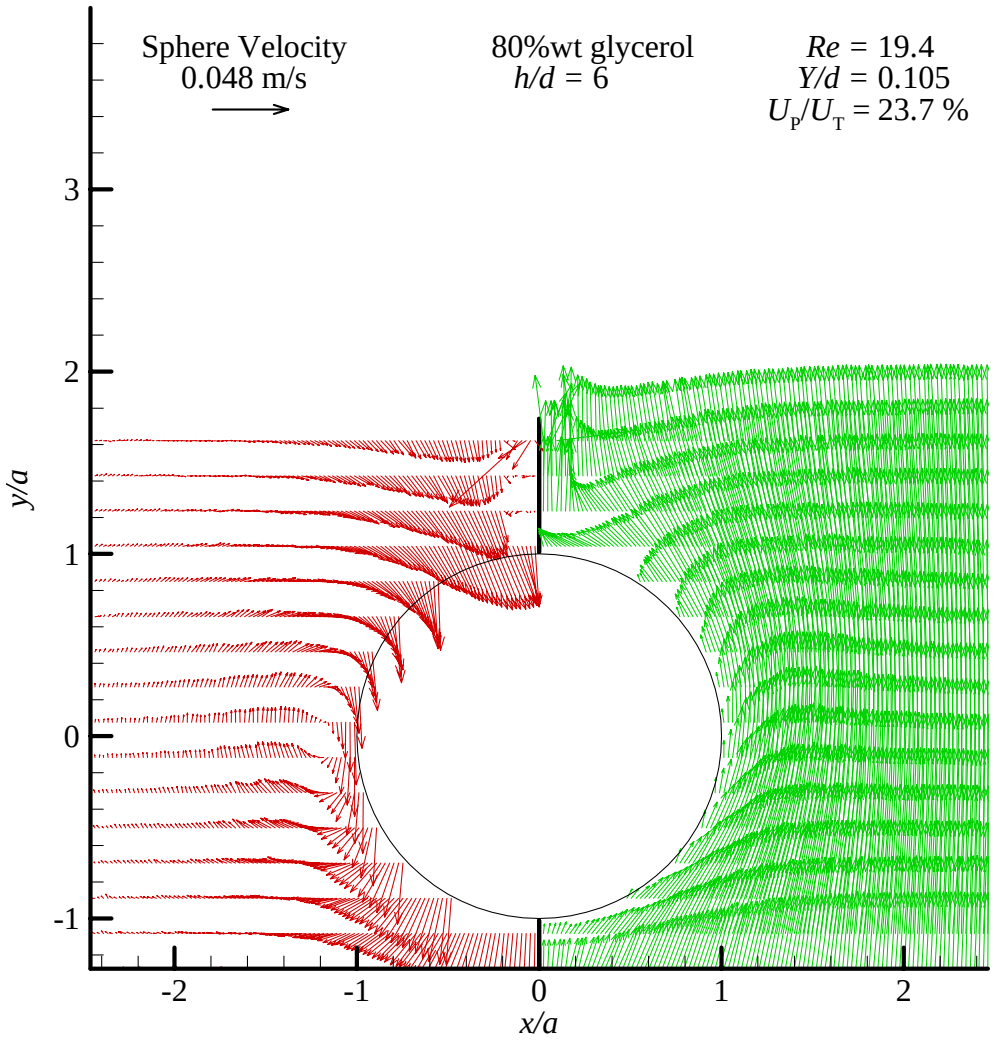

Figure A-16: Velocity field around a falling solid sphere. The left side shows velocities with respect to the moving sphere while the right is with respect to a stationary sphere. 80%wt glycerol, h/d=6.0, Y/d=0.105, U_P=48 mm/s, Re=19.4, U_P/U_T=23.7%. Every eighth row of vectors is shown.

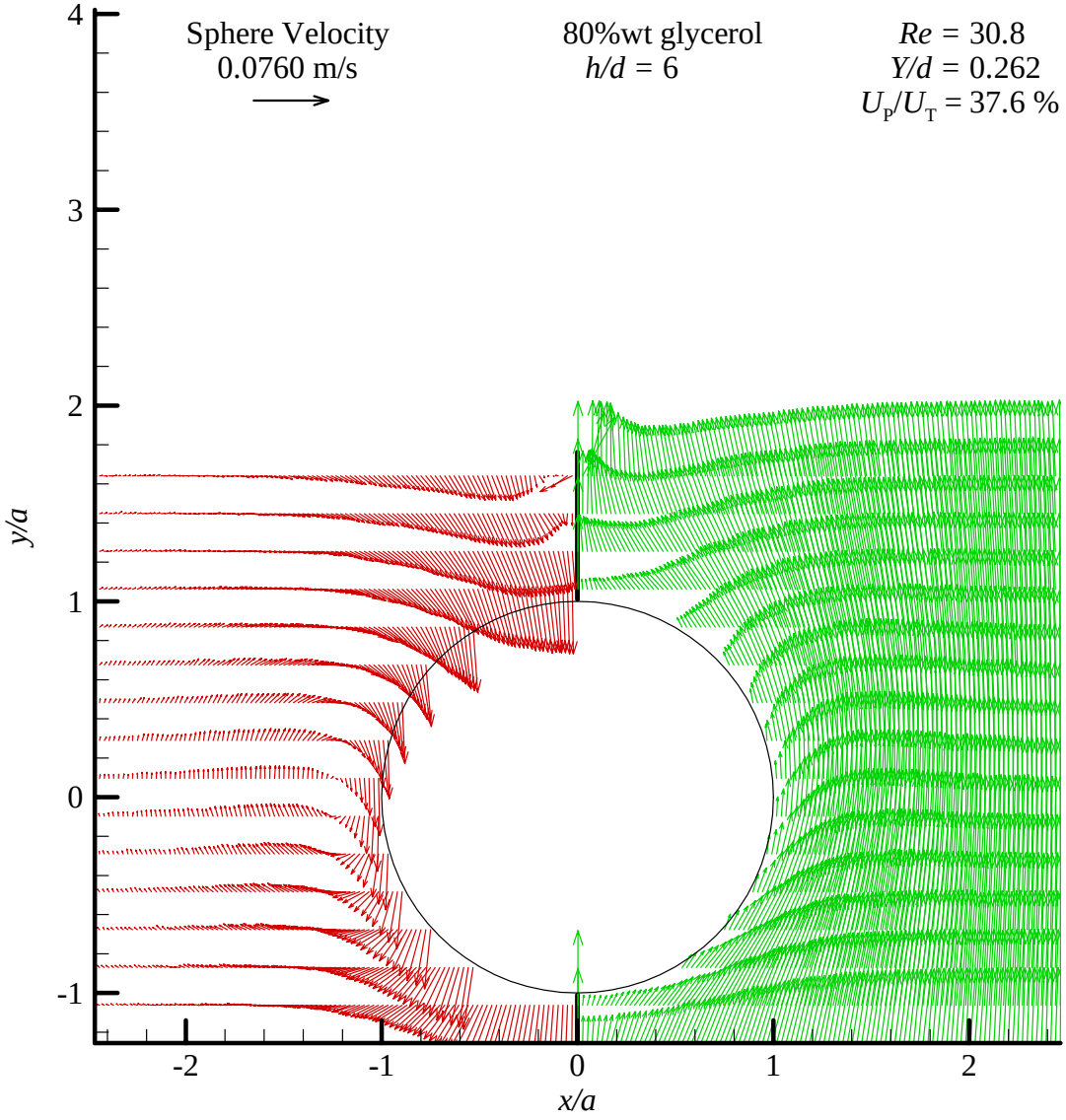

Figure A-17: Velocity field around a falling solid sphere. The left side shows velocities with respect to the moving sphere while the right is with respect to a stationary sphere. 80%wt glycerol, h/d=6.0, Y/d=0.262, U_P=76.0 mm/s, Re=30.8, U_P/U_T=37.6%. Every eighth row of vectors is shown.

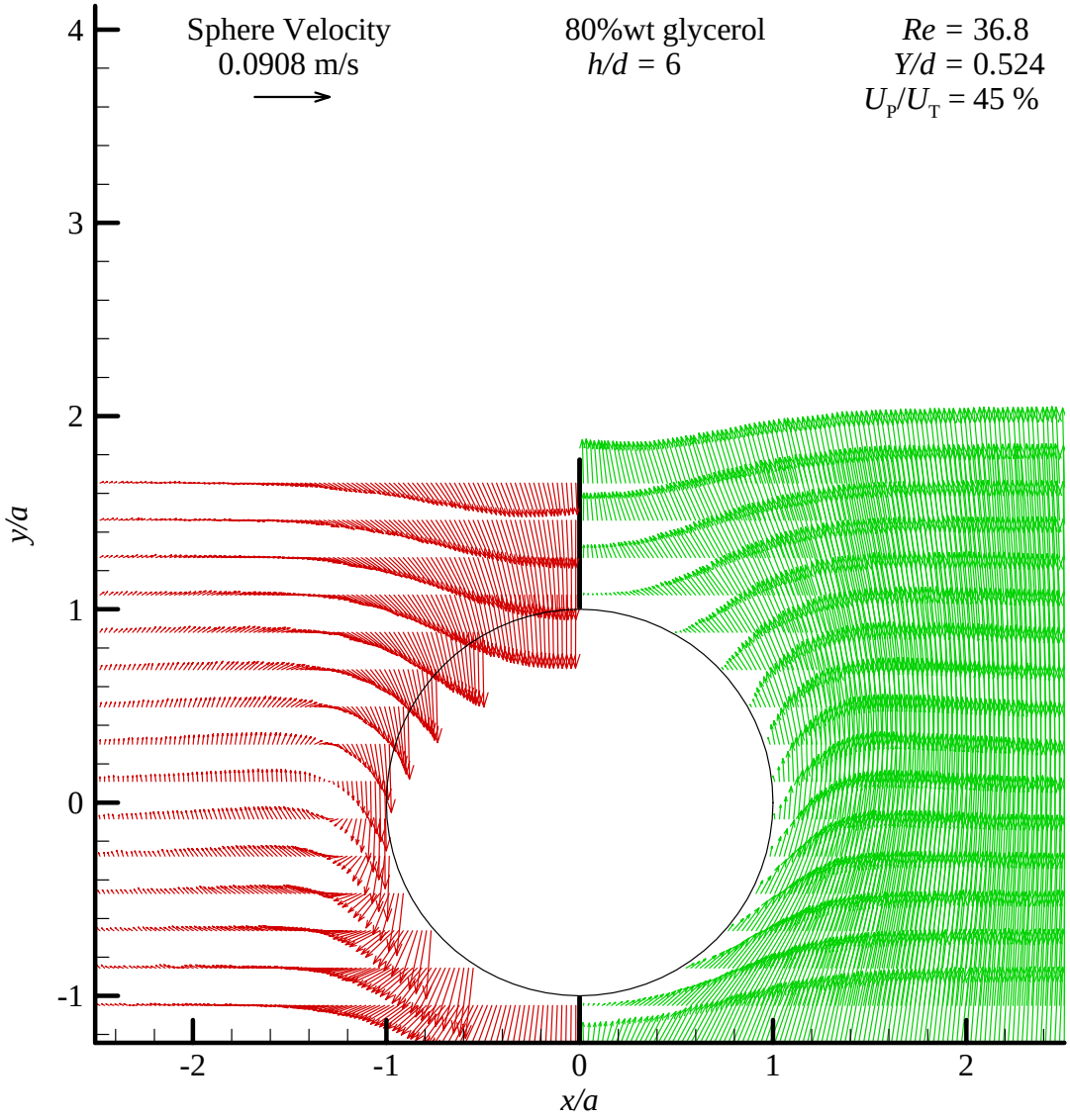

Figure A-18: Velocity field around a falling solid sphere. The left side shows velocities with respect to the moving sphere while the right is with respect to a stationary sphere. 80%wt glycerol, h/d=6.0, Y/d=0.524, U_P=90.8 mm/s, Re=36.8, U_P/U_T=45%. Every eighth row of vectors is shown.

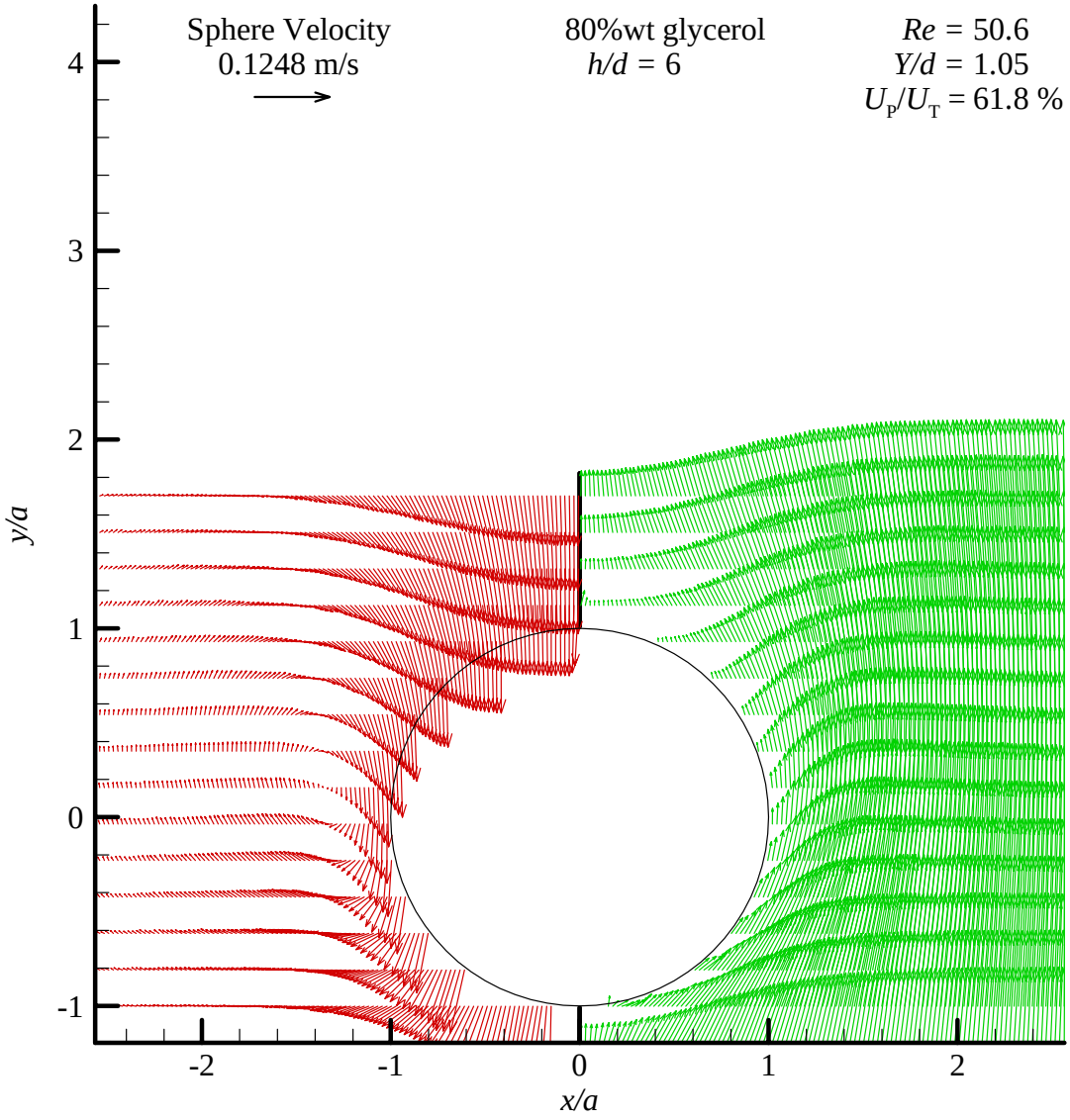

Figure A-19: Velocity field around a falling solid sphere. The left side shows velocities with respect to the moving sphere while the right is with respect to a stationary sphere. 80%wt glycerol, h/d=6.0, Y/d=1.05, U_P=124.8 mm/s, Re=50.6, U_P/U_T=61.8%. Every eighth row of vectors is shown.

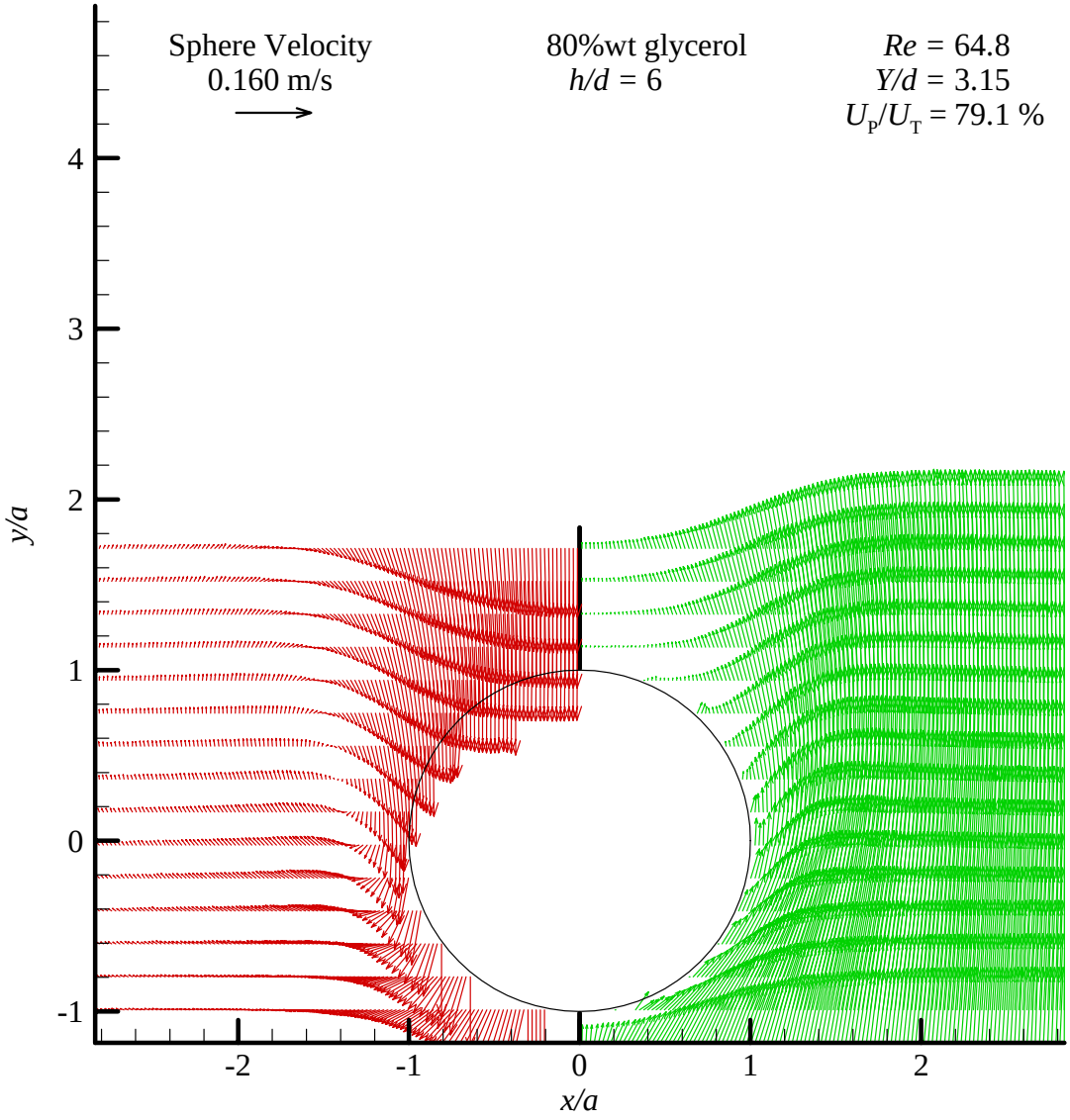

Figure A-20: Velocity field around a falling solid sphere. The left side shows velocities with respect to the moving sphere while the right is with respect to a stationary sphere. 80%wt glycerol, h/d=6.0, Y/d=3.15, U_P=160 mm/s, Re=64.8, U_P/U_T=79.1%. Every eighth row of vectors is shown.

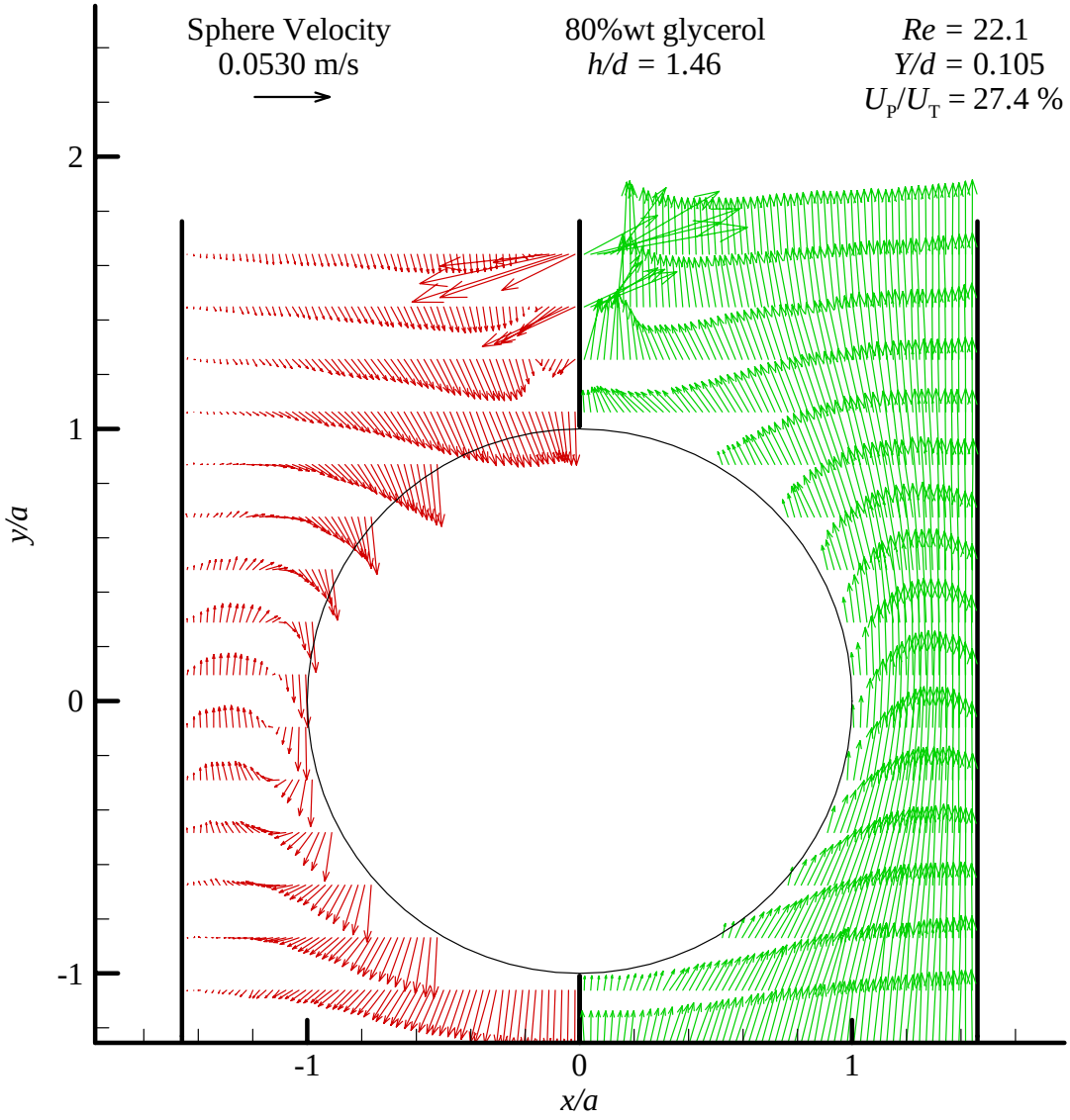

Figure A-21: Velocity field around a falling solid sphere. The left side shows velocities with respect to the moving sphere while the right is with respect to a stationary sphere. 80%wt glycerol, h/d=1.5, Y/d=0.105, U_P=53.0 mm/s, Re=22.1, U_P/U_T=27.4%. Every eighth row of vectors is shown.

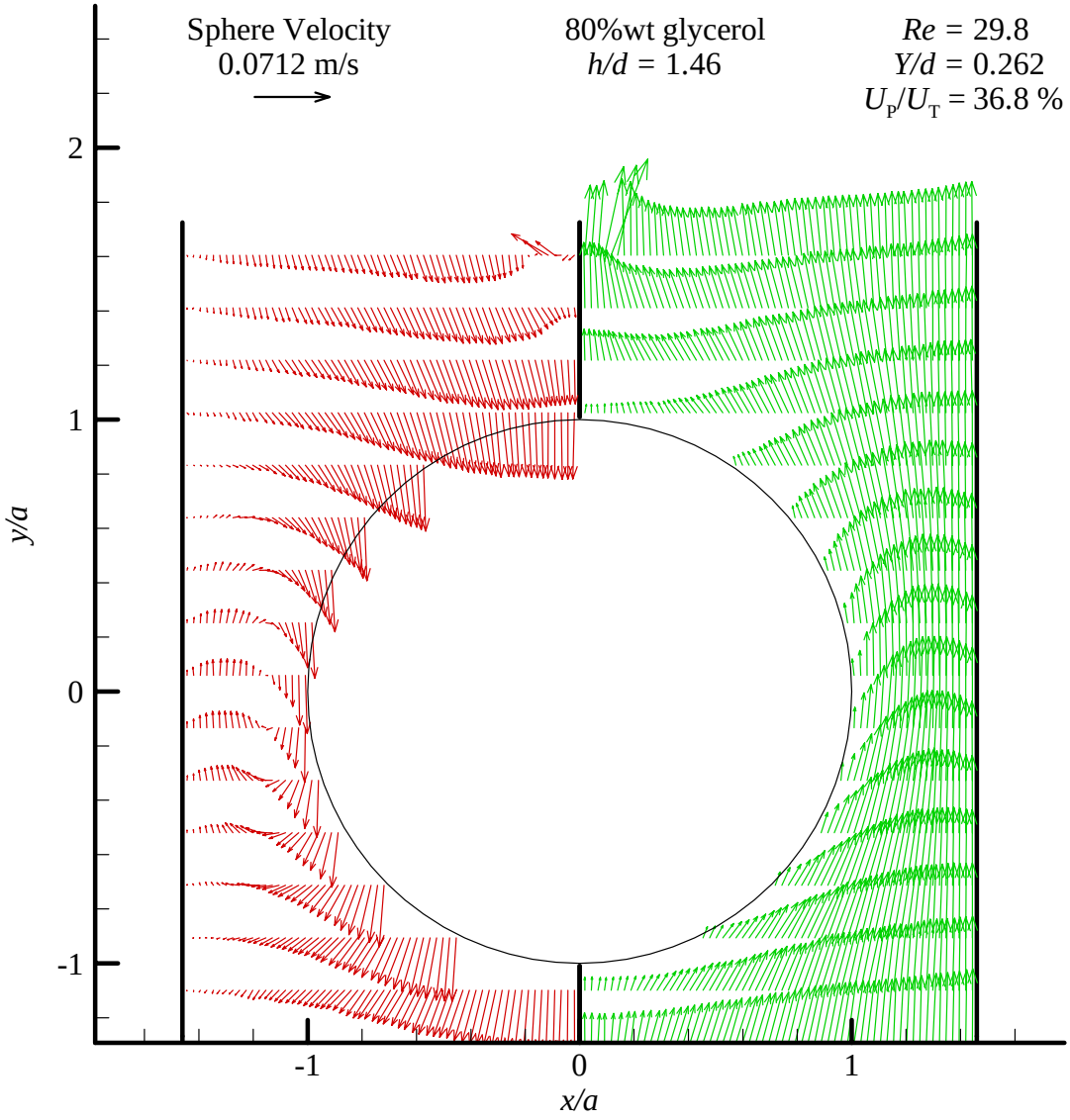

Figure A-22: Velocity field around a falling solid sphere. The left side shows velocities with respect to the moving sphere while the right is with respect to a stationary sphere. 80%wt glycerol, h/d=1.5, Y/d=0.262, U_P=71.2 mm/s, Re=29.8, U_P/U_T=36.8%. Every eighth row of vectors is shown.

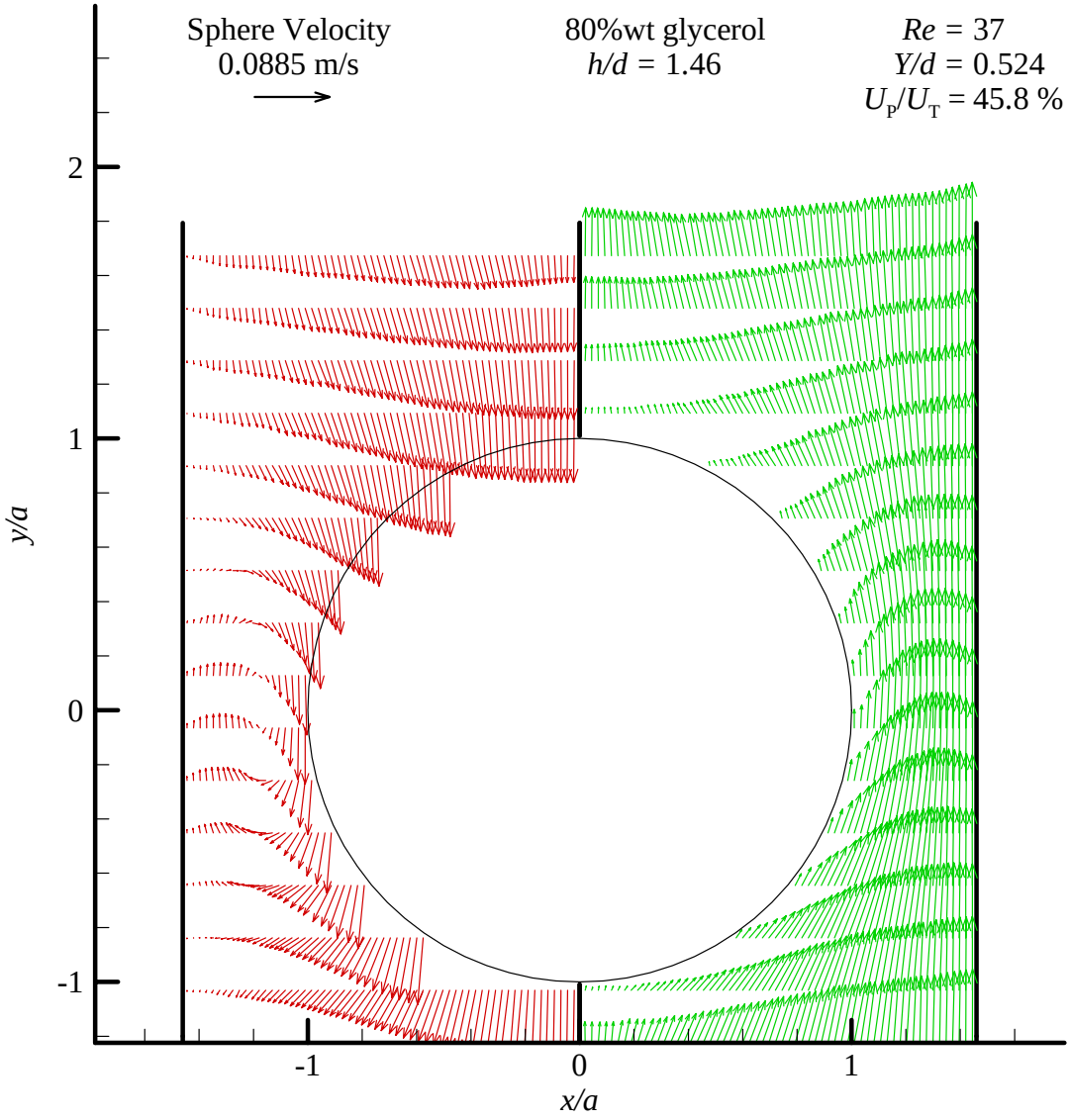

Figure A-23: Velocity field around a falling solid sphere. The left side shows velocities with respect to the moving sphere while the right is with respect to a stationary sphere. 80%wt glycerol, h/d=1.5, Y/d=0.524, U_P=88.5 mm/s, Re=37, U_P/U_T=45.8%. Every eighth row of vectors is shown.

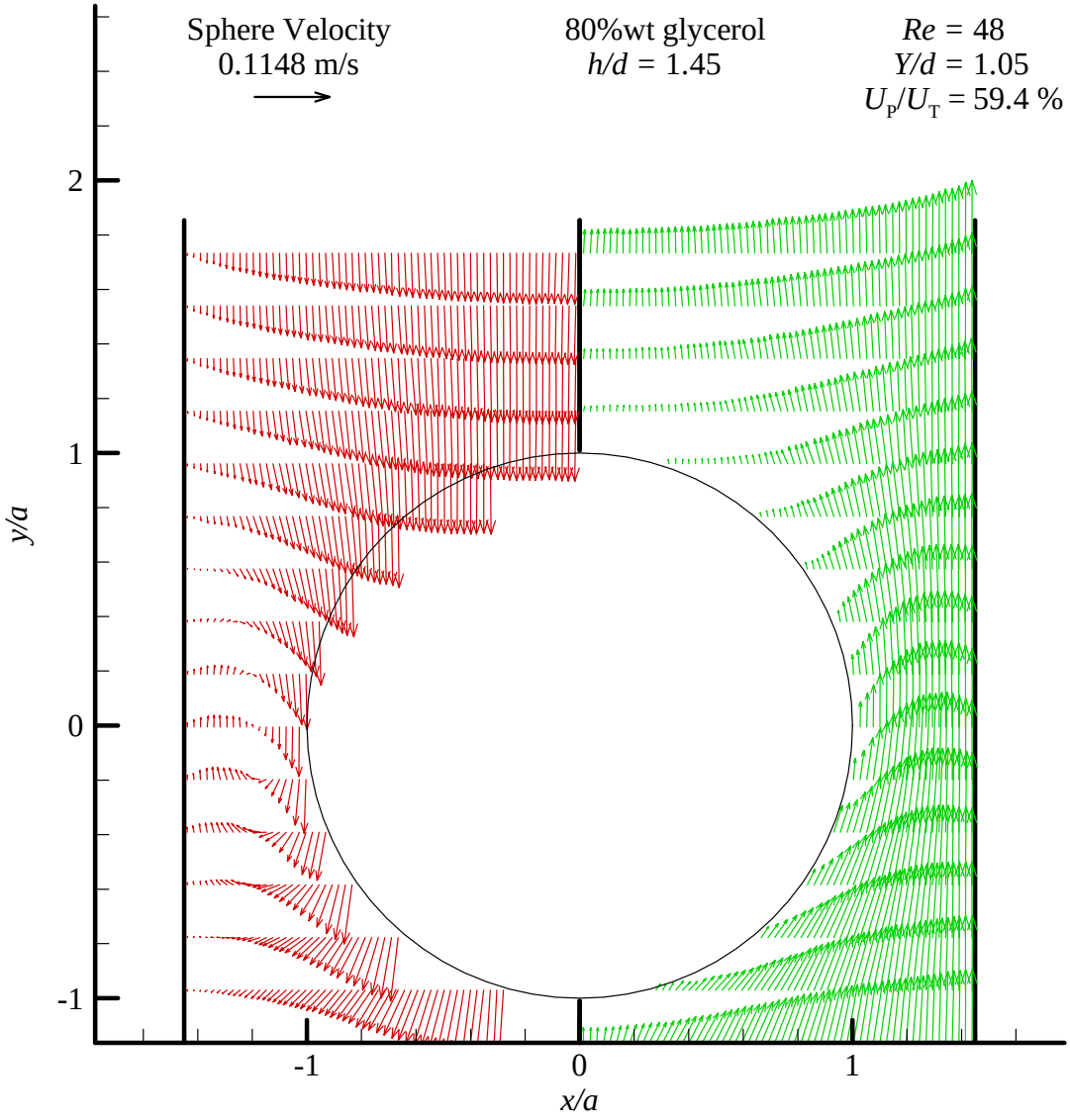

Figure A-24: Velocity field around a falling solid sphere. The left side shows velocities with respect to the moving sphere while the right is with respect to a stationary sphere. 80%wt glycerol, h/d=1.5, Y/d=1.05, U_P=114.8 mm/s, Re=48, U_P/U_T=59.4 %. Every eighth row of vectors is shown.

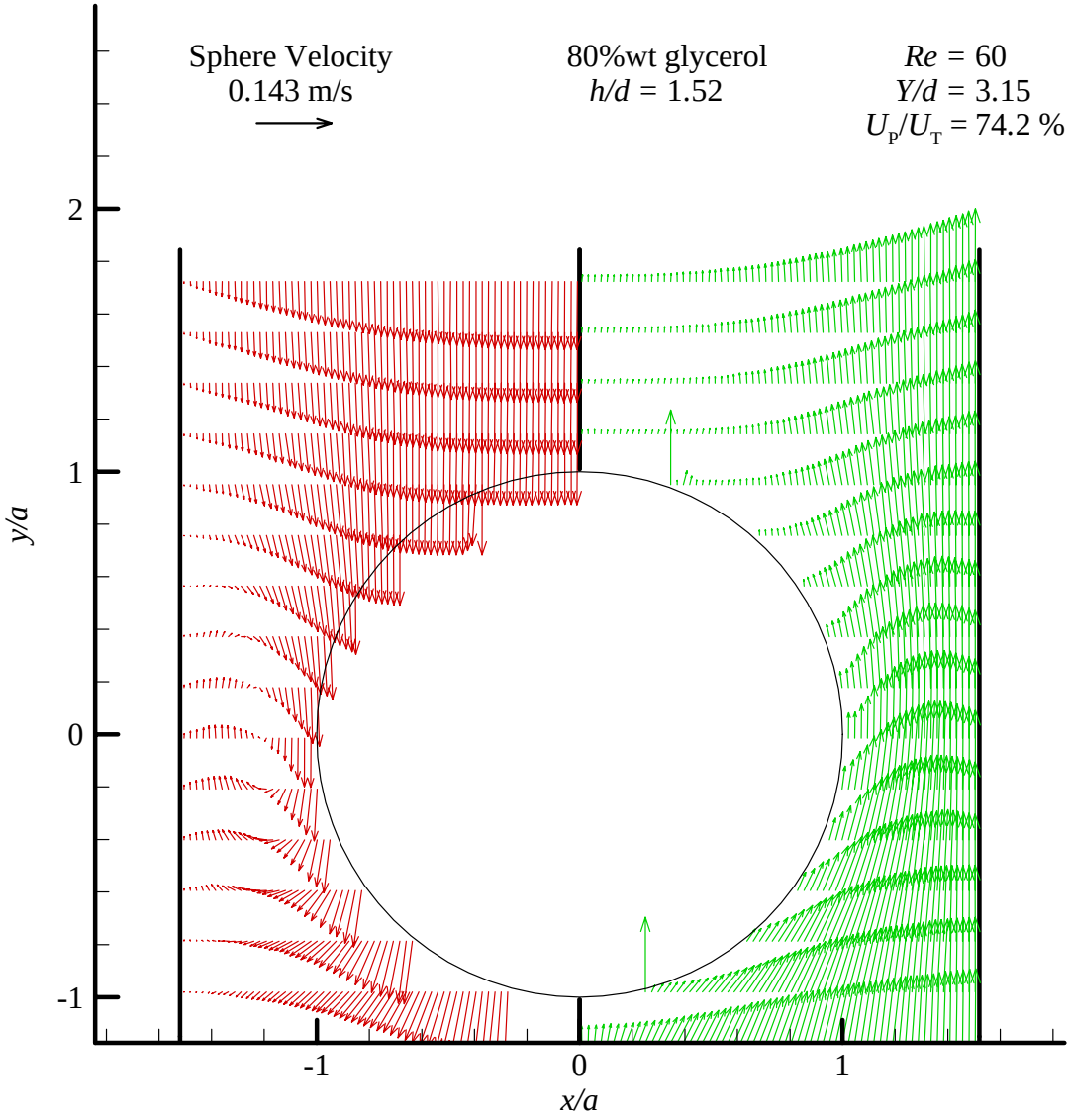

Figure A-25: Velocity field around a falling solid sphere. The left side shows velocities with respect to the moving sphere while the right is with respect to a stationary sphere. 80%wt glycerol, h/d=1.5, Y/d=3.15, U_P=143 mm/s, Re=60, U_P/U_T=74.2%. Every eighth row of vectors is shown.

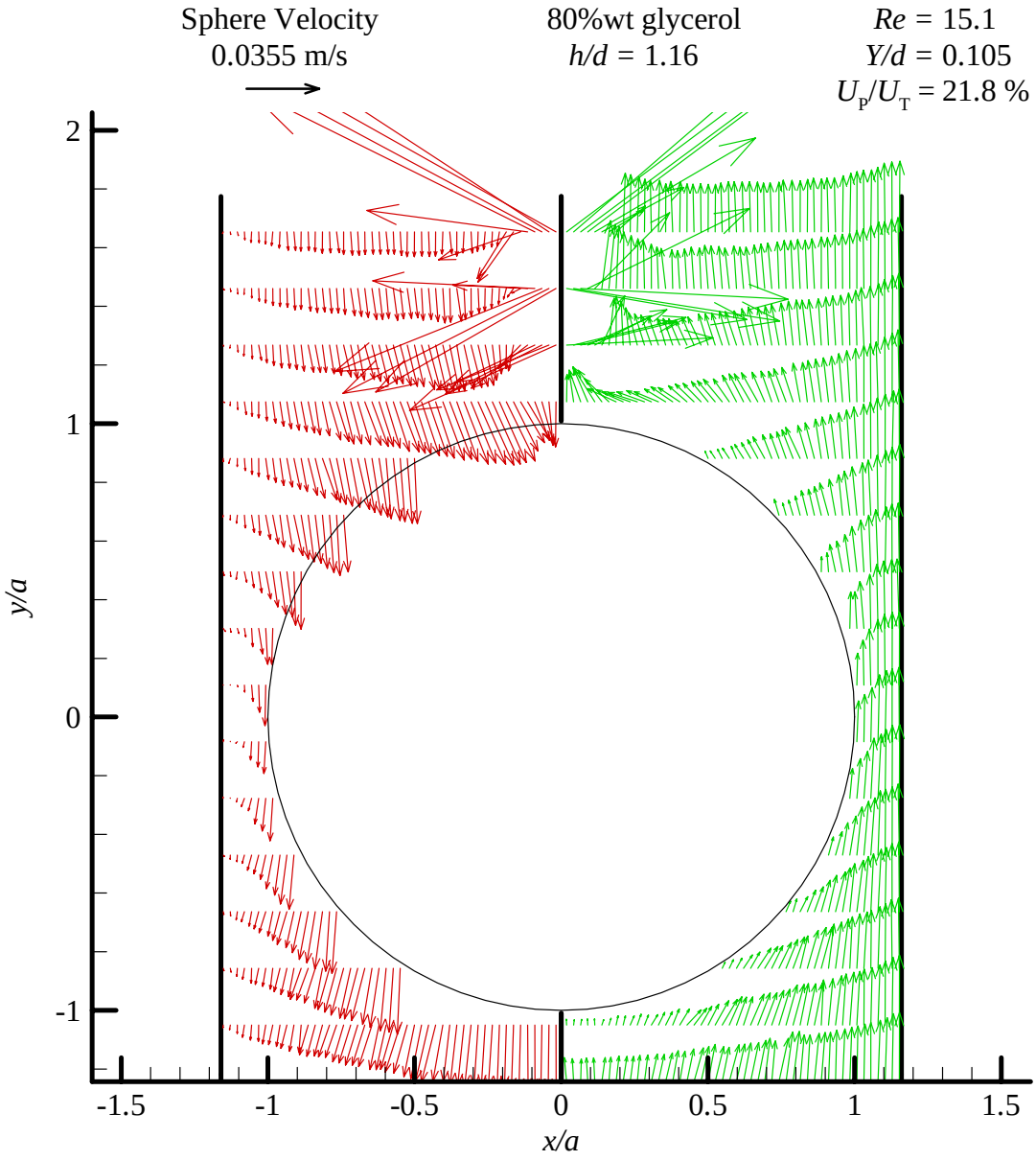

Figure A-26: Velocity field around a falling solid sphere. The left side shows velocities with respect to the moving sphere while the right is with respect to a stationary sphere. 80%wt glycerol, h/d=1.2, Y/d=0.105, U_P=35.5 mm/s, Re=15.1, U_P/U_T=21.8%. Every eighth row of vectors is shown.

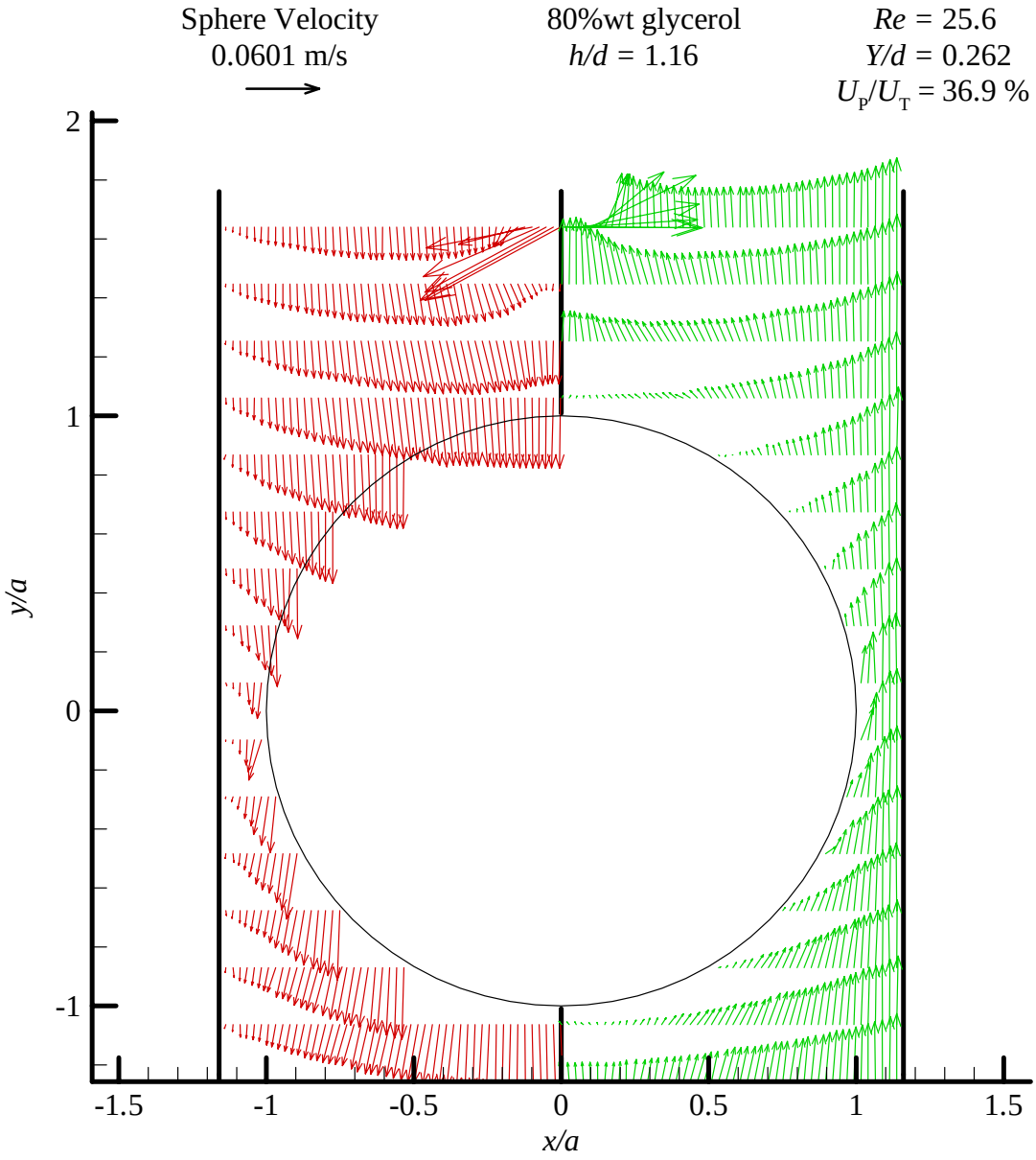

Figure A-27: Velocity field around a falling solid sphere. The left side shows velocities with respect to the moving sphere while the right is with respect to a stationary sphere. 80%wt glycerol, h/d=1.2, Y/d=0.262, U_P=60.1 mm/s, Re=25.6, U_P/U_T=36.9%. Every eighth row of vectors is shown.

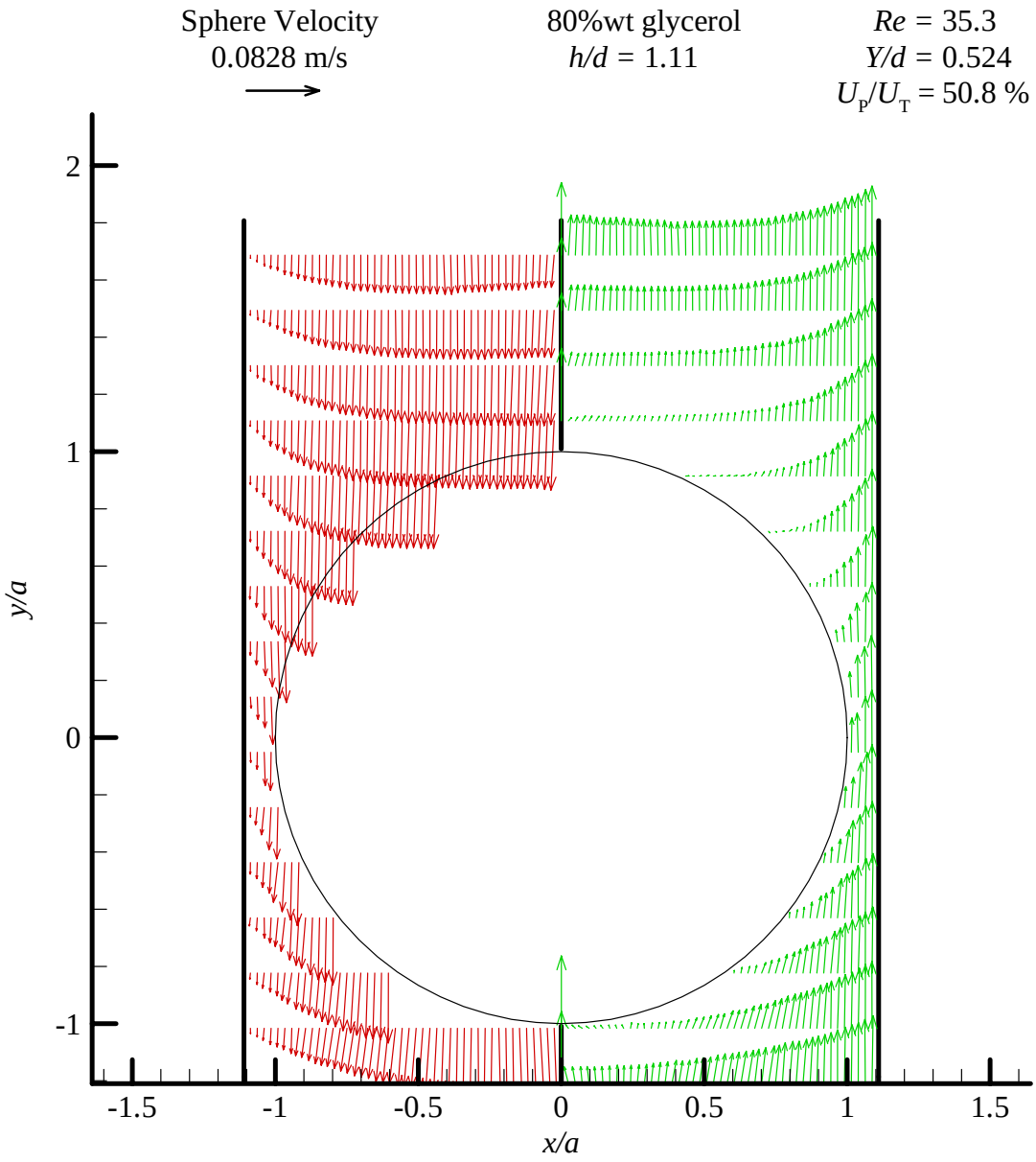

Figure A-28: Velocity field around a falling solid sphere. The left side shows velocities with respect to the moving sphere while the right is with respect to a stationary sphere. 80%wt glycerol, h/d=1.2, Y/d=0.524, U_P=82.8 mm/s, Re=35.3, U_P/U_T=50.8%. Every eighth row of vectors is shown.

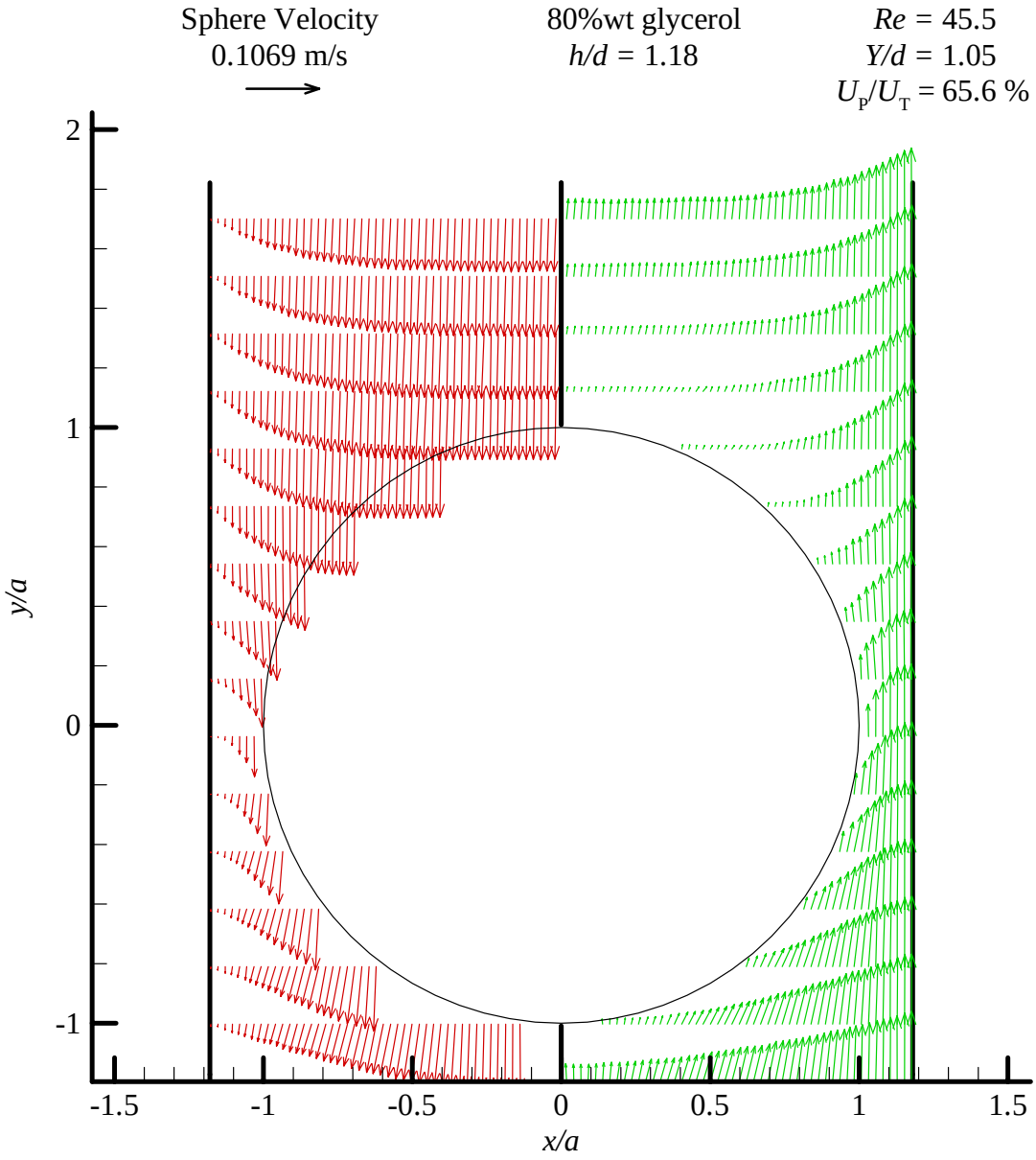

Figure A-29: Velocity field around a falling solid sphere. The left side shows velocities with respect to the moving sphere while the right is with respect to a stationary sphere. 80%wt glycerol, h/d=1.2, Y/d=1.05, U_P=106.9 mm/s, Re=45.5, U_P/U_T=65.6%. Every eighth row of vectors is shown.

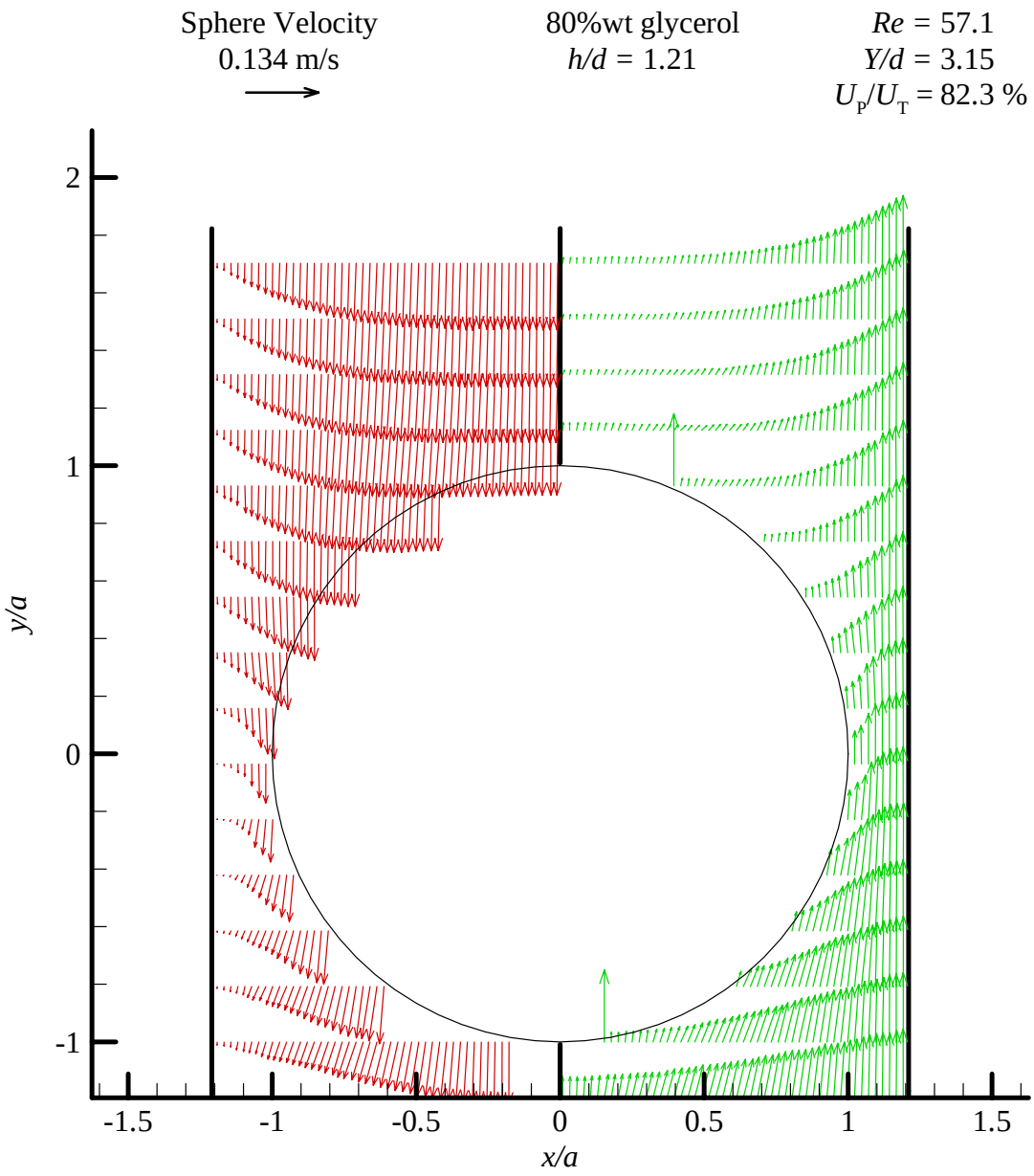

Figure A-30: Velocity field around a falling solid sphere. The left side shows velocities with respect to the moving sphere while the right is with respect to a stationary sphere. 80%wt glycerol, h/d=1.2, Y/d=3.15, U_P=134 mm/s, Re=57.1, U_P/U_T=82.3%. Every eighth row of vectors is shown.

Appendix B
Statements of Permission to Reprint Third-Party Material

This appendix contains permission statements from both Elsevier and Dover Publications. The permission statement from Elsevier appears on page 130, while the permission statement from Dover Publications is a result of email correspondence shown on pages 131 and 132.

425·125
YEARS OF PUBLISHING
TRADITION | EXCELLENCE
We commemorate the founding of the House of Elzevir in 1580 and celebrate the establishment of the Elsevier company in 1880.

ELSEVIER

21 September 2005 Our ref: HG/mm/sept 05.J036

Mr Warren Brooke
University of Saskatchewan
Wtb311@mail.usask.ca

Dear Mr Brooke

INTERNATIONAL JOURNAL OF MULTIPHASE FLOW, *Vol 7, 1980, pp 46-47, Miyamura et al, "Experimental wall…"*

As per your letter dated 19 September 2005, we hereby grant you permission to reprint the aforementioned material at no charge **in your thesis, in print and on the University of Saskatchewan web site** subject to the following conditions:

1. If any part of the material to be used (for example, figures) has appeared in our publication with credit or acknowledgement to another source, permission must also be sought from that source. If such permission is not obtained then that material may not be included in your publication/copies.

2. Suitable acknowledgment to the source must be made, either as a footnote or in a reference list at the end of your publication, as follows:

   "Reprinted from Publication title, Vol number, Author(s), Title of article, Pages No., Copyright (Year), with permission from Elsevier".

3. Reproduction of this material is confined to the purpose for which permission is hereby given.

4. This permission is granted for non-exclusive world **English** rights only. For other languages please reapply separately for each one required. Permission excludes use in an electronic form other than as specified above.

5. This includes permission for the National Library of Canada to supply single copies, on demand, of the complete thesis. Should your thesis be published commercially, please reapply for permission.

Yours sincerely

HGainford

Helen Gainford
Rights Manager

Your future requests will be handled more quickly if you complete the online form at
www.elsevier.com/locate/permissions

Date: Tue, 11 Oct 2005 22:57:17 -0400
From: Tracy_McDonald <Tracy_McDonald@doverpublications.com>
To: wtb311@mail.usask.ca
Subject: Thank You for Your Dover Inquiry
Part(s): Message Source Save As...

Dear Mr. Brooke,

Thank you for contacting us regarding rights and permission for Dover Publications.

Our Rights and Permissions Department is researching your inquiry and will be in touch with you soon.

If you have any further questions, or if I may assist you in any way, please don't hesitate to contact me at tracy_mcdonald@doverpublications.com, and I will respond promptly.

Thank you for your interest in Dover Publications.

Best Regards,

Tracy McDonald
Customer Care Specialist
DoverPublications.com

FirstName: Warren
LastName: Brooke
Email: wtb311@mail.usask.ca
bookstofind: I am seeking permission to use a figure from a 1934 text by Prantl and Tietjens in a thesis for my masters degree. I believe that Dover now publishes this book.

These are the details of the title:

Prandtl, L., and Teitjens, O. G., "Applied Hydro- and Aeromechanics", McGraw-Hill Book Company, Inc., New York, 1934; Copyright, 1934, by the United Engineering Trustees, Inc.

I wish to use figure 14 on page 284, and figure 56 on page 302 of this book.

One copy of the thesis will be printed, and an electronic version will be available on the University of Saskatchwan Library website.

Can you grant me permission to use these figures?

Thank you for your help in this regard.

sincerely,
Warren Brooke

Thank you for your inquiry.
Although we would not want this statement construed as a warranty or guarantee, to the best of our knowledge this material is in the public domain. Therefore, Dover cannot grant or withhold permission for its use.
In the interest of proper documentation we would, of course, appreciate a credit line indicating author, title and publisher.

Terri Torretto
Dover Publications
Rights & Permissions Dept.